

The radiation balance of Midmar Dam in KwaZulu-Natal, South Africa

by

LINDUMUSA MYENI

Submitted in fulfilment of the academic requirements of

Master of Science

in Agrometeorology

School of Agricultural, Earth and Environmental Sciences

College of Agriculture, Engineering and Science

University of KwaZulu-Natal

Pietermaritzburg

South Africa

November 2016

PREFACE

The research contained in this dissertation was completed by the candidate while based in the Discipline of Agrometeorology, School of Agricultural, Earth and Environmental Sciences of the College of Agriculture, Engineering and Science, University of KwaZulu-Natal, Pietermaritzburg Campus, South Africa. The research was financially supported by Water Research Commission and National Research Foundation.

The contents of this work have not been submitted in any form to another university and, except where the work of others is acknowledged in the text, the results reported are due to investigations by the candidate.

Signed: Professor MJ Savage

Date: 21 November 2016

DECLARATION 1: PLAGIARISM

I, I, Lindumusa Myeni, declare that:

(i) the research reported in this dissertation, except where otherwise indicated or acknowledged, is my original work;

(ii) this dissertation has not been submitted in full or in part for any degree or examination to any other university;

(iii) this dissertation does not contain other persons' data, pictures, graphs or other information, unless specifically acknowledged as being sourced from other persons;

(iv) this dissertation does not contain other persons' writing, unless specifically acknowledged as being sourced from other researchers. Where other written sources have been quoted, then:

a) their words have been re-written but the general information attributed to them has been referenced;

b) where their exact words have been used, their writing has been placed inside quotation marks, and referenced;

(v) where I have used material for which publications followed, I have indicated in detail my role in the work;

(vi) this dissertation is primarily a collection of material, prepared by myself, published as journal articles or presented as a poster and oral presentations at conferences. In some cases, additional material has been included;

(vii) this dissertation does not contain text, graphics or tables copied and pasted from the Internet, unless specifically acknowledged, and the source being detailed in the dissertation and in the References sections.

Signed: Lindumusa Myeni

Date: 21 November 2016

DECLARATION 2: PUBLICATIONS

My role in each paper and presentation is indicated. The * indicates corresponding author.

1. Savage MJ, Pasi JM, Myeni L*, Clulow AD. Monin-Obukhov Similarity Method for Open Water Evaporation. Paper presentation to 18th SANCIAHS Symposium, Durban, South Africa in September 2016. Presented by MJ Savage.
2. Savage MJ, Pasi JM, Myeni L*, Clulow AD. 2016. Open water evaporation measurement using micrometeorological methods. Unpublished Water Research Commission Report No. K5/2335.

ABSTRACT

Energy balance models driven by the difference between net irradiance (R_n) and water-stored heat flux (G), the available energy flux, are the most accurate methods of estimating open water evaporation after the direct measurement of open water evaporation and are often used as a reference method against which other methods are compared. However, measurements of the available energy flux above water storage may not be readily available. The available energy flux is measured directly with greater difficulty because it involves significant financial investment in instrumentation and extensive field work on a reservoir. The lack of the available energy flux data above water storages could be solved by using the models that estimate available energy flux from meteorological data that is readily available in most standard weather stations.

The modified Penman-Monteith model seems to be the most promising technique to estimate the available energy flux for open water evaporation from different water storages of different sizes. The modified Penman-Monteith model utilises the concepts of equilibrium temperature to estimate the water-body temperature of the storage using an iterative procedure. The estimated water-body temperature is essential for computing G and the outgoing infrared irradiance (L_u) from the water surface. Therefore, in this study, the Daily Penman, Monteith, Equilibrium Temperature Hargreaves-Samani (DPMETHS) model, implemented in Excel to incorporate the daily solar radiation estimation model which utilizes the daily minimum and maximum air temperature to infill any gaps of missing solar irradiance data was used to estimate the available energy flux. The DPMETHS model to estimate the available energy flux for open water evaporation is on its developmental stage and has not been used in any known study. Therefore, there was a need to evaluate the performance of the DPMETHS model to estimate the available energy flux above water from different climatic conditions using the land-based meteorological data. However, there was a vital need to understand the factors enhancing temporal and spatial variability of the radiation balance at water storage to model available energy flux at water storage with confidence.

The net radiation balance is the balance between the net solar radiation and net infrared radiation under steady atmospheric conditions

Measurements of the available energy flux above open water were performed from 12th February to 4th April in 2016 at Midmar Dam, KwaZulu-Natal, South Africa. Radiative fluxes acquired using the net radiometer were accompanied by water temperature profile measurements from which G was computed. The results of this study showed that the solar irradiance (R_s) was the dominant component of R_n during the day while infrared irradiance was the dominant component of R_n during night. The cloud cover, reflection coefficient of water, air temperature and surface water temperature (SWT) were the main factors that control the temporal and spatial variability of the radiation balance above open water surface. The spatial variation of R_n above open water was mainly due to the spatial variability in SWT since with constant emissivity, L_u depends on SWT alone. The *in-situ* measurement of SWT compared well to the Landsat-8 estimate of SWT . The observed average of 1.5 to 2 °C variability of SWT across Midmar Dam implies the very low spatial variability of L_u which is temperature dependent. Therefore, the low spatial variability of SWT is associated with low spatial variation of R_n across the dam. Despite the high spatial resolution and freely availability of Landsat-8 data, remote sensing methodology still needs calibration and validation with ground truth data and are unlikely to yield daily R_n .

The variability of the available energy flux over water indicated that the R_n was the dominant component of the available energy flux at water surface. However, G showed a similar diurnal variation to R_n with comparable magnitudes and peaked at the same time as the peak in R_n . During the daytime, R_n fluxes were positive, corresponding to a source of the energy flux while during night-time, R_n fluxes were negative, corresponding to a loss of energy flux from the water surface.

To evaluate the performance of the DPMETHS model to simulate R_n above Midmar Dam, model estimates of R_n were compared to the measurements of R_n above water surface at Midmar Dam. Results indicated a good relationship between the daily estimates of R_n predicted from the DPMETHS model and the daily R_n measured above water, with slope (m) of 0.76, regression coefficient exceeding 0.70 and the root mean square error (RMSE) of 3.04 MJ m⁻². The mean bias error (MBE) of 0.70 MJ m⁻² indicated that the model often over-simulated R_n . The estimated R_n and measured R_n fluxes were not statistically different at the 99.5 % level of confidence. The under-simulation of R_n during overcast days was attributed to under-

simulation of L_d due to poor estimation of cloud fraction using the Brunt's formula that was established only for clear-skies. The relative lack of validity of the assumption that the SWT is equal to the T_{air} together with the use of wind speed measured at the land-based station which was less than the wind speed at water surface as a model inputs resulted in the model under-simulating L_u which resulted on the over-simulation of R_n on some of the days.

Model estimates of R_n were compared to the measurements of R_n for the Stratus station at the eastern Pacific Ocean. Results indicated a good relationship between the daily R_n estimated using the DPMETHS model and R_n measured above ocean, with m of 0.62, regression coefficient exceeding 0.76 and RMSE of 5.67 MJ m^{-2} . The MBE of 5.45 MJ m^{-2} indicated that the model often over-simulated R_n . The estimated R_n and measured R_n fluxes for the Stratus station at the eastern Pacific Ocean were statistically different at the 99.5 % level of confidence. The over-simulation of R_n at the ocean was attributed to the poor model input data available at the ocean. The presence of the low, thick stratus clouds above the ocean emitted greater L_d than expected and resulted on the poor simulations of L_d at the ocean.

The availability of long-term meteorological dataset at Cedara station near Midmar Dam enables the unique opportunity to investigate the potential impacts of climate change on the radiation balance of Midmar Dam. This study showed evidence of the impacts of climate change on the radiation balance of Midmar Dam. Climate changes attributed to the global increase in the concentrations of total carbon dioxide threaten to increase the long-term air temperatures of the earth with consequent increase in R_n due to increases in L_d .

This study showed that R_n can be simulated well from standard weather station data using the DPMETHS model. The DPMETHS model performed successfully on the Midmar Dam study and to a lesser extent at the eastern Pacific Ocean. Despite challenges encountered during this study, results produced are generally acceptable and it is believed that the DPMETHS model can be used to estimate R_n for open water at different climatic conditions. However, a better and reliable method of measuring or estimating G is required since G fluxes were measured with great difficulty using thermocouples. Therefore, model estimates of G were not compared to unreliable measurements of G in this study.

ACKNOWLEDGMENTS

First and foremost, I would like to thank my loving God for giving me the opportunity to write this dissertation. I would also like to thank my lovely family and empowering friends for their support and for believing in me throughout the study period. I would also like to express my sincere gratitude to my supervisor Prof. Savage for the continuous support through this research, for his patience, motivation, and immense knowledge.

Several special acknowledgements deserve specific mention:

the staff of the Department of Water and Sanitation offices and KwaZulu-Natal Wildlife at Midmar for allowing the use of their facilities for this work;

this work would not have been possible without the technical support from: JM Pasi (University of KwaZulu-Natal), Dr. AD Clulow (University of KwaZulu-Natal), S Strydom (University of KwaZulu-Natal), NC Mbangiwa (University of KwaZulu-Natal);

Mr B Gijsbertsen (University of KwaZulu-Natal) for his assistance with remote sensing and GIS;

Mrs MA Savage (University of KwaZulu-Natal) for the administration and support towards my research is well acknowledged;

Agriculture Research Council for meteorological data from their nearby stations;

Umgeni Water and Department of Water and Sanitation for supplying water level and surface area data of Midmar Dam during study period;

Woods Hole Oceanographic Institution for the (online) Status data in the eastern Pacific Ocean;

University of KwaZulu-Natal, National Research Foundation, and Water Research Commission (South Africa) as part of project K5/2355 for funding.

TABLE OF CONTENTS

	<u>Page</u>
PREFACE	ii
DECLARATION 1: PLAGIARISM.....	iii
ABSTRACT	v
ACKNOWLEDGMENTS.....	viii
TABLE OF CONTENTS	ix
LIST OF TABLES	xii
LIST OF FIGURES.....	xiii
CHAPTER 1 : INTRODUCTION	1
1.1 Background	1
1.2 Justification	3
1.3 Aim.....	5
1.4 Objectives.....	5
1.5 Outline of dissertation	5
CHAPTER 2 : LITERATURE REVIEW	7
2.1 Radiation balance	7
2.1.1 Introduction.....	7
2.1.2 Radiation balance above open water surface.....	7
2.2 Diurnal and seasonal variability of the radiation balance	10
2.1.4 Spatial variability of the net irradiance above water surface.....	11
2.2 Available energy flux for open water evaporation.....	13
2.2.1 Introduction.....	13
2.2.2 Measuring available energy flux	13
2.2.3 Modelling available energy flux	13
2.2.4 Description of the DPMETHS model for computing available energy flux	15
CHAPTER 3 : METHODS AND MATERIALS.....	18
3.1 Study site description	18
3.2 Experimental setup.....	19
3.3 Instrumentation.....	19
3.4 Equipment testing and calibration.....	21

3.4.1 Laboratory equipment test	21
3.4.1.1 Testing the land-based station sensors	21
3.4.1.2 Testing the water-based station sensors	22
3.4.2 Calibration of the station systems	23
3.5 Systems set-up.....	23
3.6 Data collection and processing.....	25
3.7 Data analysis	26
3.8 Landsat-8 surface water temperatures data collection and processing.....	27
3.9 Acquisition of the ocean data	28
3.10 Acquisition of the long-term historical data at Cedara station	29
CHAPTER 4 : RESULTS AND DISCUSSION	30
4.1 Introduction	30
4.2 Calibration of the CNR4 net radiometer	31
4.2.1 Solar irradiance	31
4.2.2 Reflected solar irradiance	31
4.2.3 Incoming infrared irradiance	31
4.2.4 Outgoing infrared irradiance.....	32
4.2.5 Net irradiance.....	36
4.2.6 General comments	37
4.3 Climatic conditions during study period at Midmar Dam.....	37
4.4 Radiation balance of the water surface at Midmar Dam	38
4.4.1 Factors enhancing temporal variability of the radiation balance over water surface	38
4.4.1.1 Cloud cover	38
4.4.1.2 Reflection coefficient of water	40
4.4.1.3 Air and surface water temperature	43
4.4.2 Spatial variability of the radiation balance above water at Midmar Dam	44
4.5 Above-water available energy flux	46
4.5.1 Water-stored heat flux	46
4.5.2 Variability of the available energy flux components above water	49
4.6 Modelling study at Midmar Dam	51
4.6.1 Comparisons between land and water meteorological measurements	51
4.6.1.1 Solar irradiance	52
4.6.1.2 Air temperature	52

4.6.1.3 Wind speed	52
4.6.1.4 Relative humidity	52
4.6.1.5 General comments	55
4.6.2 Modelling radiative fluxes	56
4.6.2.1 Solar irradiance	56
4.6.2.2 Incoming infrared irradiance	56
4.6.2.3 Outgoing infrared irradiance	58
4.6.2.4 Net irradiance	59
4.6.2.5 Overall discussion on modelling of the radiative fluxes at Midmar Dam ..	61
4.7 Modelling study at Stratus station, East Pacific Ocean.....	62
4.7.1 Modelling radiative fluxes at Stratus station, East Pacific Ocean	62
4.7.1.1 Incoming infrared irradiance	62
4.7.1.2 Net irradiance	63
4.7.2 Overall discussion on modelling of the radiative fluxes at Stratus ocean station ..	65
4.8 Potential impacts of climate change on the radiation balance of Midmar Dam	65
4.8.1 Long-term radiation balance of Midmar Dam.....	65
4.8.2 Overall discussion on the potential impacts of climate change on the radiation balance of Midmar Dam	68
4.8.3 General comments	69
CHAPTER 5 : CONCLUSIONS AND RECOMMENDATIONS FOR FURTHER RESEARCH.....	70
5.1 Introduction	70
5.2 Findings.....	70
5.3 Challenges and recommendations for future research	72
5.4 Final comments and summary.....	73
CHAPTER 6 : REFERENCES	75

LIST OF TABLES

<u>Table</u>	<u>Page</u>
Table 3.1: Some characteristics of Midmar Dam (adapted from Mengistu and Savage (2010)).	19
Table 3.2: Details of the equipment used for land-based and water-based weather station systems at Midmar Dam during the study period.	20
Table 3.3: Location of the different stations used in the study	26

LIST OF FIGURES

<u>Figure</u>	<u>Page</u>
Figure 2.1: Schematic diagram showing radiation balance on earth's surface, where G_g are the greenhouse gases (Savage, 2012).....	8
Figure 3.1: Map showing the location of the Midmar Dam in the Umgeni catchment in KwaZulu-Natal midlands.	18
Figure 3.2: Location of the land and water-based stations at Midmar Dam during the study period.....	24
Figure 3.3: Land and water-based stations at Midmar Dam during the study period.....	25
Figure 4.1: Comparisons between R_s_CNR4 and R_s_CNR1 for a two-day period (27 th and 29 th July 2015) at the AIM site.....	32
Figure 4.2: Regression plot of R_s_CNR4 vs R_s_CNR1 for a two-day period (27 th and 29 th July 2015) at the AIM site.	33
Figure 4.3: Comparisons between rR_s_CNR4 and rR_s_CNR1 for a two-day period (27 th and 29 th July 2015) at the AIM site.....	33
Figure 4.4: Regression plot of rR_s_CNR4 vs rR_s_CNR1 for a two-day period (27 th and 29 th July 2015) at the AIM site.....	34
Figure 4.5: Comparisons between L_d_CNR4 and L_d_CNR1 for a two-day period (27 th and 29 th July 2015) at the AIM site.....	35
Figure 4.6: Comparisons between Lu_CNR4 and Lu_CNR1 for a two-day period (27 th and 29 th July 2015) at the AIM site.....	35
Figure 4.7: Comparisons between R_n_CNR4 and R_n_CNR1 for a two-day period (27 th and 29 th July 2015) at the AIM site.....	36
Figure 4.8: The regression plot of R_n_CNR4 vs R_n_CNR1 for a two-day period (27 th and 29 th July 2015) at the AIM site.....	37

Figure 4.9 : Radiative fluxes above open water at Midmar Dam for clear-sky (3 th March 2016) and overcast conditions (8 th March 2016).....	
Figure 4.10: The diurnal variability of reflection coefficient of water at Midmar Dam for the 29 th March 2016 (cloudless).....	41
Figure 4.11: The temporal graph showing the daily reflection coefficient of water measured at Midmar Dam from 24 th February to 4 th April 2016.	41
Figure 4.12: The temporal graph showing the calculated daily rRs and observed daily rRs above open water at Midmar Dam from 24 th February to 4 th April 2016.	42
Figure 4.13: The diurnal variation of the air temperature and surface water temperature at Midmar Dam for the 6 th March 2016 (cloudless).....	43
Figure 4.14: Temporal graph showing variability of the daily-average T_{air} and SWT at Midmar Dam from 24 th February to 4 th April 2016.	44
Figure 4.15: The spatial variability of SWT across Midmar Dam for the 25 th February 2016 (cloudless) at 09h50.	
Figure 4.16: The diurnal variability of G measurements at different water depth increments for Midmar Dam for the 1 th March 2016 (cloudless).....	48
Figure 4.17: Temporal variability of G measurements at different water depth increments for Midmar Dam from 24 th February to 4 th April 2016.	48
Figure 4.18: The diurnal variation in the measured 30-min fluxes of G and Rn for the 26 th February (DOY 56) 2016 (cloudless).....	49
Figure 4.19: The diurnal variation in the measured 30-min fluxes of G and Rn for the 13 th March (DOY 66) 2016 (cloudless).	50
Figure 4.20: Temporal graph showing the variability of G and Rn measurements for Midmar Dam from 24 February to 4 April 2016.	50
Figure 4.21: The regression graph of the daily G vs Rn for Midmar Dam from 24 February to 4 April 2016.	51
Figure 4.22: Regression graph of Rs_{water} and Rs_{land} for the period between 24 th February and 9 th March 2016 at Midmar Dam.	53

Figure 4.23: Temporal variation in <i>Tair water</i> and <i>Tair land</i> for the period between 24 th February and 9 th March 2016 at Midmar Dam.....	53
Figure 4.24: Regression plot of <i>Tair water</i> vs <i>Tair land</i> for the period between 24 th February and 9 th March 2016 at Midmar Dam.	54
Figure 4.25: Temporal variation in <i>U water</i> and <i>U land</i> for the period between 24 th February and 9 th March 2016 at Midmar Dam.	54
Figure 4.26: Temporal variation in <i>RH water</i> and <i>RH land</i> for the period between 24 th February and 8 th March 2016 at Midmar Dam.....	55
Figure 4.27: Regression plot of <i>RH water</i> vs <i>RH land</i> for the period between 24 th February and 8 th March 2016 at Midmar Dam.	55
Figure 4.28: The comparison between the daily measured and the simulated <i>Rs</i> above open water at Midmar Dam from 24 th February to 4 th April 2016.....	57
Figure 4.29: The regression graph of the measured and the simulated <i>Rs</i> above open water at Midmar Dam from 24 th February to 4 th April 2016.	57
Figure 4.30: The comparison between the daily measured and the simulated <i>Ld</i> above open water at Midmar Dam from 24 th February to 4 th April 2016.....	58
Figure 4.31: The comparison between the daily measured and the simulated <i>Lu</i> above open water at Midmar Dam from 24 th February to 4 th April 2016.....	59
Figure 4.32: The comparison between the daily measured and the simulated <i>Rn</i> above open water at Midmar Dam from 24 th February to 4 th April 2016.....	60
Figure 4.33: The regression graph of the measured and the simulated <i>Rn</i> above open water at Midmar Dam from 24 th February to 4 th April 2016.	60
Figure 4.34: The comparison between the daily measured and the simulated <i>Ld</i> for the Stratus station of the East Pacific Ocean from 10 th September to 24 th October 2016.....	63
Figure 4.35: The comparison between the daily measured and the simulated <i>Rn</i> for the Stratus station of the East Pacific Ocean from 10 th September to 24 th October 2016.....	64
Figure 4.36: The regression graph of the measured and the simulated <i>Rn</i> for the Stratus station of the East Pacific Ocean from 10 th September to 24 th October 2016.	64

Figure 4.37: Temporal variation in annual average daily R_n for the period between year 1966 and 2015 (inclusively) at Midmar Dam. 66

Figure 4.38: Temporal variation in annual average daily R_s for the period between year 1966 and 2015 (inclusively) at Midmar Dam. 67

Figure 4.39: Temporal variation in annual average daily L_u for the period between year 1966 and 2015 (inclusively) at Midmar Dam. 67

Figure 4.40: Temporal variation in annual average daily L_d for the period between year 1966 and 2015 (inclusively) at Midmar Dam. 68

Figure 4.41: Temporal variation in annual average daily air temperature for the period between year 1966 and 2015 (inclusively) at Midmar Dam. 69

CHAPTER 1 : INTRODUCTION

1.1 Background

South Africa is a water-scarce country where annual evaporation exceeds annual rainfall in most parts of the country. According to DWAF (2013), the mean annual precipitation of 450 mm in South Africa is far below the global mean annual precipitation of about 860 mm. The high temporal and spatial variability of rainfall in semi-arid regions such as South Africa results in water resources being not uniformly distributed throughout the region (Mukheibir, 2007). To ensure water security at various times of the year, water is stored in reservoirs (DWAF, 2013). Water demands due to increases in human population and economic development are projected to increase in the near future, resulting in a greater gap between supply and demand under current water resources management habits which involves storing water in open dams (McKenzie and Craig, 2001). CSIR (2010) reported that about 70 % of the total mean annual runoff is captured in about 569 large dams in South Africa.

Significant amounts of water may be lost from open water storages to the atmosphere as water vapour and this phenomenon is referred to as an open water evaporation (McJannet *et al.*, 2013). Schulze (2011) stresses the seriousness of water loss from open water storages in South Africa given the projected increase in evaporation due to climate change reported by Mukheibir and Sparks (2003). Evaporation rates information is required by water resources managers for many different purposes such as irrigation scheduling, management of wetlands, catchment water balance studies, dam design, and municipal and industrial water allocations (Finch and Hall, 2001). Estimation of evaporation rates is important in the study of soil, plant and atmosphere continuum as well as in hydrology and climate studies (McMahon *et al.*, 2013). However, water resources managers often overlook the open water evaporation from dam storages, leading to inefficient dam operating rules and poor water allocations (van Dijk and van Vuuren, 2009).

Evaporation is a significant component in the hydrological cycle and it is therefore critical that it can be understood and quantified (Savage *et al.*, 2004). There are several methods that have been successfully applied to estimate open water evaporation worldwide. However, each technique applies to a specific spatial and temporal scale, and some are therefore more suitable than others under specific conditions (Tanny *et al.*, 2008). According to Savage (2010), currently there is no single accepted method that is reliable and results in adequate resolution

that can provide accurate temporal and spatial evaporation measurements or modelling estimates of open water evaporation. According to Finch and Hall (2001), each method has its own advantages and disadvantages, in terms of the method, theoretical assumptions, accuracy, complexity, cost, fetch requirements and power consumption. The choice of the technique to be used is highly dependent on the availability of data, level of accuracy of the output results and the representation of results (Finch and Hall, 2001).

There is a vital need to develop and improve the relatively inexpensive methods to estimate open water evaporation from readily available measurements with reliable accuracy and acceptable precision to calibrate new technologies. For operational purposes, such as water resources management, irrigation management and hydrologic studies, where near real time estimates of evaporation are needed, the energy balance approach (Eq. 1.1) driven by the available energy flux (i.e. $R_n - G$) seems to be the most promising technique to estimate open water evaporation due to its superior resolution of measurements and data requirements (Huntington and McEvoy, 2011).

$$R_n - G = LE + H \quad (1.1)$$

where R_n is net irradiance (W m^{-2}) which is the net balance between the net solar irradiance and the net infrared irradiance at water surface, G is the water-stored heat flux (W m^{-2}), $R_n - G$ is the available energy flux for open water evaporation, E is evaporation flux ($\text{kg s}^{-1} \text{m}^{-2}$, equivalent to mm s^{-1}), $L = 2.43 \text{ MJ kg}^{-1}$ is the specific latent energy of vaporisation and H is the sensible heat flux (W m^{-2}).

The energy balance techniques are the most accurate methods of estimating open water evaporation after the direct measurement of the open water evaporation and are often used as a standard method against which other methods are compared (Finch, 2001). Mengistu and Savage (2010) showed that open water evaporation from reservoirs can be computed as a residual of the energy balance, given that R_n , G and H fluxes above water surface can be estimated or measured. According to Finch and Calver (2008), the main disadvantage of the energy balance techniques is the large number of the high frequency measurements required and the difficulties in measuring some of them. Consequently, energy balance techniques are a relatively expensive techniques and have only been used in intense research studies. The energy balance techniques for estimating open water evaporation require either estimation or

measurement of the available energy flux which may not be readily available in the water storage of interest, especially in developing countries (Duan, 2014). The lack of the available energy flux data above water storages hinders routine computations of the open water evaporation based on the energy balance methods (McJannet *et al.*, 2013). However, McMahon *et al.* (2013) argue that these limitations could be solved by using the models that estimate available energy flux from meteorological data that is readily available in most standard weather stations.

1.2 Justification

The Penman model (1948) combines aerodynamic and energy balance aspects, as well as meteorological factors, which can more accurately describe open water evaporation (Jensen, 2010). Monteith (1965) modified the Penman model by including a surface resistance term which resulted in the widely-used Penman-Monteith model. The original Penman model was based on assumption that there was no change in G , which resulted in poor estimation of open water evaporation (McCuen and Assmussen, 1973). Finch (2001) stresses the significance of considering G while estimating open water evaporation. Edinger *et al.* (1968) proposed the concept of equilibrium temperature which was defined by Finch (2001) as the equilibrium temperature at which water temperature is being driven to by the net heat exchange. Therefore, for water at the equilibrium temperature, the net heat flux exchange is zero (Finch and Hall, 2001). MacJannet *et al.* (2008) used the concept of equilibrium temperature with the Penman-Monteith model to account for G while assuming that the water body is uniformly mixed with no thermal stratification and the surface resistance of water is zero, and obtained good estimates of open water evaporation from different water storages of different sizes compared to the original Penman-Monteith model. The modified Penman-Monteith model was further developed by Savage *et al.* (2016) and implemented in Excel to incorporate the daily solar radiation estimation model introduced by Hargreaves and Samani (1982) which utilizes the daily minimum and maximum air temperature to infill any gaps of missing solar irradiance data. Therefore, in this study, the Daily Penman, Monteith, Equilibrium Temperature Hargreaves-Samani (DPMETHS) model of Savage *et al.* (2016), assuming energy balance closure, was used to estimate the available energy flux above open water. The development of the DPMETHS model is part of a Water Research Commission (WRC) project which aims to measure and model open water evaporation using land-based meteorological data. This WRC project considered the two aspects of the modelling of the open water evaporation i.e. energy

balance and radiation balance of the water surface. However, the focus of the current study was on the radiation balance of the water surface. The DPMETHS model utilises the concepts of equilibrium temperature to estimate the water-body temperature at the water storage using an iterative procedure. The estimated water-body temperature is essential for computing G and the outgoing infrared irradiance from the water surface (McMahon *et al.*, 2013). Consequently, water-body temperature is one of the paramount parameters in the model and yet it is rarely measured above water storage. Furthermore, the temporal and spatial variability of water-body temperature on water storages are not well understood (Duan, 2014).

The DPMETHS model to estimate the available energy flux for open water evaporation is on its developmental stage and has not been used in any known study. Therefore, the estimates of the available energy flux from the DPEMETS model need to be tested for goodness of fit against measurements of the available energy flux under different climatic conditions before the model can be utilised with confidence to estimate the available energy flux for open water evaporation from the land-based measurements. Unless this is the case, the DPMETHS model is unlikely to be accepted by users other than the model developers. Therefore, there was a need to evaluate the performance of the DPMETHS model to estimate the available energy flux above water at different climatic conditions using the land-based meteorological data. However, there was a vital need to understand the factors enhancing temporal and spatial variability of the radiation balance at water storage for accurate modelling of the available energy flux at water storage.

Climate change is predicted to hit South Africa harder than countries in the north and will be felt first through its impacts on scarce water resources of this region (Schulze, 2011). Climate change has already altered, and will continue to alter the different components of the hydrological cycle such as evaporation (IPCC, 2014). However, the impacts of climate change on evaporation are not yet fully understood given that different components of evaporation will be affected differently (CSIR, 2010). Furthermore, the lack of a long-term record of R_n data over water surface hindered the evaluation of the potential impacts of climate change on the R_n , one of the drivers of open water evaporation. The availability of long-term meteorological dataset at Cedara station near Midmar Dam enables the unique opportunity to investigate the potential impacts of climate change on the radiation balance of Midmar Dam. Therefore, this current study also investigates the potential impacts of climate change on the radiation balance of Midmar Dam.

1.3 Aim

Available energy flux on water storages is the main driver of the energy balance techniques for estimating open water evaporation and yet are measured with difficulty. The main aim of this study was to understand the factors enhancing temporal and spatial variability of the radiation balance at water storage and to evaluate the performance of the DPMETHS model to simulate the available energy flux above open water at Midmar Dam and for an eastern Pacific Ocean site.

1.4 Objectives

- To improve an understanding of the variability of the radiation balance and available energy above open water storage and assessing the factors that affect the radiation balance above open water;
- To evaluate the performance of the DPMETHS model to simulate the daily available energy flux at Midmar Dam and at the ocean Pacific Ocean;
- To investigate the potential impacts of climate change on the radiation balance of Midmar Dam.

1.5 Outline of dissertation

Chapter 1 introduces the study with an overview of the significance of an available energy flux on quantifying open water evaporation. The models that have been successfully used to estimate an available energy flux from the standard meteorological data are also introduced.

Chapter 2 provides detailed information on the radiation balance of the open water surfaces and focuses on the factors that control the temporal and spatial variability of the radiation balance components. The theoretical background of measuring and modelling the available energy flux at open water surfaces is also explained explicitly.

Chapter 3 provides the detailed procedure used on both laboratory and outdoor calibrations of the instrumentation at the Agrometeorology Instrument Mast system. The procedure on the

experiment set-up at Midmar Dam is also provided. The detailed procedure for data collection, data processing and data analysis is also explained explicitly.

In Chapter 4 the radiation data acquired from the water-based station were compared against the radiation data from Agrometeorology Instrument Mast system for the same period. The factors that control the temporal and spatial variability of the radiation balance of the Midmar Dam were investigated. The temporal variability of the available energy flux at Midmar Dam was also investigated. Furthermore, the performance of the DPMETHS model to simulate daily radiative fluxes at Midmar Dam and at the ocean was also evaluated.

Chapter 5 provides the summary of the conclusions and recommendations for future research.

CHAPTER 2 : LITERATURE REVIEW

2.1 Radiation balance

2.1.1 Introduction

The net radiation balance is the balance between the net solar radiation and net infrared radiation under steady atmospheric conditions (illustrated in Figure 2.1). This sub-section aims to improve the understanding of the radiation balance at water surfaces. The factors enhancing temporal and spatial variability of the radiation balance at water surfaces are also explained. Furthermore, the methods used to estimate available energy flux are also explained explicitly.

2.1.2 Radiation balance above open water surface

The term radiation refers to the continual emission of energy from the surface of all bodies with temperature greater than 0 K (Liou, 2002). However, Howell *et al.* (2010) defined radiation as the transmission of energy from one body to another by means of electromagnetic waves with or without intervening physical medium. Incoming solar radiation from the sun referred to as shortwave irradiance (R_s) may be defined as the radiation in the visible and near-visible portions of electromagnetic spectrum that is within the range of wavelength 250 to 2800 nm (Dozier, 1980). Howell *et al.* (2010) defined R_s which includes both direct and diffuse shortwave radiation as the radiant energy reaching a horizontal plane at the earth's surface. Furthermore, R_s is expressed as energy amount per unit time per unit interval. The diffuse radiation component can be noticed by blocking out the sun's direct rays and observing the diffuse component (Sinclair *et al.*, 1992). Liou (2002) referred to the sum of the direct and diffuse components as the total solar radiation (which excludes infrared radiation).

Some of R_s in the form of shortwave radiation reaches the water bodies in diffused form, after scattering by clouds, dust and different gases such as nitrogen, oxygen and ozone in the atmosphere (Allen *et al.*, 1998). Furthermore, part of the R_s that actual reaches the water body is reflected into space (Figure 2.1). The reflection coefficient depends on transient factors, such as the angle of incidence of the solar beam, colour and the nature of the surface (Allen *et al.*, 1998). The reflection coefficient of water is much lower than that of vegetation. Consequently, the water surface absorbs more solar irradiance than vegetation (Arya, 2001). Finch and Hall (2001) reported that about 92% of the solar irradiance striking the surface of the water body is

absorbed. Finch and Calver (2008) argue that the amount of absorption is highly dependent on the wavelength of the radiation i.e. near-infrared radiation is absorbed much less as compared to blue light. The reflection coefficient of water directly determines the amount of solar irradiance absorbed by the water surface (Brutsaert., 2013). According to Allen *et al.* (1998), the reflected solar irradiance cannot be absorbed or transmitted through the water surface. Therefore, reflected solar irradiance is not utilized on water surface.

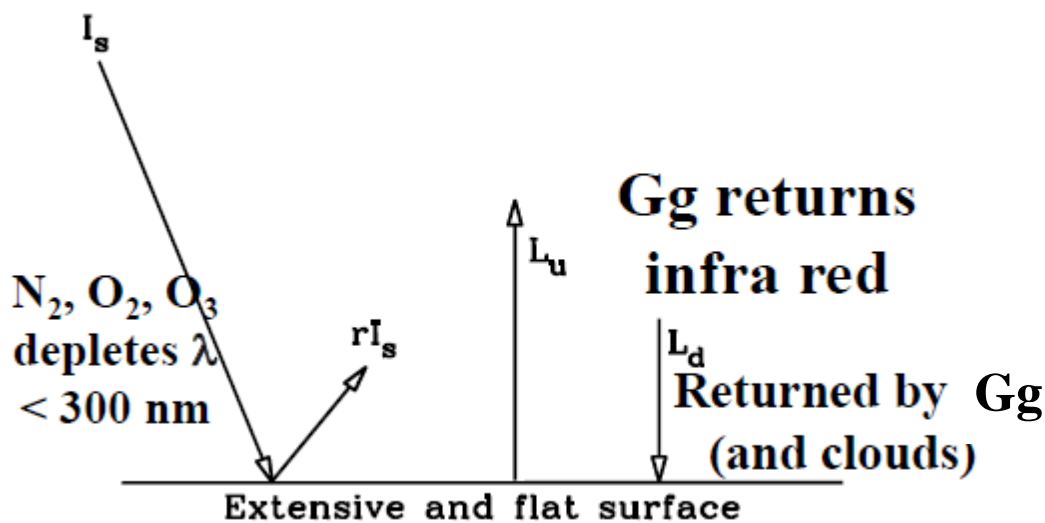


Figure 2.1: Schematic diagram showing radiation balance on earth's surface, where Gg are the greenhouse gases (Savage, 2012).

The absorbed solar irradiance from the sun on water surface is converted to heat energy which excites electrons and warms the top layer of water (Jensen, 2010). According to Finch and Calver (2008), most of the solar irradiance is absorbed within the top one meter of the water surface. Water surface is the primary energy storage medium mainly due to its high heat capacity compared to vegetation, soil minerals, and soil organic matter (Brutsaert, 1982). For vegetation, the partitioning of the solar irradiance is straight forward and the soil heat flux tends to be relatively small. Therefore, solar irradiance absorbed at the soil surface, is the available energy flux for evaporation. However, for open water, solar irradiance penetrates the water column and absorbed at greater depths and is not immediately available for open water evaporation (Granger and Hedstrom, 2011). The quantity of the solar irradiance that penetrates the water column is highly dependent on the colour of water and turbidity (Finch and Hall,

2001). Finch and Calver (2008) noted that the absorbed solar irradiance is transferred to greater depths through movement from wind and convection while heat is slowly transferred throughout the water column, it often does not reach all the way to the bottom. Furthermore, the lowest strata of water remained near 4 °C, while the surface water temperature fluctuated both diurnally and seasonally (Finch and Calver, 2008).

According to Liou (2002), if the water surface could only absorb energy, the temperature of the water will be infinitely rising. The temperature of water is much lower than that of the sun, therefore, water emits infrared radiation with wavelengths longer than those from the sun (Henderson-Sellers, 1996). Gates (1980) defined emitted infrared radiation (L_u) as the radiation originating at terrestrial sources with temperatures ranging between 200 and 370 K and have wavelengths greater than 2800 nm. The quantity of L_u is highly dependent on the surface water temperature, humidity and emissivity at low latitudes (Allen *et al.*, 1998). According to Liou (2002), most of the radiant energy emitted by the water surface is contained in the wavelength region of 4000 to 10000 nm and can be explained by Stefan–Boltzmann law based on radiant energy emission by a black body as:

$$L_{u\text{ wet}} = \varepsilon\sigma T^4 \quad (2.1)$$

where ε is the emissivity of the water surface, σ is the Stefan-Boltzmann constant (5.67×10^{-8} W m⁻² K⁻⁴) and T is the surface water temperature of the surface (K).

In the atmosphere, greenhouse gases and clouds selectively transmit, absorbed or reflect L_u (Liou, 2002). According to Kirchhoff's law it is apparent that L_u that is absorbed by the atmosphere would be reradiated (Koberg, 1964). Consequently, greenhouse gases such as water vapour and carbon dioxide on the atmosphere emit infrared radiation in all directions (Koberg, 19964). According to Gates (1980), some of L_u goes back to the water surface while some of it escapes in the atmospheric window into space (Figure 2.1). Ohring and Clapp (1980) defined atmospheric window as the transparent region, with wavelength of about 7000 to 12000 nm where neither water vapour nor carbon dioxide absorb appreciable radiation. Therefore, during clear-skies, energy of that wavelength band passes through the atmosphere unimpeded. According to Stefan-Boltzmann law, if the water surface is warmer than the overlaying atmosphere which is the normal state of affairs, the atmosphere will receive more terrestrial radiation than it emits (Liou, 2002). Arya (2001) reported that about 90 % of the infrared

radiation radiated to space by the earth, is absorbed by the atmosphere. Furthermore, much of this infrared radiation is sent back or counter radiated to the water surface and effectively prevents the water surface from excessive cooling at night. The re-radiation back of infrared radiation to the earth is called the greenhouse effect and keeps the earth's temperature almost constant (Ramanathan *et al.*, 1989). Brunt (1934) showed that the incoming infrared irradiance (L_d) can be expressed by:

$$L_d = \sigma T^4 \left[0.44 + 0.08 \left(\frac{e_{air}}{100} \right)^{0.5} \right] \quad (2.2)$$

where the emissivity is assumed to be unity, T is the surface air temperature (K) and e_{air} is the atmospheric water vapour pressure (Pa).

According to de Bruin (1982), R_n is given by:

$$R_n = R_s + rR_s - L_u + L_d \quad (2.3)$$

All terms are in $W m^{-2}$. L_u depends on surface water temperature and emissivity while L_d is influenced by atmospheric temperature, humidity, and cloud fraction (Finch and Calver, 2008). The sign convention used in Eq. (2.3) is that all the radiative fluxes directed toward the water surface are positive while the radiative fluxes directed away from the water surface are negative.

2.2 Diurnal and seasonal variability of the radiation balance

The downward components of the radiation balance are controlled by the solar zenith angle which varies with time of the day, season, and latitude (Wang and Liang, 2009). Furthermore, the downward components of the radiation balance are controlled by the atmospheric conditions such as the amount and composition of clouds, atmospheric water vapour amount, and aerosol loading. According to Federer (1968), the downward components of the radiation balance can be assumed to be relatively constant over relatively large surface areas except under partially cloudy skies. The amount of R_s reaching water surface depends on the turbidity of the atmosphere and the presence of clouds which reflect and absorb major parts of the radiation (Finch and Calver, 2008). Therefore, cloud amount and type are important, as well as latitude, season and time of the day in determining the solar radiation reaching water surface. Clouds cover increase scattering and absorption of the solar radiation in the atmosphere (Finch and Hall, 2001). Consequently, less R_s reaches the earth's surface during cloudy or overcast days than during clear-sky days. Allen *et al.* (1998) reported that on clear-sky day, incoming solar radiation is about 75 % of the extraterrestrial radiation while on an overcast day, the radiation

is scattered in the high turbidity atmosphere, however about 25 % of the extraterrestrial radiation may still reach the earth's surface mainly as diffuse sky radiation. The intensity of R_s increases from sunrise until noon and then decrease until sunset and the peak solar energy levels received will vary by latitude and season (Arya, 2001). The intensity of R_s received at the earth's surface depends on the sun and the sun's angle (Blonquist *et al.*, 2010). Therefore, different locations of the globe have different typical solar radiation levels in each season. According to Hatzianastassiou and Vardavas (2001), at the beginning of the year the intensity of R_s is high and then slowly drops to their lowest point around June in the southern hemisphere. After June, it begins to rise again for the rest of the year and reach the peak in December or January.

The upward components of the radiation balance are controlled by the water surface characteristics such as reflection coefficient of water surface, water emissivity, surface water temperature (*SWT*) and humidity above the water surface (Finch and Hall, 2001). The fluxes of R_n above water surface shows a substantial daily and seasonal variation (Wang *et al.*, 2014). According to Brotzge and Duchon (2000), R_s is the dominant component of R_n during the day. However, infrared irradiance is the dominant component of R_n during night. Mahmud *et al.* (2015) noted that during the daytime, R_n was directed towards the water surface while at night the R_n was much smaller in magnitude and directed away from the water surface. Consequently, the water surface warmed up during the daytime, while it cooled during the night-time, especially during the clear-sky and calm weather conditions.

2.1.4 Spatial variability of the net irradiance above water surface

Sima *et al.* (2013) reported that open water evaporation was under-estimated when point measurements of *SWT* were used instead of the satellite-derived averaged *SWT*. These results were attributed to the higher shoreline measurements of *SWT* than the satellite-derived *SWT* which resulted on over-estimation of the net infrared irradiance which reduced R_n . According to Wang *et al.* (2014), any spatial variation of R_n above open water is mainly due to the spatial variability in *SWT*. According to Alcântara *et al.* (2010), the main meteorological factors influencing variability of *SWT* are solar irradiance and wind speed. However, Kristovich and Laird (1998) argue that cloudless is also one of the significant factors determining variability of *SWT*. Finch and Hall (2001) stresses that the spatial variation in *SWT* can be large over

short-time scales during calm conditions and clear sky days with high solar irradiance. However, Swancar (2015) reported that energy exchange due to water-stored heat flux also had a significant influence on *SWT* at Lakes Calm and Starr. According to Alcântara *et al.* (2010), during daytime, water near the shore responded to the atmospheric conditions very quickly compared to offshore water. As consequence, water near the shore is always warmer than offshore water. However, during night-time the processes are inverted.

McMahon *et al.* (2013) argued that the *SWT* data are not readily available at standard automatic weather stations and difficult to measure due to high wind turbulence at water surface. According to Lamaro *et al.* (2013), conducting water temperature surveys using conventional limnological sampling involves significant financial investment in instrumentation and extensive field work on a reservoir. Furthermore, *SWT* for larger reservoirs are directly measured with great difficulty and high uncertainties due to high spatial variation in *SWT* over short-time scale. Consequently, spatial variability of *SWT* is often estimated using several satellites with relative accuracy (Steissberg *et al.*, 2005). Furthermore, satellites provide synoptic and frequent data acquisition over large areas (Alcântara *et al.*, 2011). According to (Chuvienco, 2002, cited by Lamaro *et al.*, 2013), satellite information allows to obtain data in digital format that can be easily combined with other geographic information and used to generate quantitative models. The Landsat-8 images are freely distributed through the U.S. Geological Survey and is the one of the satellites that has been used to assess spatial variability of *SWT* in reservoirs (e.g. Alcântara *et al.*, 2010). Sima *et al.* (2013) reported good agreement between Landsat-8 estimates of *SWT* and the *in-situ* measurements *SWT*. Landsat-8 was officially launched in year 2013 and deployed into orbit with two instruments on-board of which one is the Thermal Infrared Sensor (TIRS) with two spectral bands in the long-wave infrared that can be used to retrieve *SWT* (Rozenstein *et al.*, 2014). The satellite-derived *SWT* need to be calibrated with long-record of ground truth *SWT* data which may not be always readily available in the reservoir of interests (Schott *et al.*, 2001). Furthermore, the thermal infrared data from the satellite need to be corrected for the emissivity and atmospheric effects for quantitative assessment of *SWT* (Li *et al.*, 2013). The major limitation of using Landsat-8 data to access daily variability of *SWT* is that this satellite acquire data once in every 16 days at any given location and does not record data at night (Alcântara *et al.*, 2011). Furthermore, the spatial resolution of the TIRS data of 100 m limits the application of the Landsat-8 data on assessing

variability of SWT over small irrigation waters storages and open lakes (Rozenstein *et al.*, 2014).

2.2 Available energy flux for open water evaporation

2.2.1 Introduction

The difference between R_n and G fluxes, is a measure of the available energy flux that drive the processes of open water evaporation in a reservoir (Finch and Calver 2008).

2.2.2 Measuring available energy flux

Federer (1968) argues that if water is unlimited at the evaporative surface, the energy flux used in evaporation (latent energy) may be equal to the R_n which is generally measured by a net radiometer. However, Finch and Gash (2001) stress the significance of considering G in the energy balance techniques and concluded that the accurate measurement or estimation of G is a paramount input parameter for open water evaporation studies. According to Mengistu and Savage (2010), G is determined from water temperature profile measurements using the (Brutsaert, 1982) equation as:

$$G = \rho_w c_w \Delta z \frac{\Delta T_w}{\Delta t} \quad (2.4)$$

where ρ_w is the density of water, c_w is the specific heat capacity of water, Δz is the depth increment in water profile, ΔT_w is the average water temperature difference from one averaging time to another for depth increment and Δt is the change in time for the averaging period.

2.2.3 Modelling available energy flux

Geraldo-Ferreira *et al.* (2011) argues that R_n is not strictly a micrometeorological parameter due to its dependency on the temperature, emissivity and reflection of the underlying surface. Furthermore, R_n is measured with difficulty since it is the sum of four distinct variables. Consequently, R_n is measured in only a few number of standard weather stations. According to Dong *et al.* (1992), net radiometers are expensive, requiring continuous calibration and maintenance to ensure accurate estimates of R_n . Furthermore, Dong *et al.* (1992) noted that the net radiometers that are placed permanently in the field are subject to damage by ultraviolet radiation, which degrades both the black sensing surfaces and the polyethylene domes. Geraldo-

Ferreira *et al.* (2011) argues that meteorological data measured in standard meteorological stations can be used to model R_n in order to replace the use of the expensive net radiometers. The number of models used to estimate R_n from standard meteorological data varies with the level of complexity and data input requirements (Wang *et al.*, 2009). These models require measurements of the solar irradiance, air temperature and water vapour pressure (Blonquist *et al.*, 2010). Iziomon *et al.* (2000) stressed that R_n should be determined from models which are universally applicable and relatively easy to utilise.

Brutsaert (1982) showed that G can be indirectly determined from water temperature profile measurements obtained by thermocouples. However, the lack of the temporal and spatial water temperature profile data at water storages hinders routine estimation of G from water temperature profile (Winter *et al.*, 2003). Tanny *et al.* (2008) argued that turbulent water waves of different temperatures travelling past the thermocouple could result in significant errors on G estimated from water temperature profile. Consequently, G is often estimated using heat storage models for lakes based on the readily available data at the nearby meteorological weather station and some characteristics of the water storage such as water level and turbidity (Duan, 2014).

The Penman model applied to open water by Penman (1948) was the first equation to combine both energy balance and aerodynamic aspects to estimate daily evaporation (McMahon *et al.*, 2013). The energy balance aspect depends on the solar irradiance which provides the energy required to evaporate water while the aerodynamic aspect depends on wind, humidity, and temperature by which energy is removed from the evaporative surface (King *et al.*, 2015). According to McMahon *et al.* (2013), this approach eliminates SWT parameter which is not readily available at standard automatic weather stations and difficult to measure due to high wind turbulence at water surface. Monteith (1965) modified the Penman model by including a surface resistance term which resulted in the widely-used Penman-Monteith model. Penman-Monteith model is a physically based equation that has been successfully applied in many different locations worldwide to estimate both open water evaporation and evaporation from different vegetation covers (Finch and Hall, 2001). When the Penman-Monteith model is applied to estimate open water evaporation, it requires land-based inputs of the solar irradiance, sunshine hours or cloudiness, air temperature, relative humidity and wind speed from a nearby

weather station which are used to calculate R_n (McMahon *et al.*, 2013). Valiantzas (2006) noted that one of the disadvantages of the Penman-Monteith model is that R_n is usually computed indirectly from the readily available meteorological data measured at the nearby automatic weather stations.

The main limitation of the Penman-Monteith model is the lack of validity of an assumption that the water column is well mixed and there is no change in G (Finch and Gash, 2001). Edinger *et al.* (1968) proposed a useful model based on the concept of an equilibrium temperature and associated time constant, determined from land-based meteorological data to estimate G (Finch, 2001). According to McMahon *et al.* (2013), the equilibrium temperature model has been developed further by Keijman (1974), Fraederich *et al.* (1977), de Bruin (1982) and Finch and Gash (2002). McJannet *et al.* (2008) noted that a modification of the model was since deeper water bodies can store more heat than shallow water bodies. Consequently, they are not in thermal equilibrium and the surface temperature may be greater than or less than the equilibrium temperature. Finch (2001) defined equilibrium temperature as the temperature which the water temperature is being driven to by the net energy flux exchange. For water at the equilibrium temperature, the net rate of energy flux exchange is zero (Finch and Hall, 2001). From this, an expression for the temperature of a well-mixed body of water as a function of time and water depth was derived. The water-body temperature estimated from this expression can then be used to calculate G and L_u from the water surface (Finch and Calver, 2001). McJannet *et al.* (2008) used the concept of equilibrium temperature applied to the Penman-Monteith model to account for G . The modified Penman-Monteith model allows adjustment to the amount of the energy available flux for evaporation based on changes in G (McJannet *et al.*, 2008).

2.2.4 Description of the DPMETHS model for computing available energy flux

The model description provided by McJannet *et al.* (2008) form the basis of the daily time-step DPMETHS spreadsheet implemented model of Savage *et al.* (2016) that is used in this study to estimate available energy flux. The DPMETHS model computes available energy flux from the daily measurements of R_s , maximum and minimum air temperature (T_{air}), minimum and maximum relative humidity (RH) and wind speed (U) acquired at nearby land-based weather station. According to Finch and Hall (2001), R_s reaching the water surface is reduced by rR_s based on the reflection coefficient of water surface (r) and net outgoing infrared irradiance.

According to de Bruin (1982), the net infrared irradiance is calculated from T_{air} at 09h00, the estimated daily-average water temperature and cloudiness factor (C_f) while R_n at water surface is calculated from:

$$R_{net\ wet} = R_s - rR_s + L_d - L_{u\ wet} \quad (2.5)$$

where r is approximately 0.08 (Finch and Hall, 2001) and L_d is calculated from:

$$L_d = \sigma(T_a + 273.15)^4(C_f + (1 - C_f)(1 - 0.261 \exp(-7.77 \times 10^{-4} T_a^2))) \quad (2.6)$$

where $\sigma = 4.9 \times 10^{-9} \text{ MJ m}^{-2} \text{ K}^{-4}$ is the modified for daily time-scale Stefan-Boltzmann constant. C_f is determined using the procedure presented by Jegede *et al.* (2006):

for $I_s/I_{s\ clear} \leq 0.9$, where:

$$I_{s\ clear} = I_{s\ extra}(0.75 + 2 \times 10^{-5} h) \quad (2.7)$$

where $I_{s\ clear}$ is the clear-sky solar irradiance (MJ m^{-2}), and where $I_{s\ extra}$ is the extra-terrestrial solar irradiance (MJ m^{-2}) and h is the site latitude (m). $I_{s\ extra}$ is calculated using standard astronomical equation involving day of year, latitude, declination and sunset hour angle, then:

$$C_f = 1.1 - I_s/I_{s\ clear} \quad (2.8)$$

Otherwise if $I_s/I_{s\ clear} > 0.9$ then:

$$C_f = 2(1 - I_s/I_{s\ clear}) \quad (2.9)$$

In Eq. 2.5, $L_{u\ wet}$ is the outgoing infrared irradiance emitted by the water surface at temperature T_{water} (K) and is calculated using:

$$L_{u\ wet} = 0.97\sigma(T_{water} + 273.15)^4 \quad (2.10)$$

$L_{u\ wet}$ (MJ m^{-2}) is approximated using Taylor series expansion at T_a by:

$$L_{u\ wet} = 0.97\sigma(T_a + 273.15)^4 + 4\sigma(T_a + 273.15)^3(T_{water\ i-1} - T_a) \quad (2.11)$$

where the factor 0.97 corresponds to the emissivity of water (Anderson 1954, cited by Jensen, 2010) and T_a is the air temperature at reference height ($^{\circ}\text{C}$).

Within the DPMETHS model, changes to water-body temperature and G are highly susceptible to the equilibrium temperature and a water-body time constant. The time constant is directly affected by the water depth and it governs the rate of change in water temperature between consecutive days as it dictates the time that would be required to reach equilibrium (McJannet *et al.*, 2008). The daily-average water temperature on day i , $T_{water\ i}$ ($^{\circ}\text{C}$), is calculated from

the average water temperature of the previous day ($T_{water\ i - 1}$), a water-body time constant τ (days) and an equilibrium temperature T_e ($^{\circ}\text{C}$):

$$T_{water\ i} = T_e + (T_{water\ i-1} - T_e) \exp(-t/\tau) \quad (2.12)$$

The τ is calculated based on the de Bruin (1982) method:

$$\tau = \frac{\rho_w c_w d}{4\sigma(T_{wet} + 273.15)^3 + f(U)(\Delta_{T_{wet}} + \gamma)} \quad (2.13)$$

where ρ_w is density of water (kg m^{-3}), c_w is the specific heat capacity of water ($0.004185 \text{ MJ kg}^{-1} \text{ K}^{-1}$), and d is the water depth (m), T_{wet} is the wet bulb temperature, γ is the psychrometric constant, $\Delta_{T_{wet}}$ ($\text{kPa } ^{\circ}\text{C}^{-1}$) is the slope of the temperature saturation water vapour vs temperature relationship curve at the wet bulb temperature and $f(U)$ is the wind functions that are usually derived empirically for particular location. The $f(U)$ above water is computed using the Harbeck (1962) method:

$$f(U_2) = 7.127A^{-0.05}U_2 \quad (2.14)$$

where $f(U_2)$ is the wind function for wind speed measured at a height of 2 m above the surface ($\text{MJ m}^{-2} \text{ kPa}^{-1}$) and A is the surface area of the water storage (m^2).

The equilibrium temperature, T_e ($^{\circ}\text{C}$), is calculated based on equation of de Bruin (1982):

$$T_e = T_{wet} + \frac{R_{net\ wet}}{4\sigma(T_{wet} + 273.15)^3 + f(u)(\Delta_{wet} + \gamma)} \quad (2.15)$$

The one-day change in heat energy flux storage of water, S (MJ m^{-2}) between day i and $i - 1$ is given by:

$$S = \rho_w c_w d (T_{water\ i} - T_{water\ i-1}) \quad (2.16)$$

CHAPTER 3 : METHODS AND MATERIALS

3.1 Study site description

The study was conducted at Midmar Dam at Umgeni Catchment in KwaZulu-Natal Midlands at about 3 km south-west of town Howick outside Pietermaritzburg, South Africa (29° 30'S, 30°10'E, elevation 985 m) from 7th July 2015 to 4th April 2016 (Figure 3.1). Some of the characteristics of the Midmar Dam are described in Table 3.1.

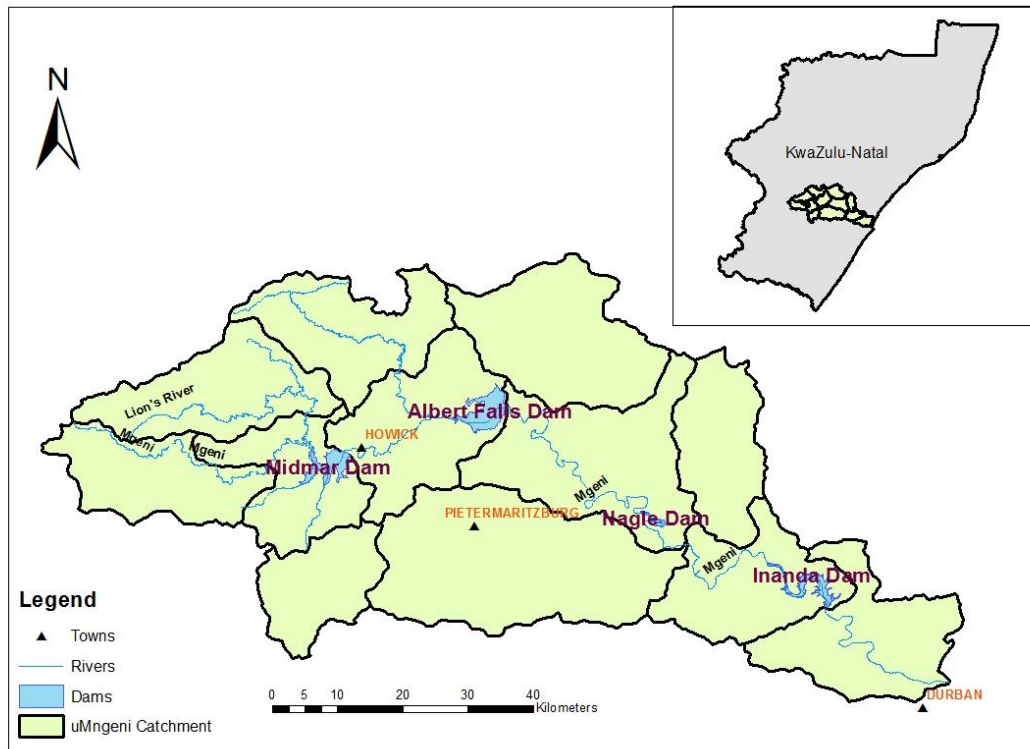


Figure 3.1: Map showing the location of the Midmar Dam in the Umgeni catchment in KwaZulu-Natal midlands.

The primary purpose of the dam is for municipal and industrial water use (Department of Water Affairs and Forestry, 2007). According to Simpson and Dickens (2006), Midmar Dam supplies approximately 374 million kilolitres of water to about 4.8 million people each year in the Howick, Pietermaritzburg and Durban regions. Midmar Dam is the first of a cascade of four large dams on the Umgeni River system (Figure 3.1). Outflow from Midmar Dam feeds Albert Falls Dam which subsequently feeds Nagle and Inanda Dams downstream (Simpson and Dickens, 2006). Consequently, the three large reservoirs in the Umgeni River system are directly affected by the quality and quantity of the outflow from Midmar Dam. According to Mengistu and Savage (2010), this area receives summer rainfall and the summer season is

characterized by warm and wet days with T_{air} exceeding 30 °C in summer while the winter season is characterized by cold and dry days with T_{air} below 20 °C and during night-time it may decrease to below 0 °C.

Table 3.1: Some characteristics of Midmar Dam (adapted from Mengistu and Savage (2010)).

Characteristic	Description
Location	29° 30'S, 30°10'E
Elevation	985 m
Mean maximum T_{air}	30 °C
Mean minimum T_{air}	20 °C
Mean annual precipitation	992 mm
Maximum daily evaporation	3.9 mm
A	1793.15 ha
Total capacity	235.5 Million m ³

3.2 Experimental setup

Land-based and water-based stations were used during the study. At the land-based station, measurements of R_s , T_{air} , RH , rainfall, U and wind direction were monitored. At the water-based station, measurements of the components of the R_n flux were monitored using a four-component net radiometer mounted at 1.5 m above the water surface. The measurements of the air temperature and relative humidity were also acquired at 1.5 m above water. The surface water temperatures were monitored using a pair of infrared thermometers with a field of view 22.0°, mounted at 1.5 m above the water surface. Furthermore, water temperatures at different depths of water were also monitored using Type-E thermocouples.

3.3 Instrumentation

The components of R_n are generally measured by net radiometers. There are different models of net radiometers available at the market. The comprehensive study of different net radiometers by Blonquist *et al.* (2009) revealed that accuracy of the estimates of R_n increases with the cost of the net radiometer and the four-component CNR4 net radiometer (Kipp & Zonen, Delft, Netherlands) was one of the most accurate net radiometers. Therefore, in this study a four-

component CNR4 net radiometer which was the most recent model of the radiometer with the most improved features was used. According to Kipp and Zonen (2014), the four-component CNR4 net radiometer consists of a pair of pyranometers and pyrgeometers, with one pair facing upward and the other pair facing downward. The pyranometer measures the solar irradiance while the pyrgeometer measures the infrared irradiance. The four-component CNR4 net radiometer covers the total spectral range between 0.3 and 42 μm , which covers both the solar radiation and the infrared radiation while the gap between these two produces negligible errors (Kipp and Zonen, 2014). The details of all equipment used in station systems are provided in Table 3.2.

Table 3.2: Details of the equipment used for land-based and water-based weather station systems at Midmar Dam during the study period.

Stations	Land-based	Water-based
Sensors	Solar irradiance (CM3 ¹), relative humidity and air temperature (HC2S3 ²), wind speed and direction (03002-L ³) all at 2 m and rain gauge (TR-525I ⁴) at 1.2 m	Net radiometer (CNR4 ⁵), relative humidity and air temperature (HC2S3 ²), two IRT (SI-111 ⁶) all at 1.5 m above water and five Type-E thermocouples at different water depths i.e. 20, 40, 80, 120, 160 mm water
Field Data loggers	CR1000 ⁷ . All measurements were every 5 s and averaged/totalled every 2 min, 60 min and daily time steps outputs	CR3000 ⁸ . All measurements were every 5 s and averaged every 30 min time step outputs
Power details	Connected to two 12 A h battery	Connected to a 12 A h battery
Data storage method	Stored in datalogger memory and SD card	Stored in SD card
Software	The station software included Loggernet 4.2 ⁸ for scheduled connection to data logger and download of data	The station software included Loggernet 4.2 ⁸ for scheduled connection to data logger and download of data

Data collection data were downloaded from the data were downloaded from the data method data logger and SD card using laptop logger and SD card using laptop

¹Pynarometer, Kipp & Zonen, Delft, Netherlands; ²RH and T probe, Campbell Scientific Inc., Logan, Utah, USA; ³RM Young wind sentry, Campbell; ⁴rain gauge, Texas Electronics, Inc, Shilling Way, Dallas, USA; ⁵net radiometer, Kipp & Zonen; ⁶infrared thermometers, Apogee Instruments Inc., Logan, USA; ⁷CR1000, Campbell; ⁸CR3000, Campbell; ⁹Loggernet, Campbell

3.4 Equipment testing and calibration

Before setting equipment at the experiment sites, laboratory test and calibration of equipment were done.

3.4.1 Laboratory equipment test

Laboratory tests were conducted to evaluate the performance and functioning of the different sensors used as well as to validate the created datalogger programs before deploying the equipment to the study sites. The main aim of these tests was to detect and replace any faulty sensor as well as to evaluate the correctness of the created datalogger programs.

3.4.1.1 Testing the land-based station sensors

The sensors for measuring R_s , T_{air} , RH , rainfall, U and wind direction as well as a rain gauge were connected to the CR1000 datalogger and monitored over a period. To test the air temperature and relative humidity sensor, a humid atmosphere was artificially created around the sensor by blowing on the sensor. Measurements of the air temperature and relative humidity were viewed through PC200W program (Campbell Scientific Inc.) which allowed observation of data at 5 s scan intervals. After blowing on the sensor, relative humidity readings rose as high as 95 % indicating that the sensor was working correctly. Temperature readings of the sensor averaged at 24 °C which was equal to the room temperature of the day, and partly indicated the correct functioning of the air temperature and relative humidity sensor. The greater measurements of the solar irradiance were observed when the light from the torch was directed to the sensor while solar irradiances were approximately zero when the sensor was shaded. These observations indicated the correct functioning of the pyranometer. The wind sentry was tested by blowing on the sensor with a fan. The greater wind speed measurements

were observed during the blowing on the sensor compared to sensor not blow on. These observations indicated the reasonable functioning of the wind sentry. The rain gauge was tested using a volume calibration. Measured amount of water were poured into the receiving area of the rain gauge using a syringe. The volume of water added was recorded each time the gauge tips. The manufacturer claims that the rain gauge tips after every 0.25 mm of water. The number of tips were in reasonable agreement with the volume of water added, which indicated the correct functioning of the rain gauge.

3.4.1.2 Testing the water-based station sensors

The procedure used to test the four-component CNR4 net radiometer at the laboratory was adapted from the procedure provided by Savage and Heilman (2009) based on the recommendations of Kipp and Zonen (2014). The four-component CNR4 net radiometer sensor was connected to the CR3000 datalogger and the components of R_n were monitored over a period. The test was conducted by directing the torch at the net radiometer sensors. The torch was shone on ‘up-facing’ and ‘down-facing’ sensors at different times, respectively. The data collected was viewed through PC200W program which allowed the observation of data at 5 s scan intervals. The observations showed a difference of less than 10 % after comparing the ‘up-facing’ pyranometer and the ‘down-facing’ one and the same was also noted for the pyrgeometer. The multimeter test using an alternating voltage was also conducted to further evaluate the functioning of the pyranometers and pyrgeometers in the net radiometer. When the pyranometers were shaded with hands, the solar irradiance readings were approximately zero. However, when the pyranometers were exposed to light, the positive readings of the solar irradiances were observed. The fluxes of the net short-wave solar irradiance which is the difference between incoming solar irradiance and the reflected solar irradiance were always positive. The values of the reflection coefficient which is the ratio of the incoming solar irradiance and the reflected solar irradiance were found to range between 0 and 1. These observations indicated the correct functioning of the pyranometers. When hot objects were placed in front of the pyrgeometers, the thermal radiation caused pyrgeometers to generate positive voltages since the surface temperature of the hot object was greater than the pyrgeometers temperatures. When the pyrgeometers were shone at the wall of the room, the thermal radiation caused pyrgeometers to generate negative voltages since the surface temperature of the wall was cooler than the pyrgeometers temperatures. These observations indicated the correct functioning of the pyrgeometers. The air temperature and relative humidity

sensor at water-based station was tested using the same procedure as the air temperature and relative humidity sensor for the land-based station. The comparisons between the measurements of the air temperature and relative humidity measured at water-based and land-based showed a difference of less than 5 %. These observations indicated the correct functioning of both air temperature and relative humidity sensors. The infrared thermometers were tested using the procedure of Savage and Heilman (2009).

3.4.2 Calibration of the station systems

Both systems were also setup at the Agrometeorology Instrument Mast system (AIM system) of Savage *et al.* (2014), for seven months (March to October of year 2015) to test the functioning of both instrumentation and datalogger programs in the outdoor as well as to calibrate the systems against the known standard AIM system before the systems. The AIM system is located (29.628 °S, 30.403 °E, at elevation of 671.3 m) near the Rabie Saunders Building of the University of KwaZulu-Natal, Pietermaritzburg, South Africa. The data acquired from both land-based and water-based station systems were compared against the data from the AIM system for the same period.

3.5 Systems set-up

After the calibration, land-based and water-based station systems were installed at Midmar Dam (Figure 3.2). The land-based station was installed near the dam at 100 m away from the shore on the 7th July 2015 while the water-based station was installed above water at 30 m away from the shore on the 12th February 2016 (Figure 3.3). The systems collected data between 12th February and 4th April 2016 for the current study apart from when there were power or data collection problems.

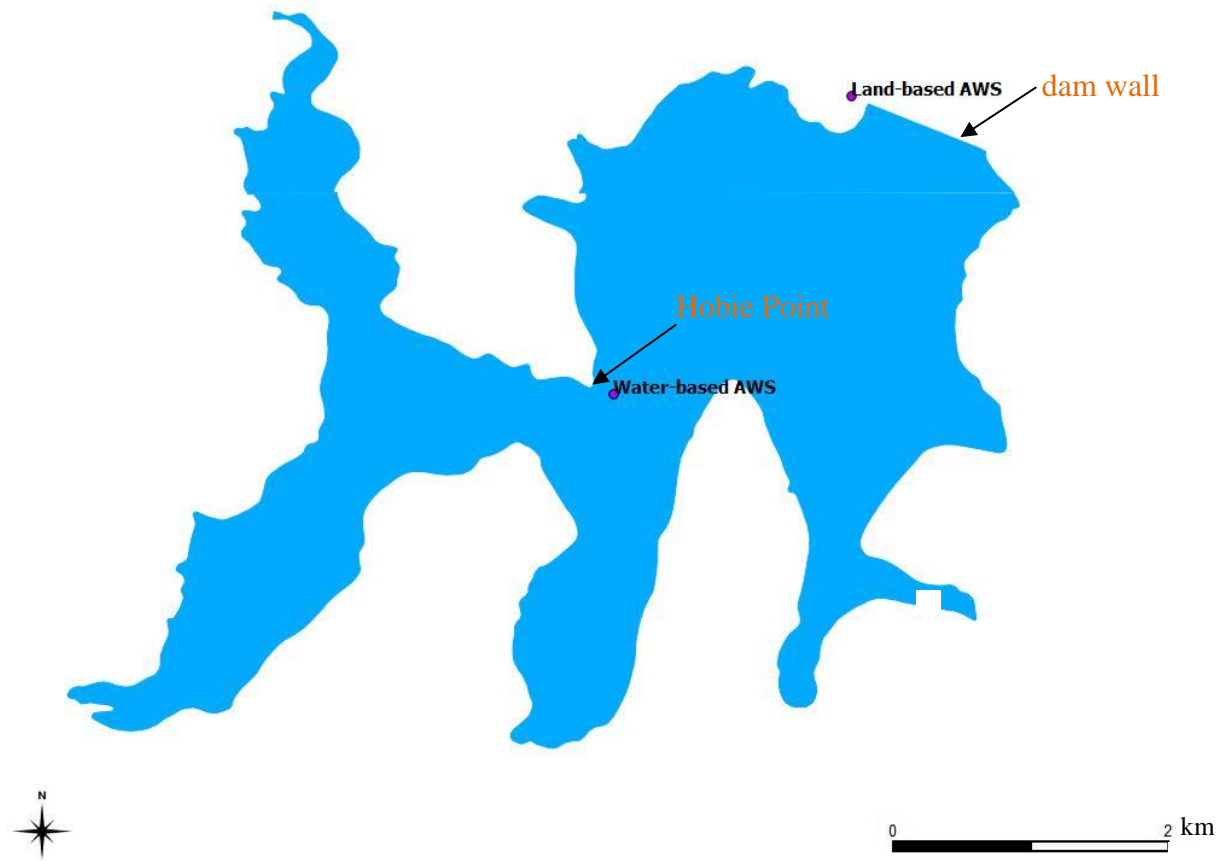


Figure 3.2: Location of the land and water-based stations at Midmar Dam during the study period.

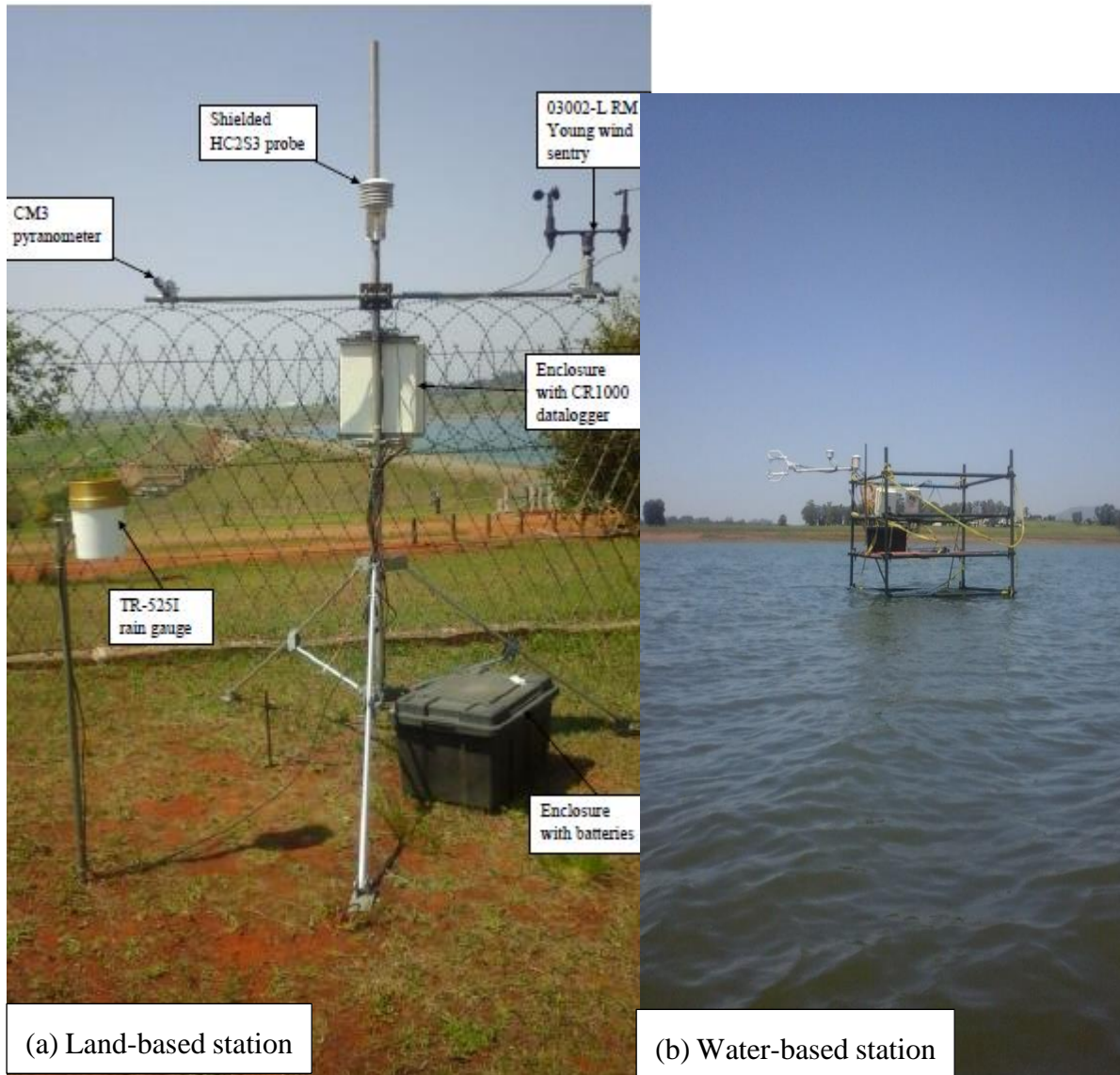


Figure 3.3: Land and water-based stations at Midmar Dam during the study period.

3.6 Data collection and processing

The meteorological data from both land-based and water-based stations were downloaded from the dataloggers after every few weeks and imported into a spreadsheet. The downloaded data underwent data quality control-routine to identify missing data, errors, possible error corrections and suspect data as well as to ensure that data were consistent and met the data quality objectives. Furthermore, data quality control was important not only in obtaining accurate data but also for monitoring the operation of the observing system. When an abnormal observation was reported, the cause was identified and any maintenance, calibration of both faulty sensor and datalogger program were carried out. Only land and water data that passed the quality control tests were used for data analysis. The measured water-based data at

timestamp of 30-min were averaged to match the daily resolution of the radiative fluxes estimated using the daily DPMETHS model. To obtain complete data sets for modelling purposes, the missing, faulty and suspect data on the land-based weather station at Midmar Dam were filled by the observations available from the nearby weather stations monitored by Agricultural Research Council (Cedara and Everdon). The location of the different stations where data used in this study were obtained is described in Table 3.3. Furthermore, the daily water depth and surface area data of Midmar Dam which are input to the DPMETHS model were acquired from Umgeni Water.

Table 3.3: Location of the different stations used in the study

Station name	Latitude (S)	Longitude (E)	Elevation (m)
Land-based	29°29'35.76"	30°11'52.80"	1045
Water-based	29°30'53.66"	30°10'50.72"	1045
Everdon	29°27'19.90"	30°16'25.80"	1077
Cedara	29°32'30.80"	30°15'53.90"	1068

3.7 Data analysis

Both land-based and water-based measured meteorological data from 24 February to 4 April 2016 i.e. day of year (DOY) 54 to 94 were used for analysis and modelling purposes at Midmar Dam. Good quality meteorological daily data obtained from the land-based station as well as the surface area and water depth of the dam data were used as input to the DPMETHS model to estimate daily R_n and G . Model estimates of R_n and G were compared to the measurements of R_n and G for the above water surface. The model simulations were compared against the measured estimates by using simple linear regression and other statistics given Page *et al.* (1979). For the error analysis, the following statistics were used:

$$RMSE = \sqrt{\frac{\sum_{i=1}^n (R_{ne} - R_n)^2}{n}} \quad (3.1)$$

$$MBE = \frac{\sum_{i=1}^n (R_{ne} - R_n)}{n} \quad (3.2)$$

where $RMSE$ and MBE are the root mean square error, and mean bias error, respectively. R_{ne} is the modelled net irradiance, R_n is the measured net irradiance, n is the number of observations.

A term by term comparison of the actual difference between R_{ne} and R_n for the short-term performance of the DPMETHS model was conducted using $RMSE$ while for long-term performance, MBE was used. To justify whether the difference between R_{ne} and R_n was significant or not, the student t-test was used. Walpole and Myers (1989) showed that t-value can be calculated from the $RMSE$ and MBE errors, as:

$$t = \sqrt{\frac{(n - 1)MBE^2}{RMSE^2 - MBE^2}} \quad (3.3)$$

3.8 Landsat-8 surface water temperatures data collection and processing

Images acquired during the study period were downloaded from the website of the United States Geological Survey (USGS) (<http://glovis.usgs.gov/>). Two Landsat-8 images covering Midmar Dam were collected during the study period (i.e. acquired on the 25th February and 12th March). However, only the image acquired on the 25th February had cloud cover less than 60% and was used in this study. At-sensor thermal infrared sensor (TIRS) provides data measured at a wavelength region are generally stored in Digital Numbers (DNs) at spatial resolution of 100 m. The TIRS provide two thermal bands (band 10 and 11). However, only thermal band 10 was used to compute SWT in this study. The choice of this band was based on its greater range of wavelength and it's not being saturated as also noted by Lamaro *et al.* (2013). The Ilwis 3.8 free software was used to write script which was used to convert TIRS data into surface water temperatures. The script used utilized the following procedure as recommended by the USG (2013):

The radiance rescaling factors provided in the metadata file were used convert the DN values to TOA spectral radiance using:

$$L_\lambda = M_L Q_{cal} + A_L \quad (3.4)$$

where L_λ is the TOA spectral radiance (Watts/ (m² srad μm)), M_L is the Band-specific multiplicative rescaling factor from the metadata (RADIANCE_MULT_BAND_x, where x is

the band number), Q_{cal} is the quantized and calibrated standard product pixel values (DN), A_L is the band-specific additive rescaling factor from the metadata (RADIANCE_ADD_BAND_x).

The TOA spectral radiances were then converted to brightness temperatures using the thermal constants provided in the metadata file:

$$T = \frac{K_2}{\ln\left(\frac{K_1}{L_\lambda} + 1\right)} \quad (3.5)$$

where T is the at-satellite brightness temperature (K), K_1 is the Band-specific thermal conversion constant from the metadata (K1_CONSTANT_BAND_x) and K_2 is the Band-specific thermal conversion constant from the metadata (K2_CONSTANT_BAND_x).

The at-satellite brightness temperatures were used to compute surface water temperatures using:

$$SWT = \frac{T}{(1 + w) \times \left(\frac{T}{p}\right) \times \ln(\varepsilon)} \quad (3.6)$$

where SWT is surface water temperature (K), w is the RADIANCE_MULT_BAND at 11.5 μm , p is the Plack's constant (6.626×10^{-34} J s) and ε is 0.97 corresponds to the infrared emissivity of water.

Water-surface temperature values estimated for the image were extracted by interpolating the location of the sampling sites using ArcGIS 10.3 software. Finally, temperatures in Kelvin were converted into $^{\circ}\text{C}$ by subtracting 273.15 from the Kelvin using a raster calculator in ArcGIS.

3.9 Acquisition of the ocean data

The hourly solar irradiance, incoming infrared irradiance, air temperature, sea surface temperature, relative humidity, wind speed and direction, rain fall and barometric pressure data of the ocean were acquired from Station 32ST0 (Stratus), owned and maintained by Woods Hole Oceanographic Institution (http://www.ndbc.noaa.gov/station_page.php?station=32ST0). The detailed information about the Stratus station and the measurement descriptions can be found at: <http://www.ndbc.noaa.gov/measdes.shtml>. The data acquired between 10th September and 24th October 2016 were used for the modelling purposes and the choice of these data was based on long record of quality data available from the ocean station.

3.10 Acquisition of the long-term historical data at Cedara station

The daily R_s , T_{air} , RH , U and sunshine duration as well as rainfall data were acquired from Cedara station, owned and maintained by Agricultural Research Council. The meteorological data from 1 January 1966 to 31 December 2015 (50 years) were used to investigate the potential impacts of climate change on the radiation balance of Midmar Dam. The choice of these data was based on long-term records of data available at the nearest weather station at Midmar Dam. The missing data were patched using the procedure provided by Savage *et al.* (2016). Furthermore, the history daily water depth and surface area data of Midmar Dam which are input to the DPMETHS model were acquired from Department of Water and Sanitation.

CHAPTER 4 : RESULTS AND DISCUSSION

4.1 Introduction

This Chapter contains results and discussion of results as listed in the aims and objectives section (Section 1.3 and 1.4, respectively). The results of the calibration of the four-component CNR4 net radiometer at the AIM system of Savage *et al* (2014) are discussed at Section 4.2. The discussion in Section 4.2, is on the comparisons between the radiation balance components from the four-component net radiometers (i.e. CNR4 and CNR1) at the AIM system. The climatic conditions overview during the data collection at Midmar Dam is discussed in Section 4.3. The results and findings for the radiation balance of the open water surface at Midmar Dam are discussed in Section 4.4. The discussion in Section 4.4.1, is on the factors that control the temporal variability of the radiation balance of the open water surface. The discussion in Section 4.4.1.1 is on the impacts of clouds cover on the radiation balance of the open water. The discussion in Section 4.4.1.2, is on the temporal variability of reflection coefficient of water (r) and its role on the radiation balance of the open water. Section 4.4.1.3, discusses the temporal variability of air temperature (T_{air}) and surface water temperature (SWT) and their effects on the radiation balance of open water surface. The discussion in Section 4.4.2, is on the impacts of the spatial variability of SWT on the spatial variability of the radiation balance of open water surface at Midmar Dam. The results and findings for the temporal variability of the above-water available energy flux are discussed in Section 4.5. The discussion in Section 4.6, is on the modelling of the radiative fluxes above water at Midmar Dam using a daily time-step DPMETHS model that utilizes the land-based measurements as model inputs. The results and findings for the comparisons between meteorological measurements made over water and land-based measurements are discussed in Section 4.6.1. The discussion in Section 4.6.2, is on the comparisons between the measured and the modelled daily radiative fluxes above water at Midmar Dam. The discussion in Section 4.7, is on the modelling of the radiative fluxes for an eastern Pacific Ocean at different climatic conditions using a daily time-step DPMETHS model. The discussion in Section 4.8, is on the potential impacts of climate change on the radiation balance of Midmar Dam using the long-term radiative daily data generated using the Cedara data as an inputs to the DPMETHS model.

4.2 Calibration of the CNR4 net radiometer

As part of the four-component CNR4 net radiometer calibration, radiative fluxes acquired from the water-based station at the AIM system were compared against the radiative fluxes from the four-component CNR1 net radiometer also at the AIM system for the same period. Radiation data between 27th and 29th July 2015 i.e. day of year (DOY) 207 to 209 were used for comparison and the choice of these data sets was based on quality of data available from both four-component net radiometers under clear-sky conditions (Kipp and Zonen, 2014).

4.2.1 Solar irradiance

The comparisons between the solar irradiances R_{S_CNR4} and R_{S_CNR1} indicated a good agreement with both following the same diurnal variability, positive during daytime and zero during night-time (Figure 4.1). The regression graph of R_{S_CNR4} and R_{S_CNR1} indicated that about 99 % variation in R_{S_CNR4} can be explained by the R_{S_CNR1} (Figure 4.2). The observed strong linear relationship between these data sets indicated the correct functioning of the ‘up facing’ pyranometer in the four-component CNR4 net radiometer.

4.2.2 Reflected solar irradiance

The comparisons between the reflected solar irradiances rR_{S_CNR4} and rR_{S_CNR1} indicated a good agreement with both closely following the same diurnal variability, positive during daytime and zero during night-time (Figure 4.3). The regression graph of rR_{S_CNR4} and rR_{S_CNR1} indicated that about 99 % variation in rR_{S_CNR4} can be explained by the rR_{S_CNR1} (Figure 4.4). The observed strong linear relationship between these data sets indicated the correct functioning of the ‘down facing’ pyranometer of the four-component CNR4 net radiometer.

4.2.3 Incoming infrared irradiance

The comparisons between the incoming infrared irradiances L_{d_CNR4} and L_{d_CNR1} indicated reasonable agreement with both following the same diurnal variability although the peaks of L_{d_CNR1} were greater than L_{d_CNR4} (Figure 4.5). However, these observations indicated the correct functioning of the ‘up facing’ pyrgeometer of the four-component CNR4 net radiometer.

4.2.4 Outgoing infrared irradiance

The comparisons between the outgoing infrared irradiances L_{u_CNR4} and L_{u_CNR1} indicated a reasonable agreement with both following the same diurnal variability although the fluxes of L_{u_CNR1} were greater than fluxes of L_{u_CNR4} (Figure 4.6). However, these observations indicated the correct functioning of the ‘down facing’ pyrgometer of the four-component CNR4 net radiometer.

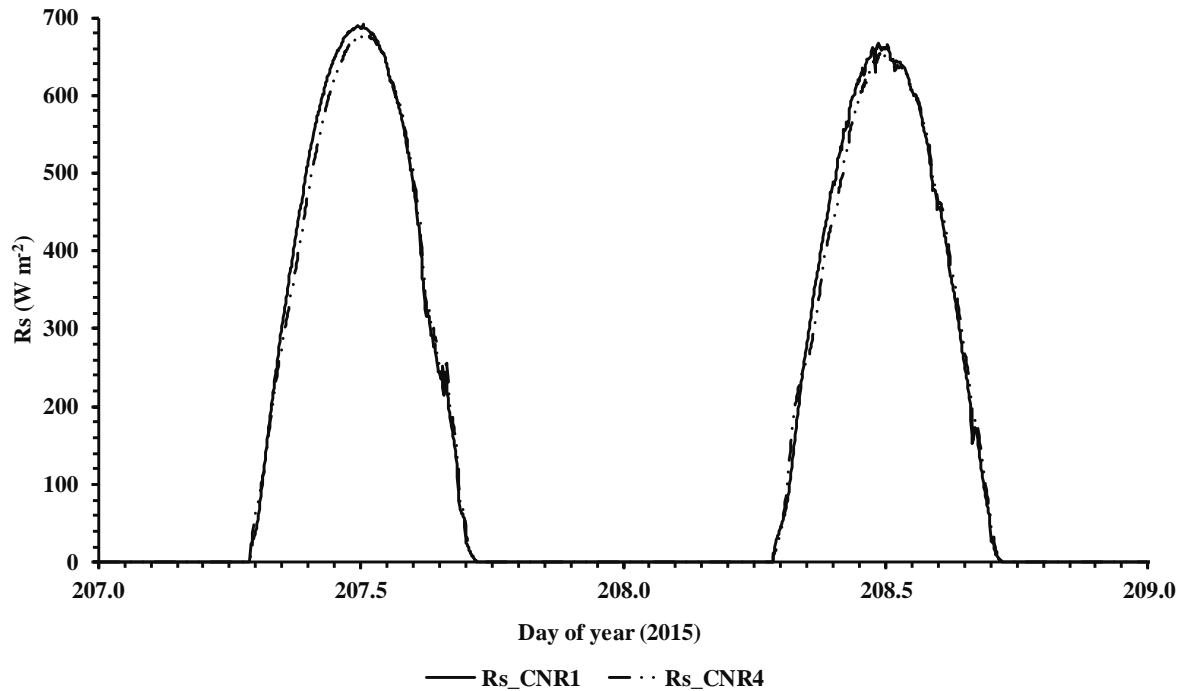


Figure 4.1: Comparisons between R_{s_CNR4} and R_{s_CNR1} for a two-day period (27th and 29th July 2015) at the AIM site.

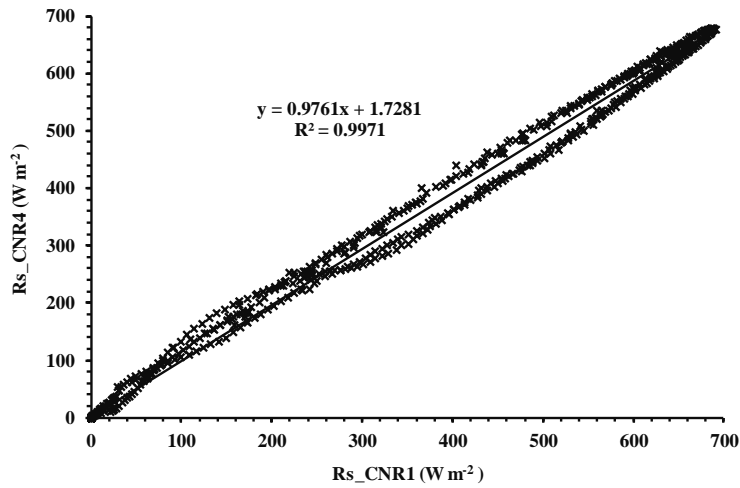


Figure 4.2: Regression plot of R_{s_CNR4} vs R_{s_CNR1} for a two-day period (27th and 29th July 2015) at the AIM site.

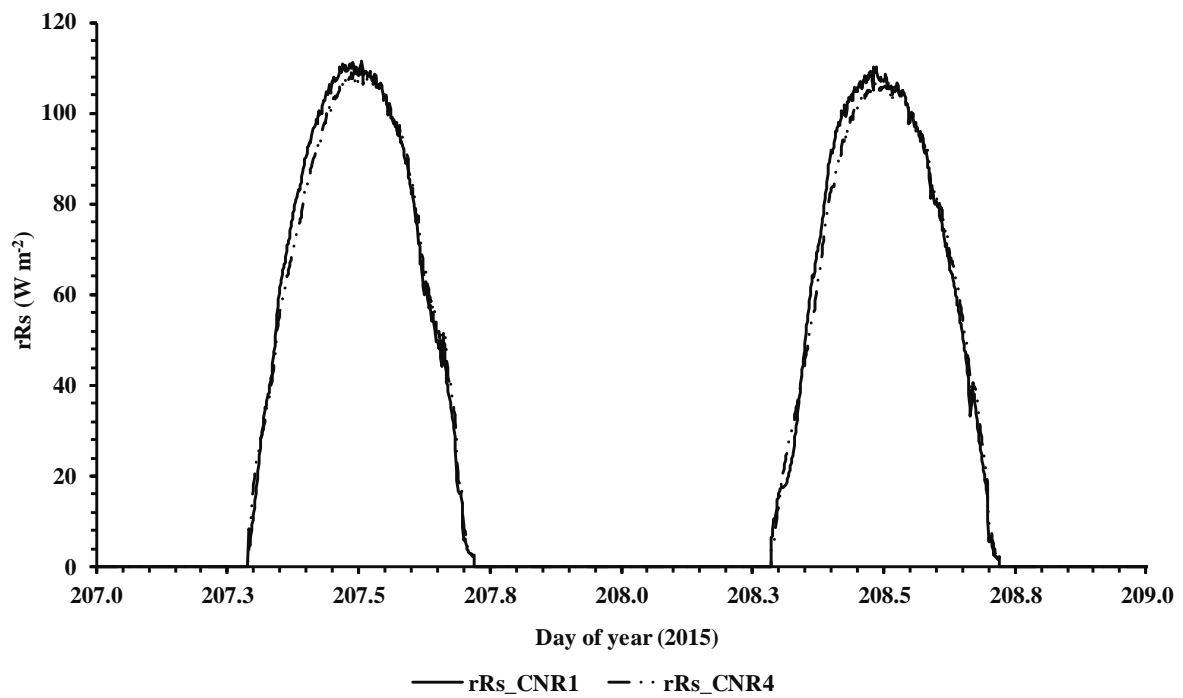


Figure 4.3: Comparisons between rR_{s_CNR4} and rR_{s_CNR1} for a two-day period (27th and 29th July 2015) at the AIM site.

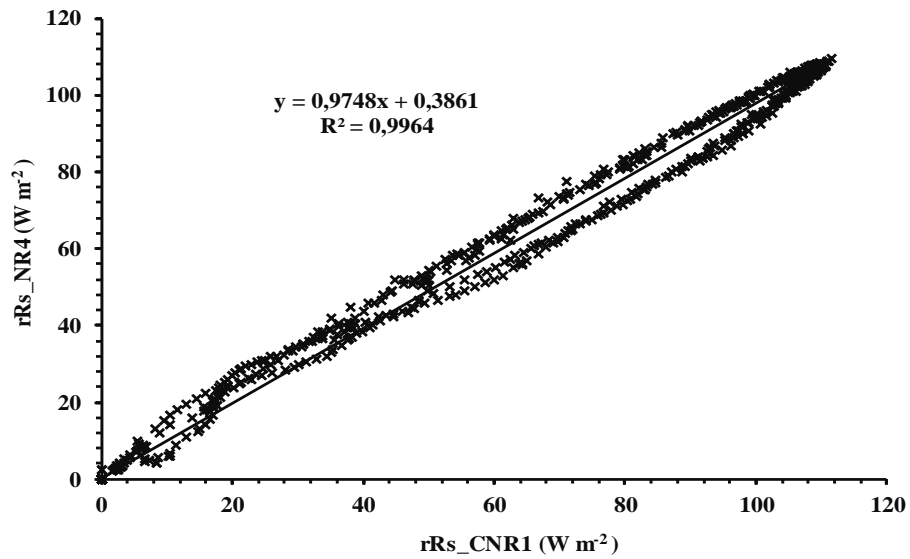


Figure 4.4: Regression plot of rR_{s_CNR4} vs rR_{s_CNR1} for a two-day period (27th and 29th July 2015) at the AIM site.

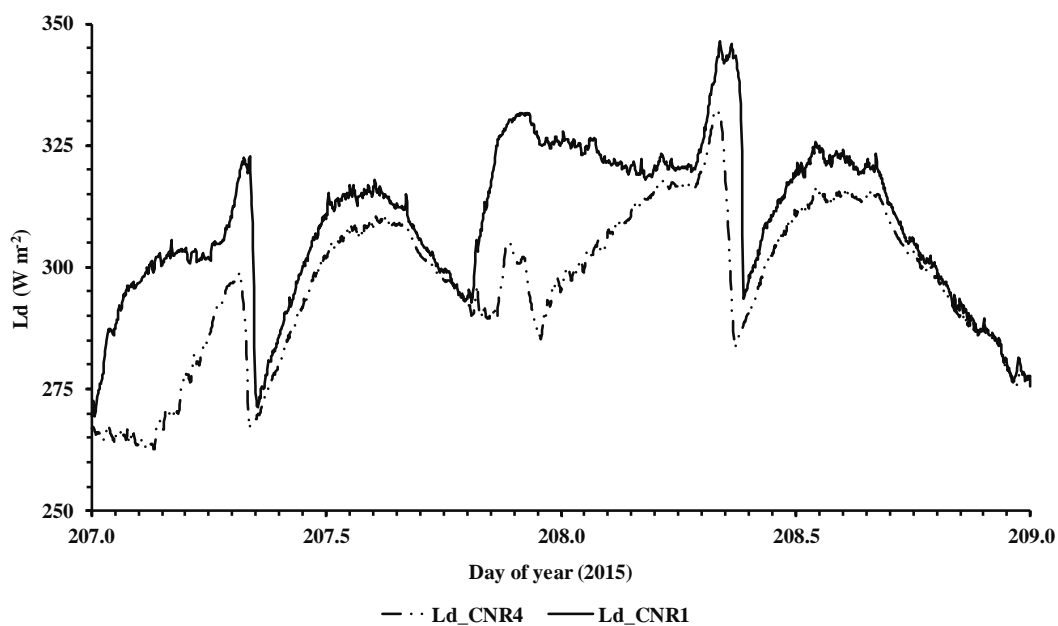


Figure 4.5: Comparisons between L_{d_CNR4} and L_{d_CNR1} for a two-day period (27th and 29th July 2015) at the AIM site.

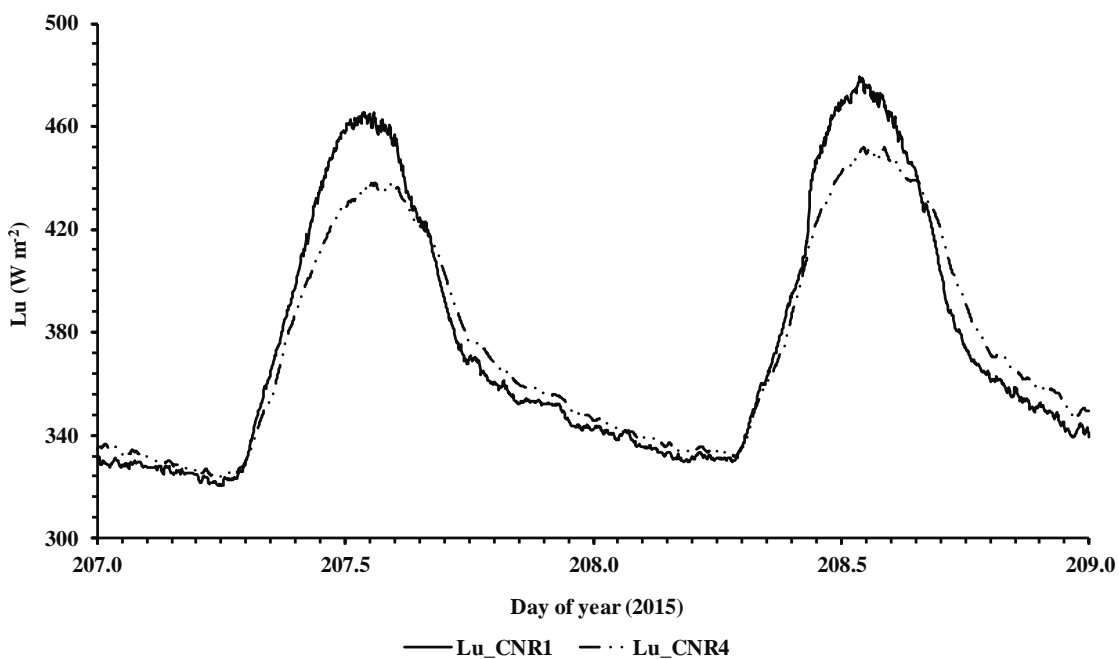


Figure 4.6: Comparisons between L_{u_CNR4} and L_{u_CNR1} for a two-day period (27th and 29th July 2015) at the AIM site.

4.2.5 Net irradiance

The two-day comparison period between R_n data obtained from the four-component CNR4 net radiometer (R_{n_CNR4}) and R_n data obtained from the four-component CNR1 net radiometer (R_{n_CNR1}) indicated that R_{n_CNR4} and R_{n_CNR1} followed the same diurnal variability, R_n being positive during daytime and negative during night-time (Figure 4.7). However, R_{n_CNR1} was greater than R_{n_CNR4} during night-time. The regression graph of R_{n_CNR4} and R_{n_CNR1} indicated that about 99 % variation in R_{n_CNR4} can be explained by the R_{n_CNR1} (Figure 4.8). The observed strong linear relationship between these data sets indicated the correct functioning of the data logger program used to compute R_n from the measured radiation balance components using four-component CNR4 net radiometer.

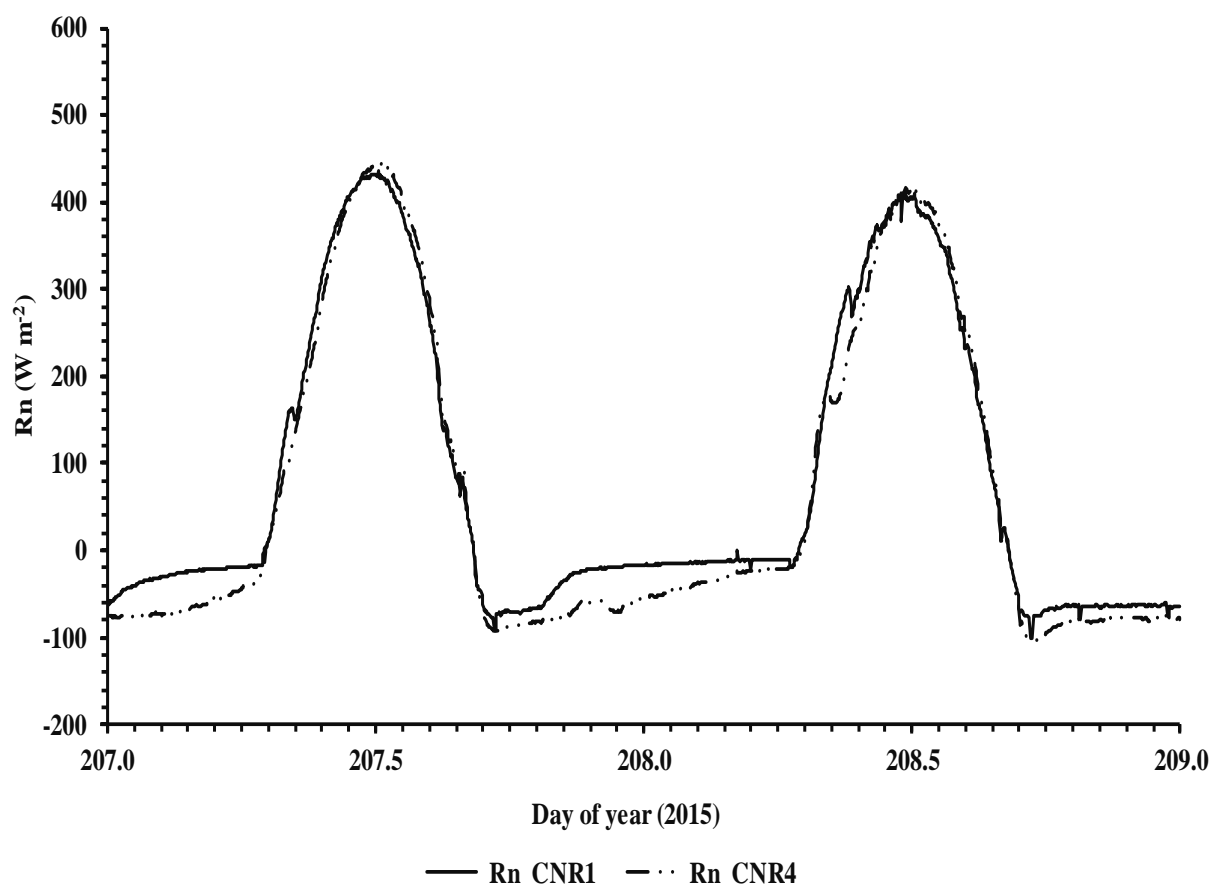


Figure 4.7: Comparisons between R_{n_CNR4} and R_{n_CNR1} for a two-day period (27th and 29th July 2015) at the AIM site.

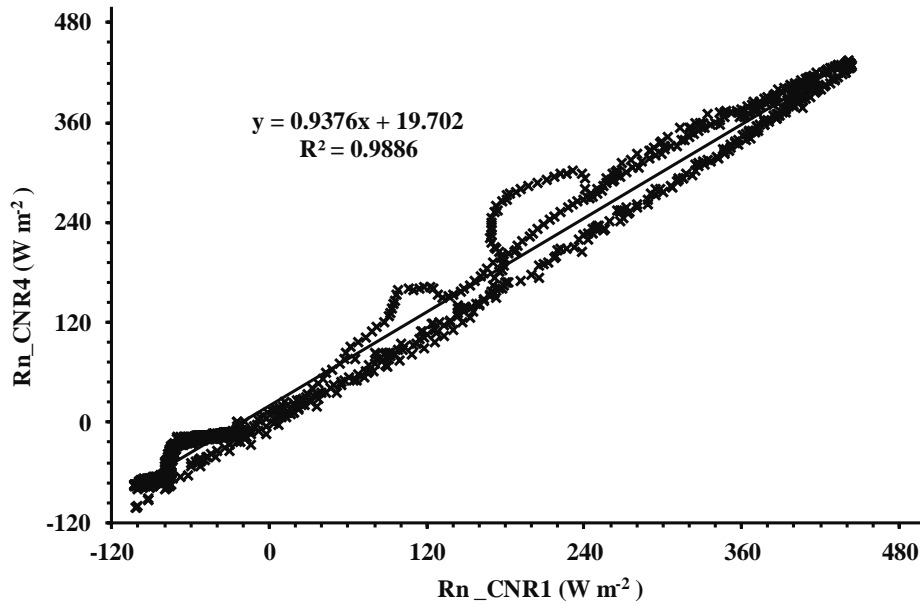


Figure 4.8: The regression plot of R_{n_CNR4} vs R_{n_CNR1} for a two-day period (27th and 29th July 2015) at the AIM site.

4.2.6 General comments

There were differences between radiation balance components from the four-component net radiometers due to the difference in levelling of these four-component net radiometers since the CNR4 net radiometer was mounted at 1.5 m above the surface while the CNR1 net radiometer was mounted at 3 m above the surface. However, good relationships were observed between these data sets which indicated that the components of the CNR4 net radiometer were functioning properly.

4.3 Climatic conditions during study period at Midmar Dam

The land-based microclimate measurements reported were acquired at Midmar Dam between from 24 February to 4 April 2016 i.e. DOY 54 to 94, inclusively. Daily-average T_{air} ranged between 14.5 and 24.9 °C on DOY 82 and 66, respectively. Minimum T_{air} recorded were as low as 10.3 °C (DOY 88) with maxima as high as 34.8 °C (DOY 67) illustrated the wide range of temperature conditions experienced during the measurement period. A rainfall total of 108.6 mm was measured over the entire measurement period (DOY 54 - 94). Daily R_s recorded were as low as 2.18 MJ m⁻² (DOY 67) with maxima as high as 26.76 MJ m⁻² (DOY 60) illustrated

the wide range of R_s experienced during the measurement period. Minimum RH as low as 13.1 % (DOY 90) with maxima as high as 100 % (on most of the days) illustrated the wide range of humidity conditions experienced during the experiment. Daily-average U were generally low and ranged between 0.26 and 1.71 m s⁻¹, but maximum U as high as 10.70 m s⁻¹ (DOY 57) were recorded. Prevailing winds were from the southeast, east and south which correspond to water to land wind flows at the water-based station as also noted by Mengistu and savage (2010).

4.4 Radiation balance of the water surface at Midmar Dam

Radiation balance of water is the balance between the net solar radiation and net infrared radiation at water surface. Measurements or estimates of R_n are required for accurate modelling of open water evaporation. However, R_n over water is measured with difficulty since it is the sum of four distinct variables. Furthermore, R_n is measured by net radiometers which are expensive, requiring continuous calibration and maintenance to ensure accurate estimates of R_n . Consequently, R_n is often estimated using the models that utilize meteorological data that are readily available in most standard weather stations. However, for accurate modelling of R_n over water surface, it is vital to understand the factors enhancing temporal and spatial variability of the radiation balance of water storage.

4.4.1 Factors enhancing temporal variability of the radiation balance over water surface

4.4.1.1 Cloud cover

To evaluate the effect of cloudiness on the radiation balance of the water surface at Midmar Dam, the radiation balance under clear-sky day (DOY 60) was compared with the radiation balance under overcast day (DOY 67), as shown in Figure 4.9. The R_n fluxes were minimal (ranged between -33 to 111 W m⁻²) for the overcast day compared to a clear-sky day (ranged between -92 to 860 W m⁻²). However, during both overcast and clear-sky days the R_n fluxes followed the same diurnal variability as the R_s fluxes although R_s fluxes were always greater than R_n fluxes. The R_s fluxes were minimal (130 W m⁻²) for the overcast day while maximum (1015 W m⁻²) for the clear-sky day. The maximum R_s fluxes were observed during mid-day (local time 12h30). The minimal R_s fluxes during overcast day are attributed to R_s being

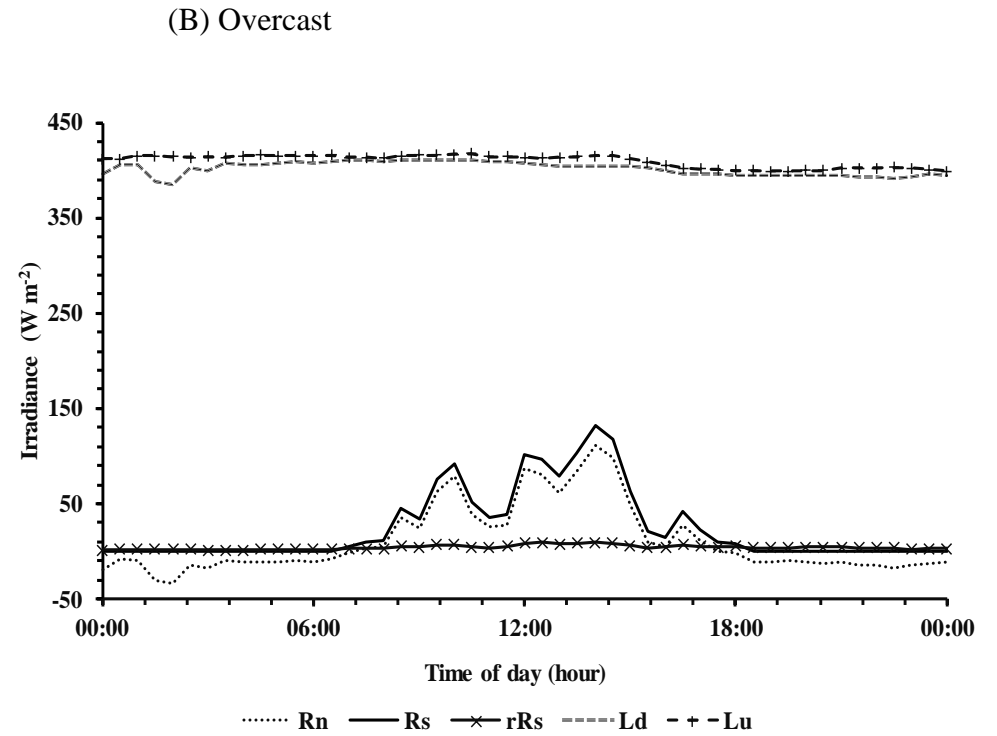
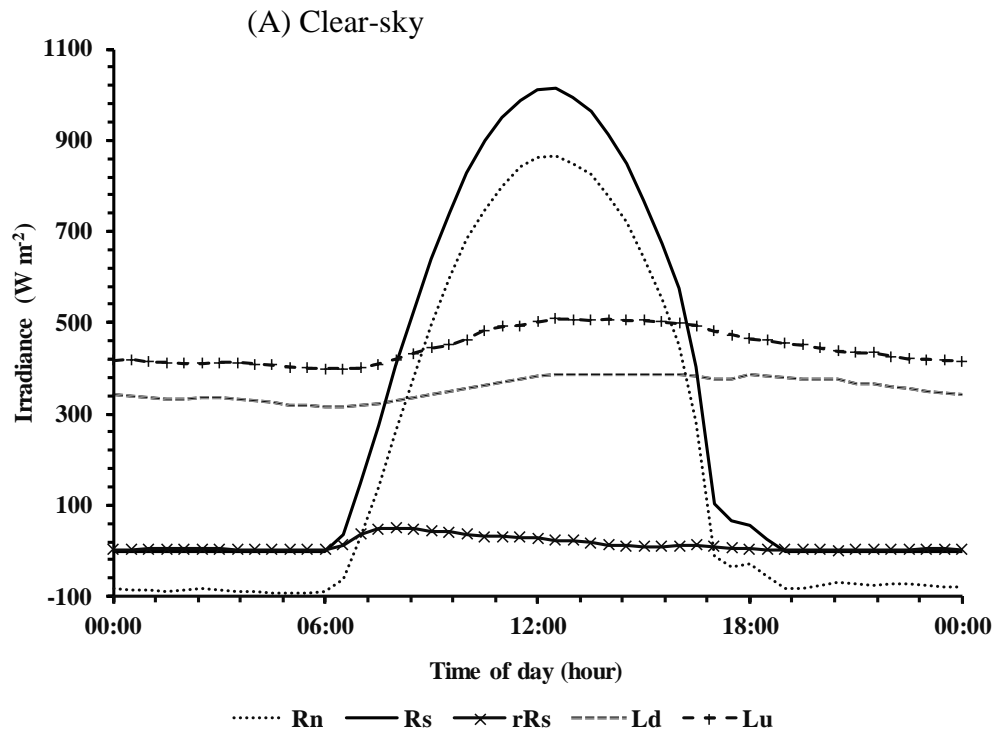


Figure 4.9 : Radiative fluxes above open water at Midmar Dam for clear-sky (3th March 2016) and overcast conditions (8th March 2016).

scattered and reflected or absorbed by clouds, also noted by Finch and Hall (2001). The rR_s fluxes followed the same diurnal variability as the R_s during both clear-sky and overcast days. However, rR_s fluxes showed minimal diurnal variability compared to R_s during both clear-sky and overcast days. During the overcast day, R_n fluxes were always (day and night) dominated by L_u and L_d , respectively while during the clear-sky day, R_n fluxes were dominated by R_s during the daytime and dominated by L_u and L_d , respectively during the night-time. However, during both overcast and clear-sky days the R_n fluxes were always directed towards the water surface during day, while at night the R_n fluxes were much weaker and directed away from the water surface and these observations were consistent with results reported by Mahmud *et al.* (2015). These observations were more pronounced under clear-sky day than overcast day. The night-time radiative cooling (negative R_n fluxes) is attributed to a much greater L_u than L_d during night-time where R_s was zero, as also noted by Arya (2001). During clear-sky day, L_u was much greater than L_d while during overcast day the difference between L_u and L_d was minimal indicated that greater L_d was emitted during the overcast day compared to the clear-sky day. Cloud cover had no effect on L_u since with constant emissivity, L_u depends on surface water temperature alone.

4.4.1.2 Reflection coefficient of water

4.4.1.2 (a) Variability of reflection coefficient of water

The reflection coefficient of water (r) directly determines the amount of R_s absorbed by the water surface. The diurnal variability of r indicated that r was higher just after the sunrise (local time 06h30) and decrease to minimal during late mid-day (local time 14h30) and then start to increase to its maximum during the sunset (local time 17h30) for water at Midmar Dam for the 29th March 2016 (cloudless) is presented in Figure 4.10. The observed diurnal variability of r indicated that high r were observed during lower sun's angles (during sunrise and sunset) and lower r were observed during the daytime when the sun was perpendicular to the water surface. These observations were consistent to the results reported by Finch and Hall (2001) who noted that at lower sun's angles, there is high water reflectivity.

Measurements of r at 30-minute timestamp were used to calculate the daily-average r . The temporal variability of the daily r for the entire study period indicated that r ranged between 0.05 and 0.14 (Figure 4.11). The maximum daily r values were observed during the days with

high rainfall, for example DOY 67, 68 and 93 with rainfall of 46, 18, and 7 mm, respectively. The thunderstorms resulted on the presence of suspended particulate matter which may increase r . A turbid water body reflected more R_s , as consequence measured R_n fluxes were low during

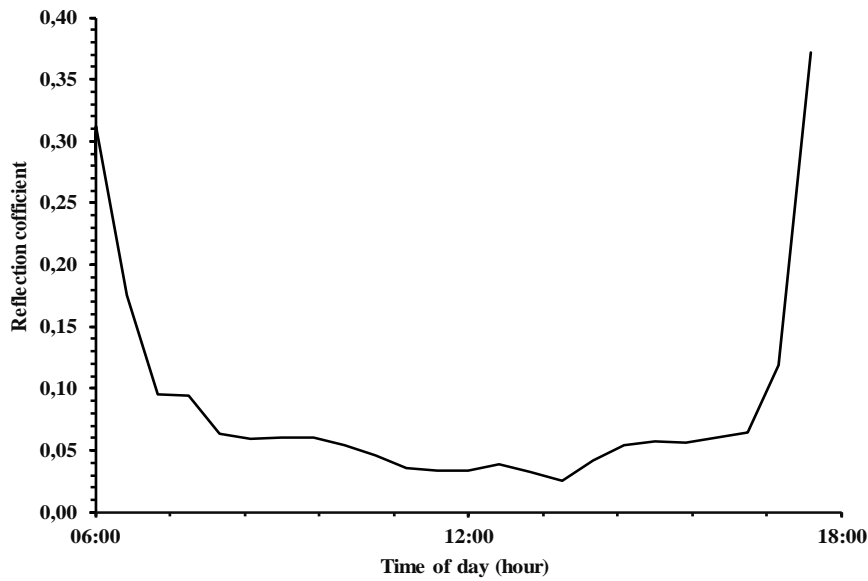


Figure 4.10: The diurnal variability of reflection coefficient of water at Midmar Dam for the 29th March 2016 (cloudless).

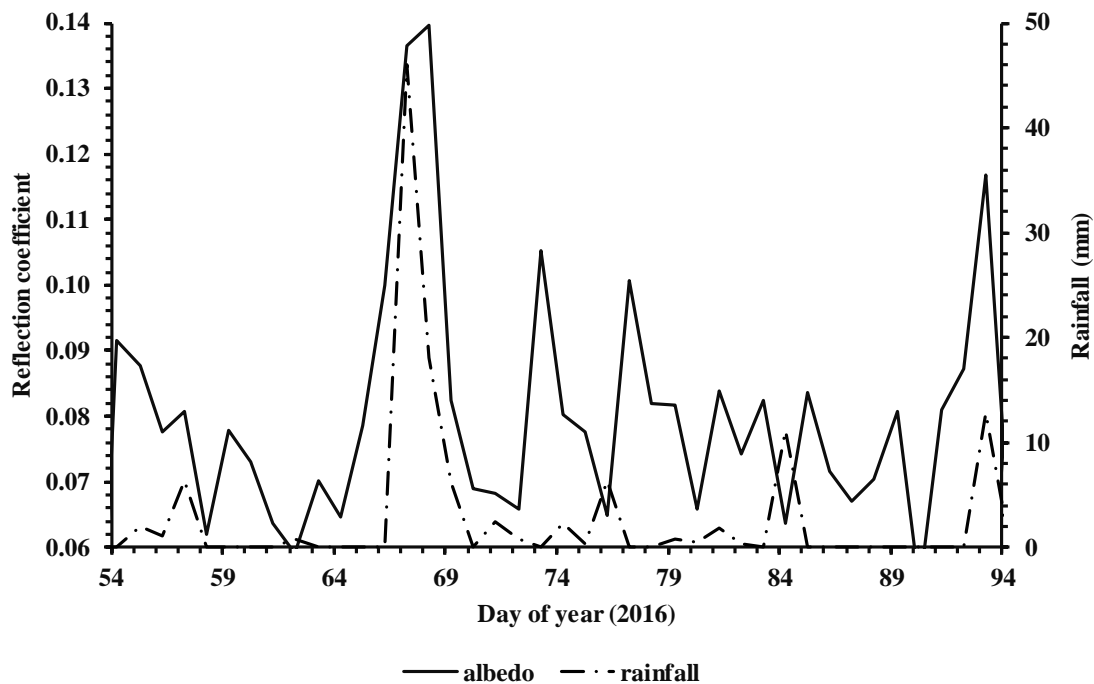


Figure 4.11: The temporal graph showing the daily reflection coefficient of water measured at Midmar Dam from 24th February to 4th April 2016.

the day just after heavy rain as also noted by Finch and Hall (2001). Furthermore, the greater cloud cover during rainy days could have increased the r values as also noted by Timofeyev and Vasil'ev (2008). However, a daily-average of 0.08 was observed during the entire study period which is in consistent with the r used in the DPMETHS model.

4.4.1.2 (b) Effects of reflection coefficient on radiation balance over water surface

To evaluate the effect of r on the radiation balance over water surface, a constant r of 0.08 was used to calculate rR_s from measurements of R_s above water surface. The comparison between the calculated daily rR_s and observed daily rR_s indicated that for high values of rR_s ($> 1.2 \text{ MJ m}^{-2}$), the calculated rR_s fluxes were always greater than the observed rR_s fluxes (Figure 4.12). However, for low values of rR_s ($< 0.4 \text{ MJ m}^{-2}$), the calculated rR_s fluxes were equal to the observed rR_s . For the entire study period, the calculated rR_s fluxes were greater than the observed rR_s fluxes by an average of 0.64 MJ m^{-2} . These observations imply that assuming a constant r of 0.08 during computation of rR_s could result in slight under-simulation of R_n due to over-estimation of rR_s which reduces R_s .

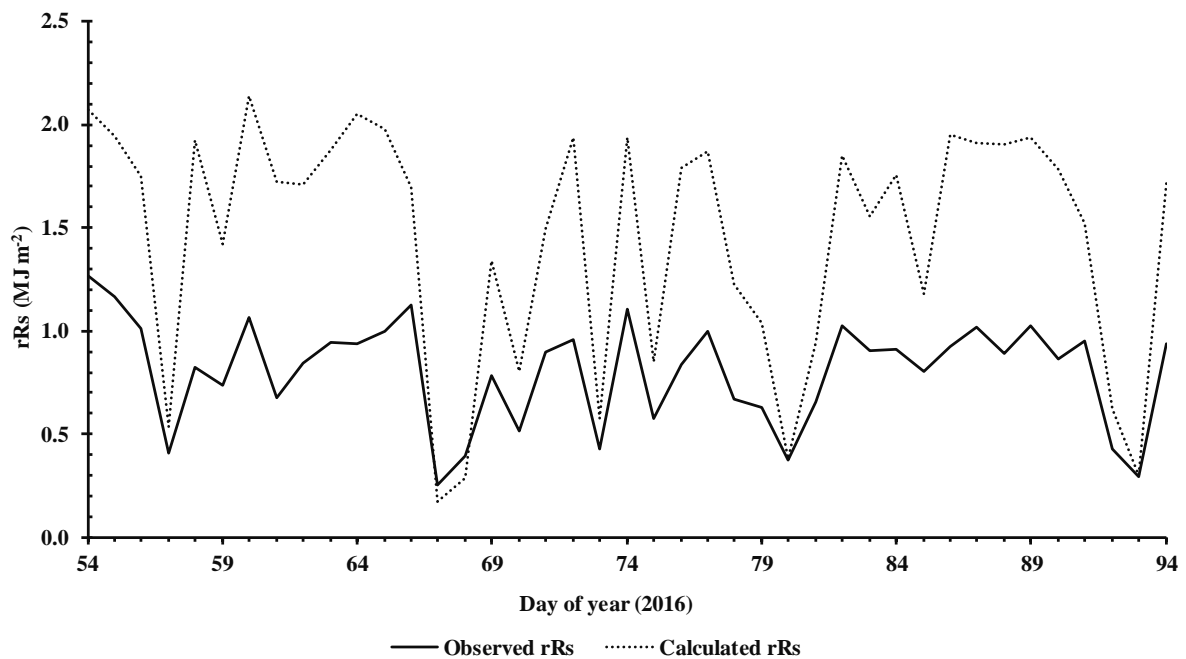


Figure 4.12: The temporal graph showing the calculated daily rR_s and observed daily rR_s above open water at Midmar Dam from 24th February to 4th April 2016.

4.4.1.3 Air and surface water temperature

To evaluate the effect of T_{air} and SWT on the radiation balance over water surface at Midmar Dam, the variability of both T_{air} and SWT (an average of the two infrared thermometers) acquired above open water were investigated since both L_u and L_d are temperature dependent. The diurnal variability of T_{air} and SWT indicated minimal of the both T_{air} and SWT were observed just before the sunrise (local time 06h30) while maximum temperatures were observed during late afternoon (local time 15h30) (Figure 4.13). During the daytime, T_{air} was warmer than SWT while during the night-time the observations were inverted. The observed diurnal variability of SWT indicated that water surface warms up during the daytime while cools during the night-time. These observations are attributed to R_n fluxes being always directed towards the water surface during the day, while at night the R_n fluxes are much weaker and directed away from the water surface as also noted by Mahmud *et al.* (2015).

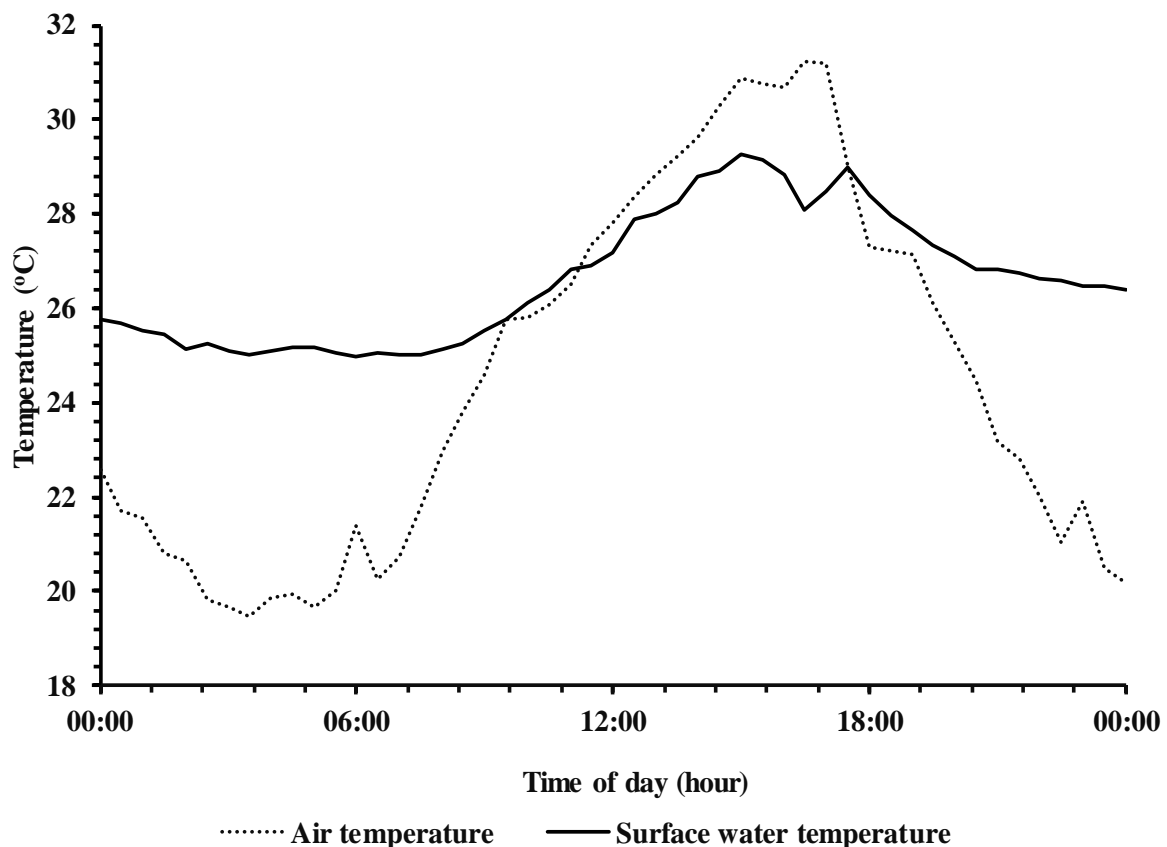


Figure 4.13: The diurnal variation of the air temperature and surface water temperature at Midmar Dam for the 6th March 2016 (cloudless).

For entire study period, the comparison between T_{air} and SWT indicated that the daily-average SWT was always warmer than average T_{air} by 3.7 °C although both T_{air} and SWT showed similar variability (Figure 4.14). However, T_{air} exhibited a wider range (ranged between 11 and 33 °C) than SWT (ranged between 21.5 and 30 °C). These results are consistent with observations reported by Lorenzetti *et al.* (2015). The reduced diurnal range in SWT is attributed to the greater specific heat capacity of water than air. Consequently, water requires a significant amount of energy to change its temperature compared to air. The large heat capacity of water and the absorption of R_s over a large depth combine to reduce the diurnal range of SWT as also noted by Jacobs *et al.* (2008).

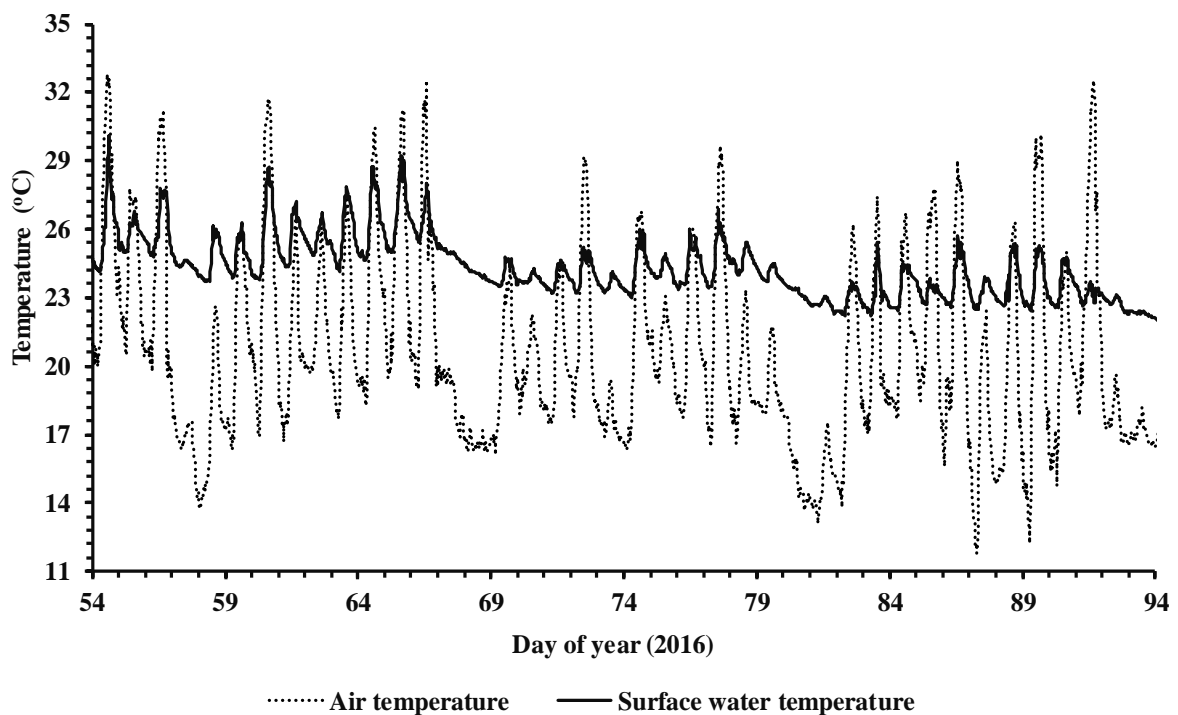


Figure 4.14: Temporal graph showing variability of the daily-average T_{air} and SWT at Midmar Dam from 24th February to 4th April 2016.

4.4.2 Spatial variability of the radiation balance above water at Midmar Dam

The downward components of radiation balance can be assumed to be relatively constant over relatively large surface areas except under partially cloudy skies (Federer, 1968). Therefore, any spatial variation of R_n above open water is mainly due to the spatial variability in SWT since with constant emissivity, L_u depends on SWT alone (Wang *et al.*, 2014). However, conducting water temperature surveys using conventional limnological sampling involves

significant financial investment in instrumentation and extensively field work on a reservoir. The spatial variation of *SWT* across Midmar Dam estimated using Landsat-8 data was used to evaluate the spatial variability of R_n as affected by the variation of L_u which is proportional by the fourth power on *SWT*. There were two Landsat-8 images covering Midmar Dam collected during this study period (i.e. acquired on the 25th February and 12th March). However, only the image acquired on the 25th February had cloud cover less than 60 % and was used in this study. The spatial variability of *SWT* across Midmar Dam indicated that *SWT* ranged between 23.4 and 26.0 °C (Figure 4.15).

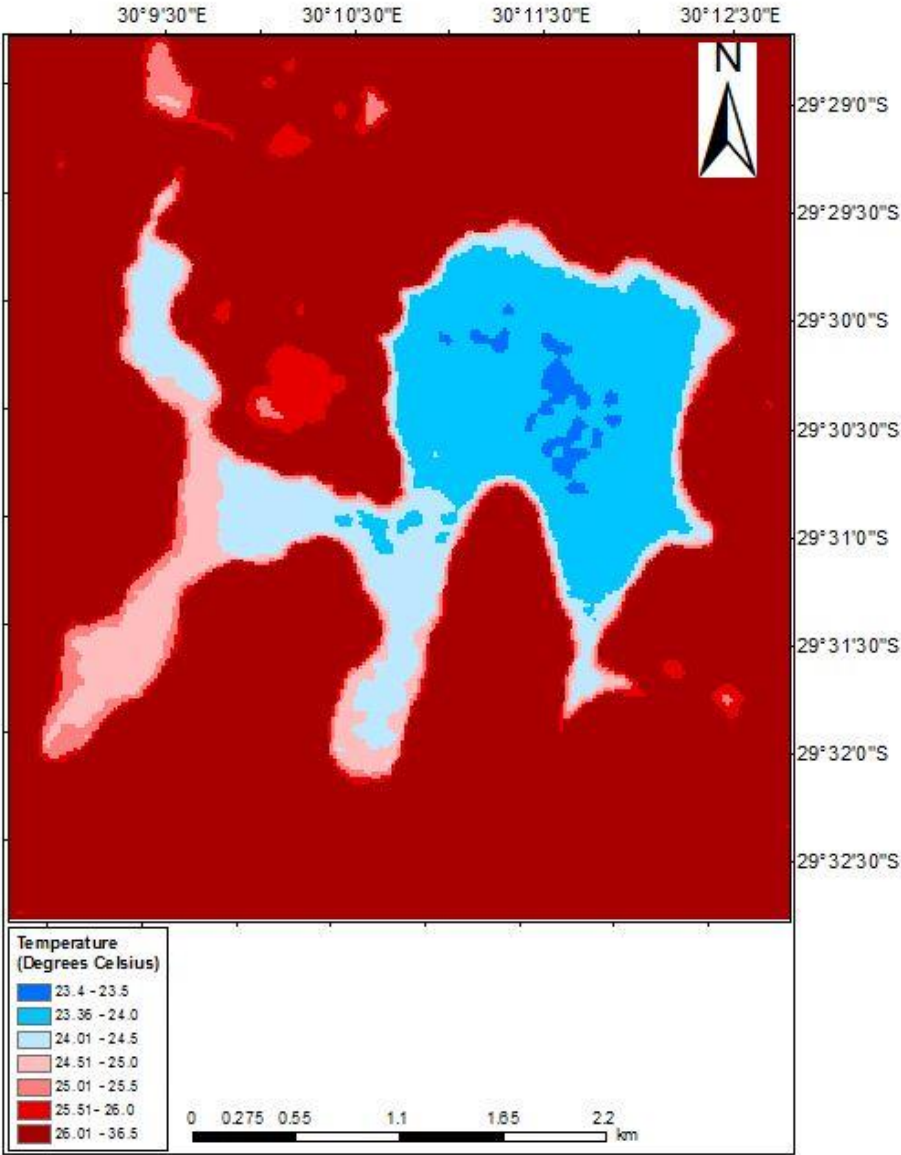


Figure 4.15: The spatial variability of *swt* across Midmar Dam for the 25th February 2016 (cloudless) at 09h50.

Furthermore, the spatial variability of SWT across Midmar Dam also indicated that water near the shore responded to the atmospheric conditions very quickly compared to the offshore water. Consequently, water near the shore was observed to always be warmer than offshore water by an average of $1.5\text{ }^{\circ}\text{C}$. These observations were consistent with the results reported by Alcântara *et al.* (2010). Furthermore, shallow parts of the dam were $2\text{ }^{\circ}\text{C}$ warmer than the deeper part of the dam. Since the north-west was the predominant wind direction during the Landsat-8 overpass time, the south-east water was warmer than north-west by an average of $1.5\text{ }^{\circ}\text{C}$ due to warm-surface water being blown from north-west to south-east by wind. The observed average of 1.5 to $2\text{ }^{\circ}\text{C}$ variability of SWT across Midmar Dam implies the very low spatial variability of L_u which is temperature dependent. Therefore, the low spatial variability of SWT is associated with low spatial variation of R_n across the dam. These observations indicated that point measurements of SWT are reasonable indicators of the reservoir SWT which is used to compute water-storage heat flux and L_u from water surface at Midmar Dam.

4.5 Above-water available energy flux

Above-water available energy flux is the paramount input in energy balance models to estimate open water evaporation and yet is measured directly with greater difficulty because it involves significant financial investment in instrumentation and extensively field work on a reservoir. Consequently, above-water available energy flux is often estimated using the models that utilize meteorological data that are readily available in most standard weather stations. However, for accurate modelling of the above-water available energy flux, it is vital to understand the variability of the above-water available energy flux. To understand the temporal variability of the above-water available energy flux, the two components of the available energy flux (i.e. R_n and water-stored flux) were evaluated.

4.5.1 Water-stored heat flux

The water-stored flux (G) was calculated from the 30-min temporal changes in average water temperatures measured at different depths using Eq. (2.4). The daily estimates of G at different water layers were obtained by summing the 30-min G data for each day (00h30 to 24h00). Then, the daily-average G was calculated from G for the different layers of the water profile.

The time series of 30-min temporal variability of G indicated that G was proportional to the depth of water (Figure 4.16). However, the G at different layers of water showed the same

diurnal variability. The minor difference in G stored between the shallowest water layer (0 to 0.02 m) is attributed to shallow (<5 m depth) water reservoirs being well-mixed with little stratification due to the wind-stirring effect as also noted by Gallego-Elvira *et al.* (2011). A running mean of order 3, corresponding to 1.5 h, was used to obtain half-hourly values of G . Even with using a running mean, estimates of G fluctuated from negative to positive for each 30-min period, due to turbulent water waves of varying temperature travelling past the thermocouples as also noted by Tanny *et al.* (2008), Mengistu and Savage (2010) as well as Savage (2010). However, G was positive during most of the day and negative during most of the night. These observations are consistent with the results reported by Mahmud *et al.* (2015), suggesting that water acted as a sink of heat during the daytime and a source of heat during the night-time. The maximum heat storage was observed just before the sunset (local time 16h00) while the maximum rapid release of stored heat was just after the sunset (local time 18h00).

For the entire study period, the temporal variability of G showed that during some days, heat was stored in water storage ($G > 0 \text{ W m}^{-2}$) while during other days, heat was released from water storage ($G < 0 \text{ W m}^{-2}$) (Figure 4.17). The net heat flux loss in the water storage was observed during days with low daily R_s while net heat flux gain was observed during days with high daily R_s . For example, during the DOY 73 with daily R_s of 7.1 MJ m^{-2} , net heat flux was released from the water storage (-15 MJ m^{-2} was loss between the depth of 0.08 and 0.16 m). However, during the DOY 74 daily R_s of 24.1 MJ m^{-2} , net heat was stored in the water storage (31 MJ m^{-2} was stored between the depth of 0.08 and 0.16 m). These observations indicate that G plays a significant role in the daily energy balance and cannot be neglected for accurate estimation of the daily open water evaporation as also noted by a number of authors (e.g. Finch and Hall (2001), Tanny *et al.* (2008), Jensen (2010), Savage (2010) as well as Mengistu and Savage (2010).)

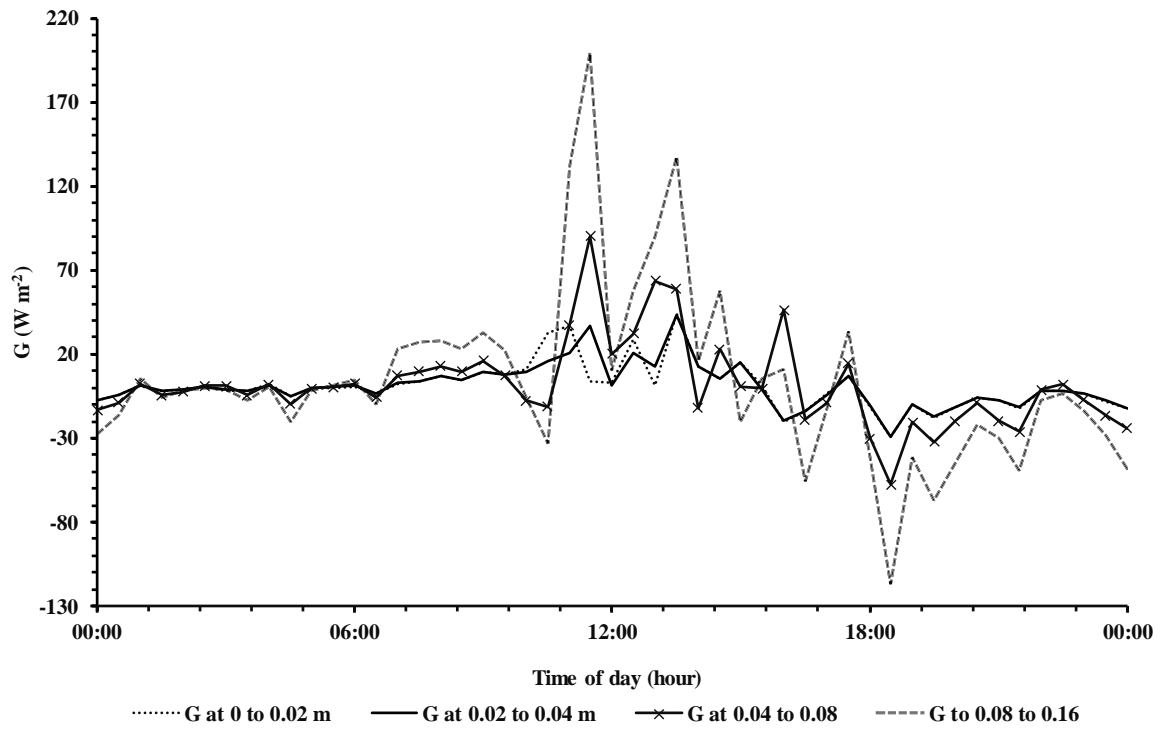


Figure 4.16: The diurnal variability of G measurements at different water depth increments for Midmar Dam for the 1th March 2016 (cloudless).

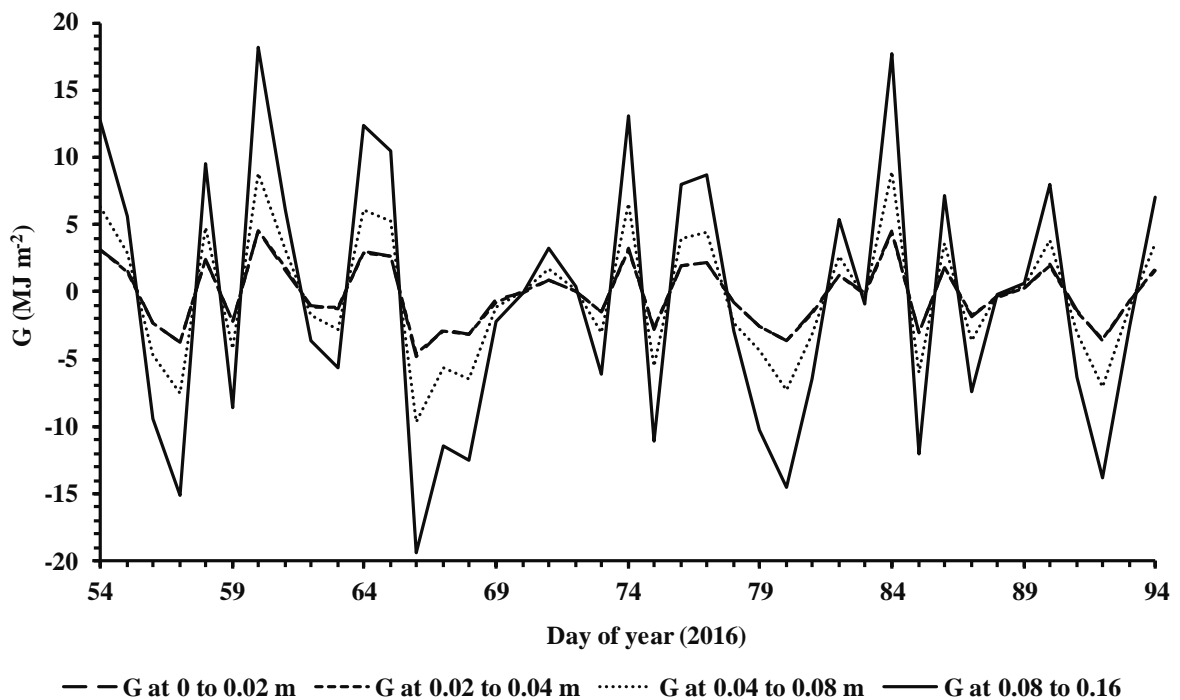


Figure 4.17: Temporal variability of G measurements at different water depth increments for Midmar Dam from 24th February to 4th April 2016.

4.5.2 Variability of the available energy flux components above water

Estimates of G fluxes of the dam showed a very wide variation that was not attributed to variation in R_n and were unreliable. As an example, during DOY 56, the temporal variation in both R_n and G indicated that G showed a similar diurnal variation to R_n with comparable magnitudes and peaked at the same time as the peak in R_n , as also noted by Savage (2010) (Figure 4.18). Maximum of both R_n and G fluxes were observed during the daytime (around 13:30 local standard time) and were negative during night-time. During the daytime, R_n fluxes were positive, corresponding to a source of energy while during night-time, R_n were negative, corresponding to a loss of energy from the water surface as also noted by Alcântara *et al.* (2010).

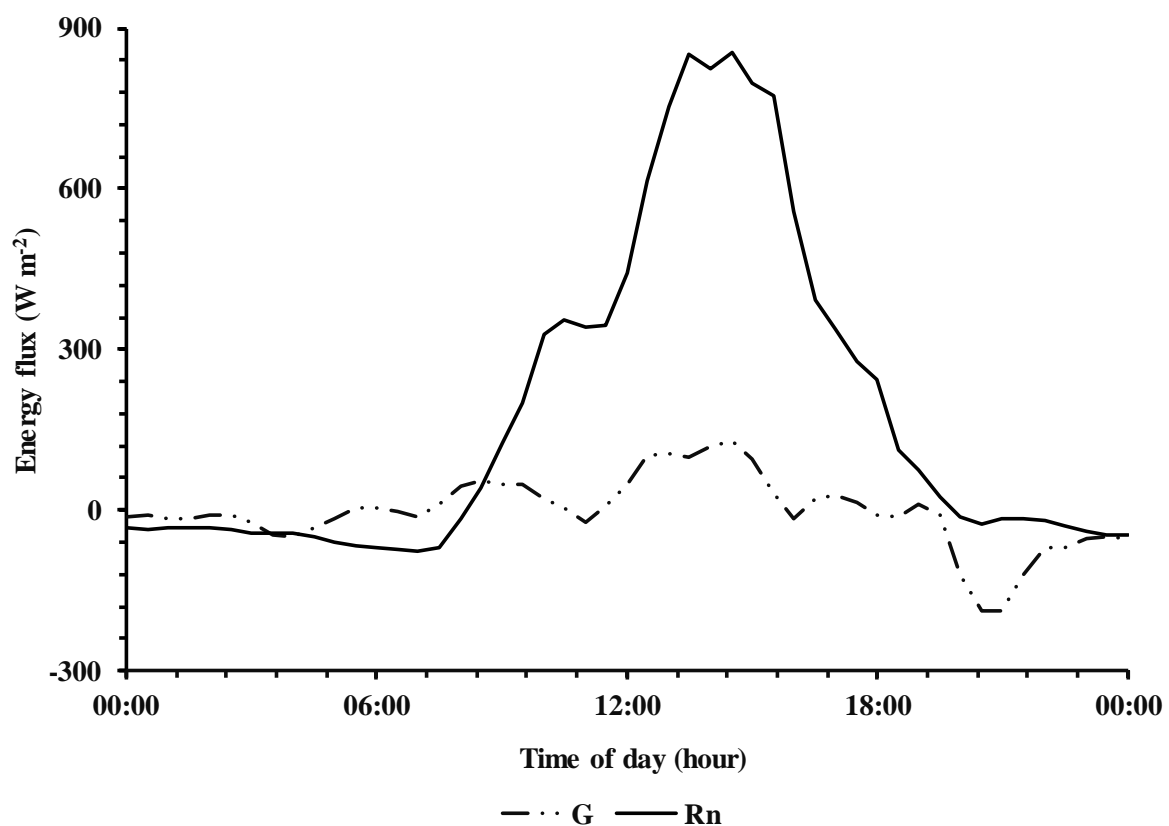


Figure 4.18: The diurnal variation in the measured 30-min fluxes of G and R_n for the 26th February (DOY 56) 2016 (cloudless).

However, during DOY 66, the temporal variation in both R_n and G indicated that G showed a similar diurnal variation to R_n but in the late afternoon (around 14h00 local standard time) a large decrease of G to -71 W m^{-2} compared to R_n of 843 W m^{-2} and immediately there was a sudden and unexplained increase of G to 52 W m^{-2} compared to R_n of 455 W m^{-2} (Figure 4.19).

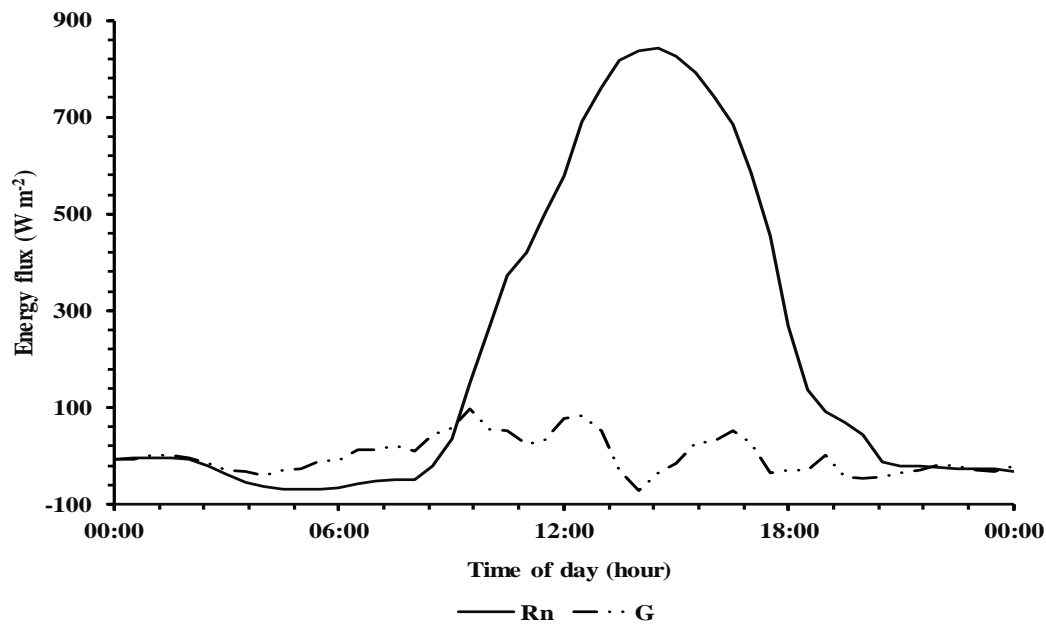


Figure 4.19: The diurnal variation in the measured 30-min fluxes of G and R_n for the 13th March (DOY 66) 2016 (cloudless).

For the entire study period, the comparison between the calculated daily-average G and the measured daily R_n indicated that daily G follow the same variability to daily R_n most of the time during the entire study period (Figure 4.20). The regression graph of the R_n and G indicated that daily G accounted for up to 47 % of the daily R_n (Figure 4.21). These observations are consistent with results reported by Mengistu and Savage (2010) at the same study site.

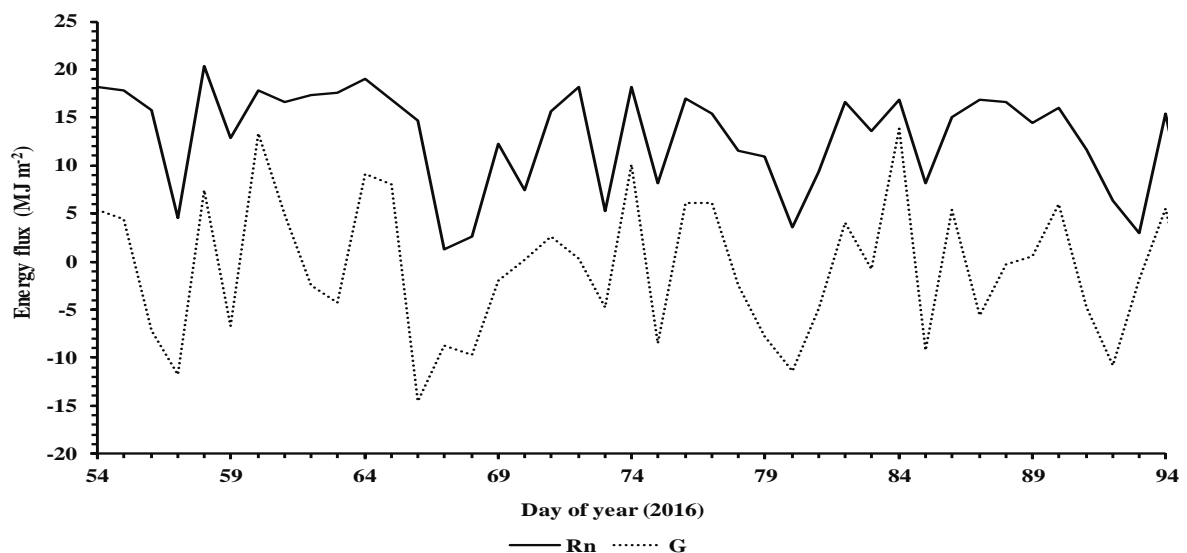


Figure 4.20: Temporal graph showing the variability of G and R_n measurements for Midmar Dam from 24 February to 4 April 2016.

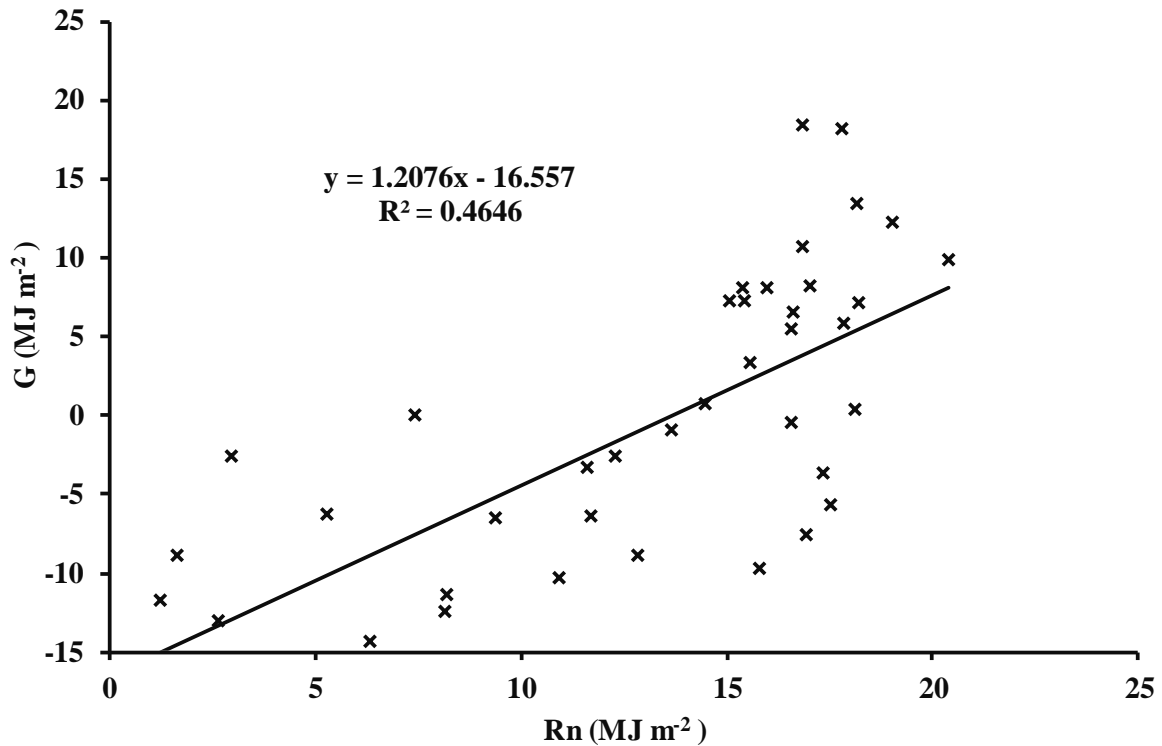


Figure 4.21: The regression graph of the daily G vs R_n for Midmar Dam from 24 February to 4 April 2016.

4.6 Modelling study at Midmar Dam

The DPMETHS model of Savage *et al.* (2016) that utilises the land-based meteorological data and the concepts of equilibrium temperature to estimate available energy flux at the water storage was new and the promising model that has not been used in any known study in South Africa for open water. To evaluate the performance of the DPMETHS model to simulate available energy flux at water storage, basic meteorological data obtained from the land-based station located near the dam were used as the inputs to the DPMETHS.

4.6.1 Comparisons between land and water meteorological measurements

Everson (1999) noted that large errors in the model simulations could be introduced using land-based meteorological data that do not represent conditions over open water surfaces. To investigate the relationships between meteorological measurements made over water and land-based measurements, the comparisons were made between 30-min meteorological data from water-based and land-based stations for the period between 24th February to 9th March 2016.

The choice of these data sets was based on quality of hourly data available from the land-based station. The main aim of comparing these data sets was to justify the use of land-based measurements as an input to the DPMETHS model to simulate the available energy fluxes over open water surface at Midmar Dam.

4.6.1.1 Solar irradiance

A comparison between the daily total solar irradiance measured above water surface ($R_{s\ water}$) and that measured at the land surface ($R_{s\ land}$) indicated that about 94 % variation in the $R_{s\ water}$ can be explained by $R_{s\ land}$ (Figure 4.22).

4.6.1.2 Air temperature

Temporal variation in air temperature measured above water ($T_{air\ water}$) and that measured at land surfaces ($T_{air\ land}$) indicated that $T_{air\ land}$ followed the same diurnal variation as $T_{air\ water}$ (Figure 4.23). A comparison between $T_{air\ water}$ and $T_{air\ land}$ indicated that about 97 % variation in the $T_{air\ water}$ can be explained by the $T_{air\ land}$ (Figure 4.24).

4.6.1.3 Wind speed

Temporal variation in wind speed measured above land surface (U_{land}) and that measured above water surface (U_{water}) indicated that U_{land} followed the same diurnal variation as U_{water} (Figure 4.25). Unexpectedly, U_{water} was maximum during night-time and minimal early in the morning. Furthermore, U_{water} was always greater than U_{land} due to open fetch on the water-based station compared to the land-based station which was closer to the buildings and trees. The smoother surface of open water compared to land could have resulted in greater wind speeds over the water surface than the land. These results are consistent with the observations reported by Finch and Hall (2001).

4.6.1.4 Relative humidity

Temporal variation in relative humidity measured above land surface (RH_{land}) and that measured above water surface (RH_{water}) indicated that RH_{land} followed the same diurnal variation as RH_{water} , relative humidity being maximum during night-time and minimal during daytime (Figure 4.26). A comparison between RH_{water} and RH_{land} indicated that about 85 % variation in the RH_{water} can be explained by the measured RH_{land} (Figure 4.27).

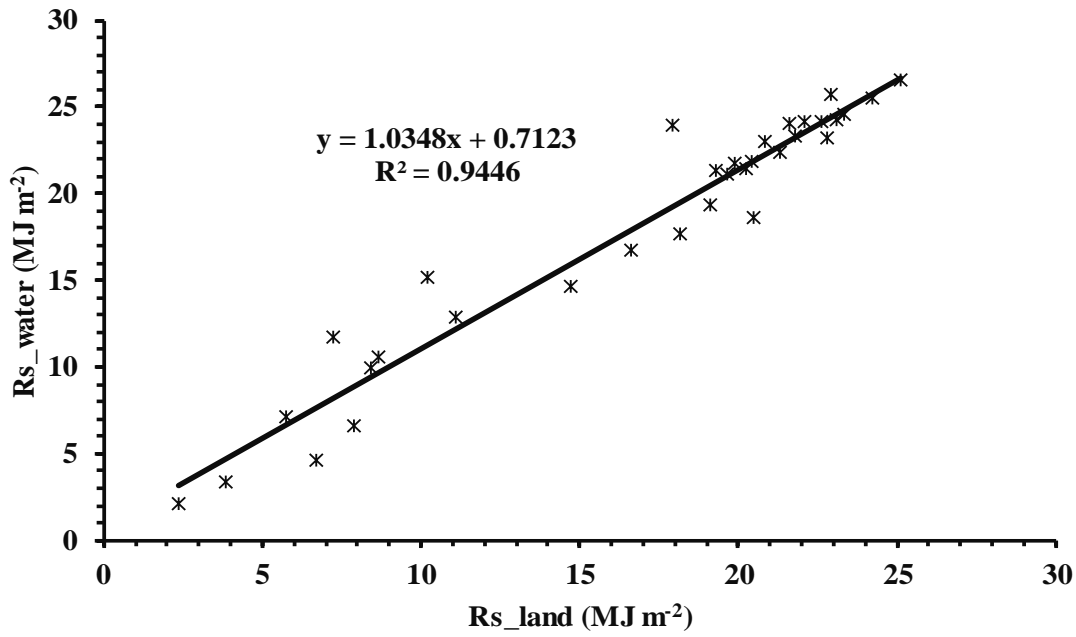


Figure 4.22: Regression graph of $R_{s\ water}$ and $R_{s\ land}$ for the period between 24th February and 9th March 2016 at Midmar Dam.

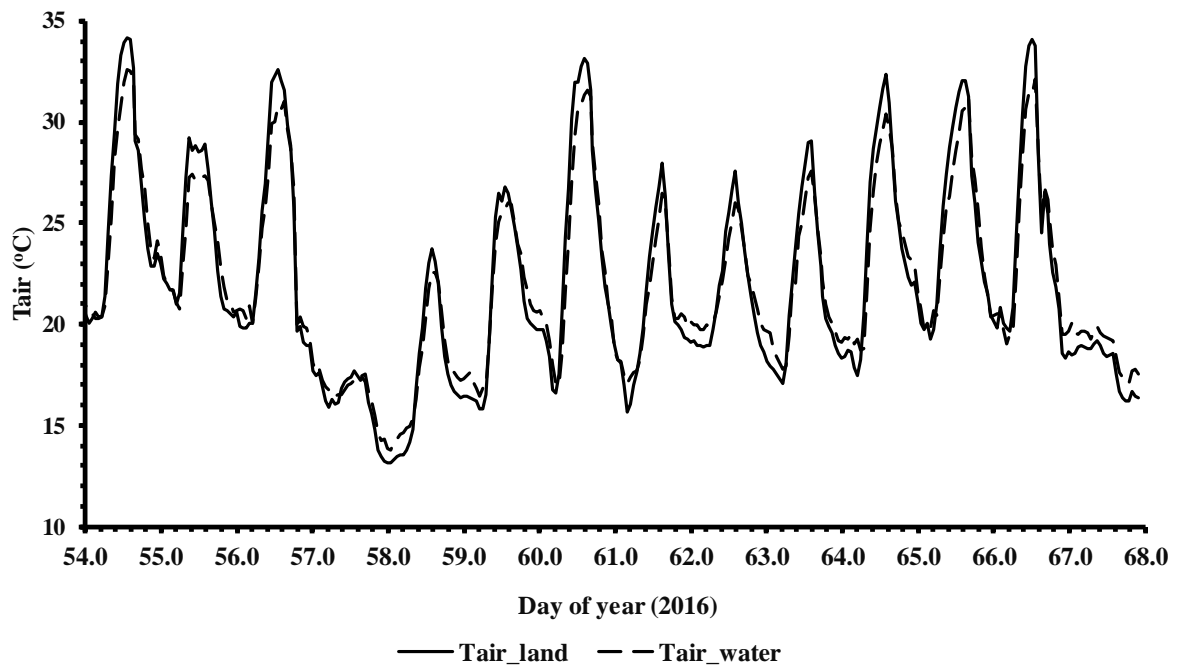


Figure 4.23: Temporal variation in $T_{air\ water}$ and $T_{air\ land}$ for the period between 24th February and 9th March 2016 at Midmar Dam.

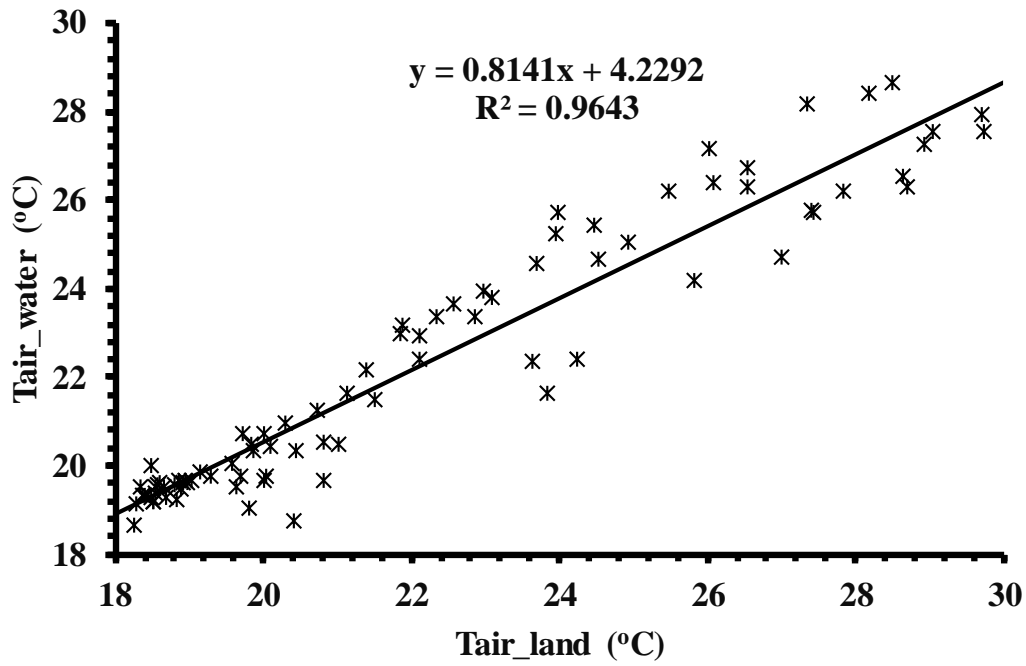


Figure 4.24: Regression plot of $T_{air\ water}$ vs $T_{air\ land}$ for the period between 24th February and 9th March 2016 at Midmar Dam.

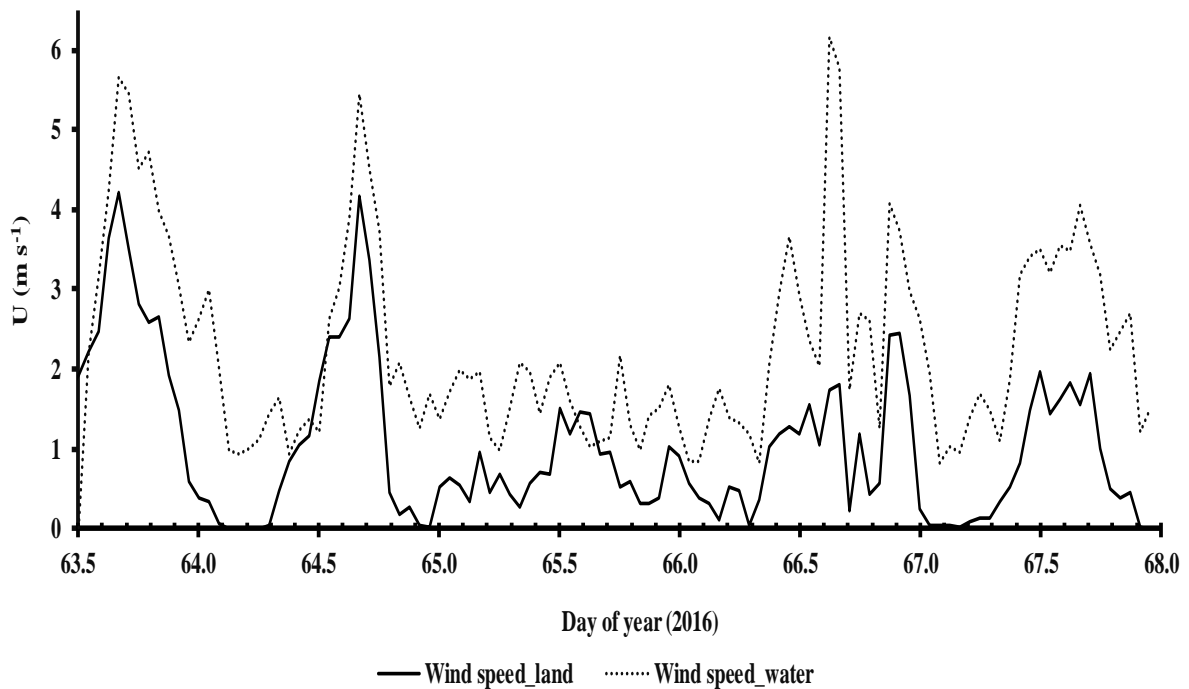


Figure 4.25: Temporal variation in U_{water} and U_{land} for the period between 24th February and 9th March 2016 at Midmar Dam.

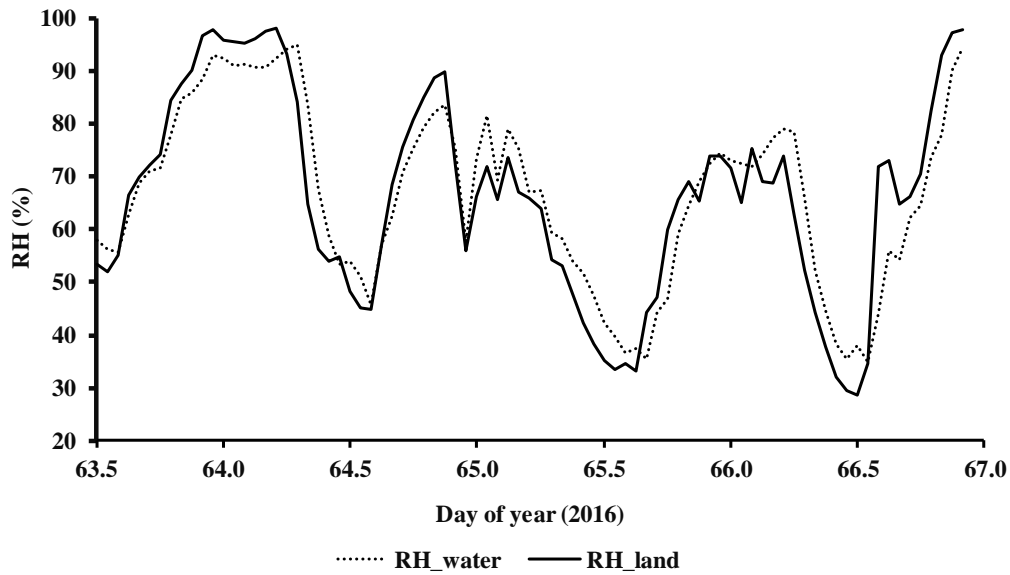


Figure 4.26: Temporal variation in RH_{water} and RH_{land} for the period between 24th February and 8th March 2016 at Midmar Dam.

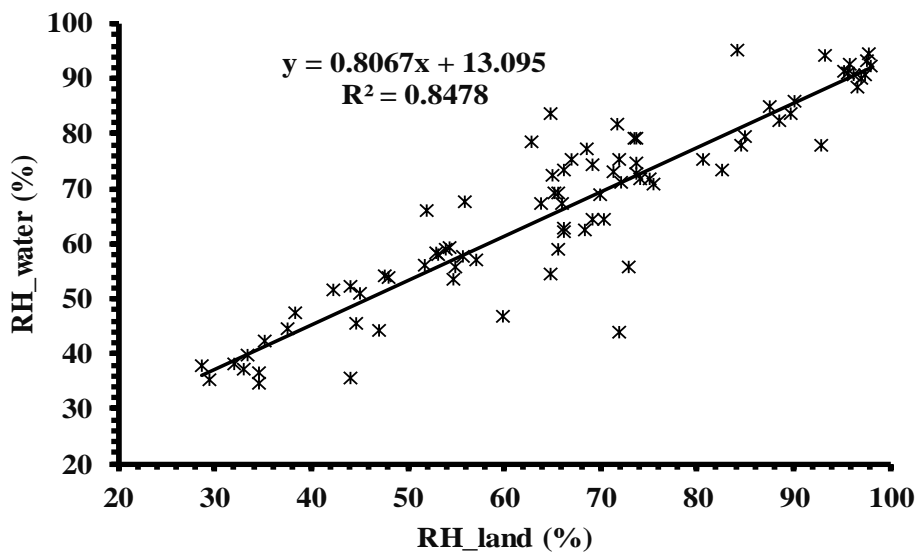


Figure 4.27: Regression plot of RH_{water} vs RH_{land} for the period between 24th February and 8th March 2016 at Midmar Dam.

4.6.1.5 General comments

Although there were differences between the measurements made over water and land-based measurements, good relationships were observed between these meteorological measurements. Therefore, there was no need to adjust the land-based data for modelling purposes.

4.6.2 Modelling radiative fluxes

Estimates of R_s , L_d , and L_u are computed within the DPMETHS during the computation of R_n from the land-based meteorological data using the iterative procedure. To evaluate the performance of the DPMETHS model to simulate R_n above water storage, the comparisons were made between the daily estimates of the radiative fluxes predicted from the DPMETHS model and the daily radiative fluxes measured above water at Midmar Dam.

4.6.2.1 Solar irradiance

The relationship between the daily estimates of R_s predicted from the DPMETHS model and the daily R_s measured above water indicated reasonable agreement (Figure 4.28). The regression graph between estimates of R_s and measured R_s indicated the statistically significant relationship between estimates of R_s and measured R_s , with slope (m) of 0.58 and regression coefficient (r^2) of 0.8 and intercept of 7.16 MJ m^{-2} (Figure 4.29). The r^2 indicated that about 80 % variation in the measured R_s can be explained by the model estimates of R_s . The root mean square error (RMSE) of 3.71 MJ m^{-2} indicated the model simulates R_s very well. However, the mean bias error (MBE) of 0.50 MJ m^{-2} indicated that the model over-simulated R_n during other days although such a small value of MBE indicated a better model performance. The calculated t-statistic value of 0.8 which was much less than the critical t-value of 2.66 obtained from the statistical tables indicated that estimates of R_s and measured R_s fluxes were not statistically different at the 99.5 % level of confidence.

4.6.2.2 Incoming infrared irradiance

The comparisons between the daily estimates of L_d predicted from the DPMETHS model and the daily L_d measured above water indicated reasonable agreement with both following the same variation (Figure 4.30). However, the model over-simulated the high values of L_d while under-simulated low values of L_d . The RMSE of 2.39 MJ m^{-2} indicated the model simulates L_d fairly. However, the MBE of 1.05 MJ m^{-2} indicated that the model often over-simulated L_d . The calculated t-statistic value of 3.1 which was greater than the critical t-value of 2.66 obtained from the statistical tables indicated that the estimated L_d and measured L_d fluxes were statistically different at the 99.5 % level of confidence.

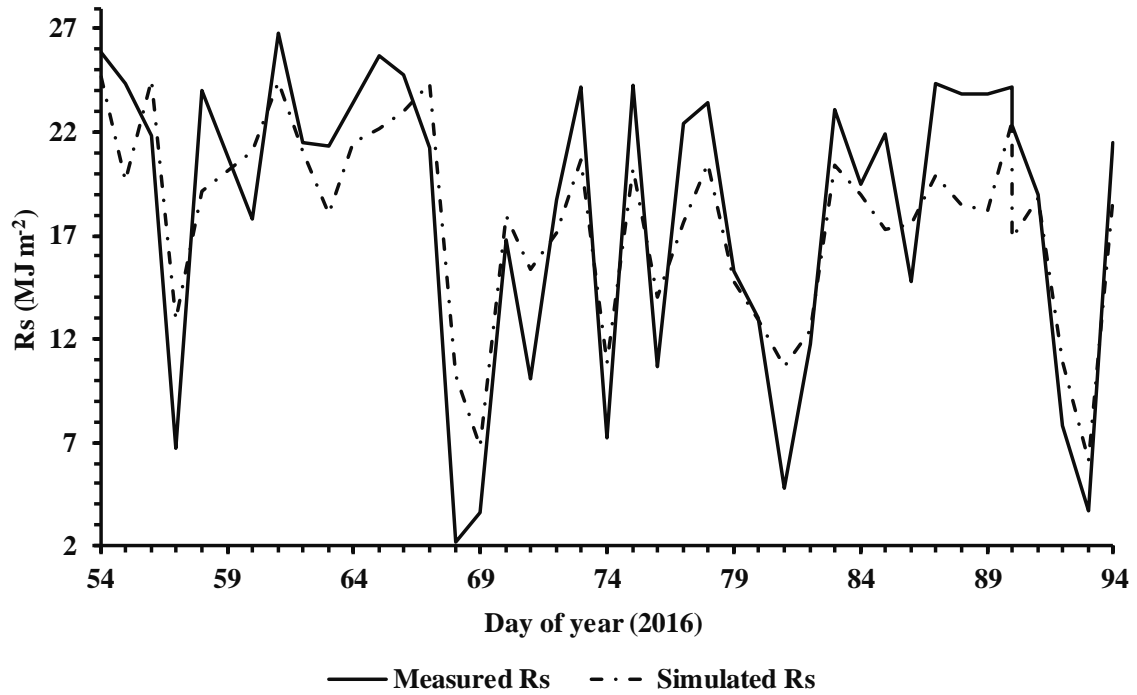


Figure 4.28: The comparison between the daily measured and the simulated R_s above open water at Midmar Dam from 24th February to 4th April 2016.

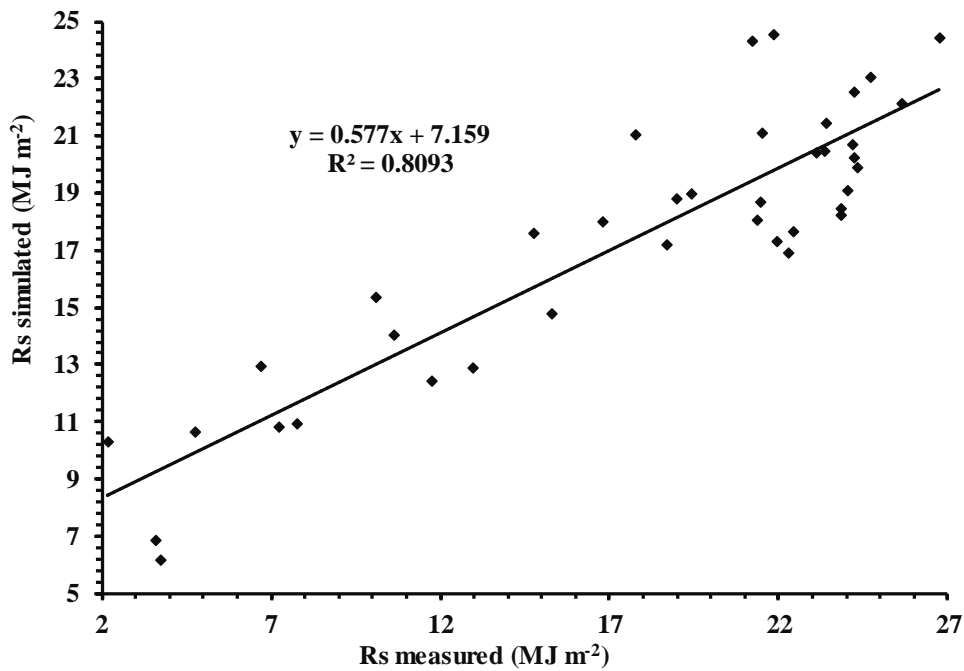


Figure 4.29: The regression graph of the measured and the simulated R_s above open water at Midmar Dam from 24th February to 4th April 2016.

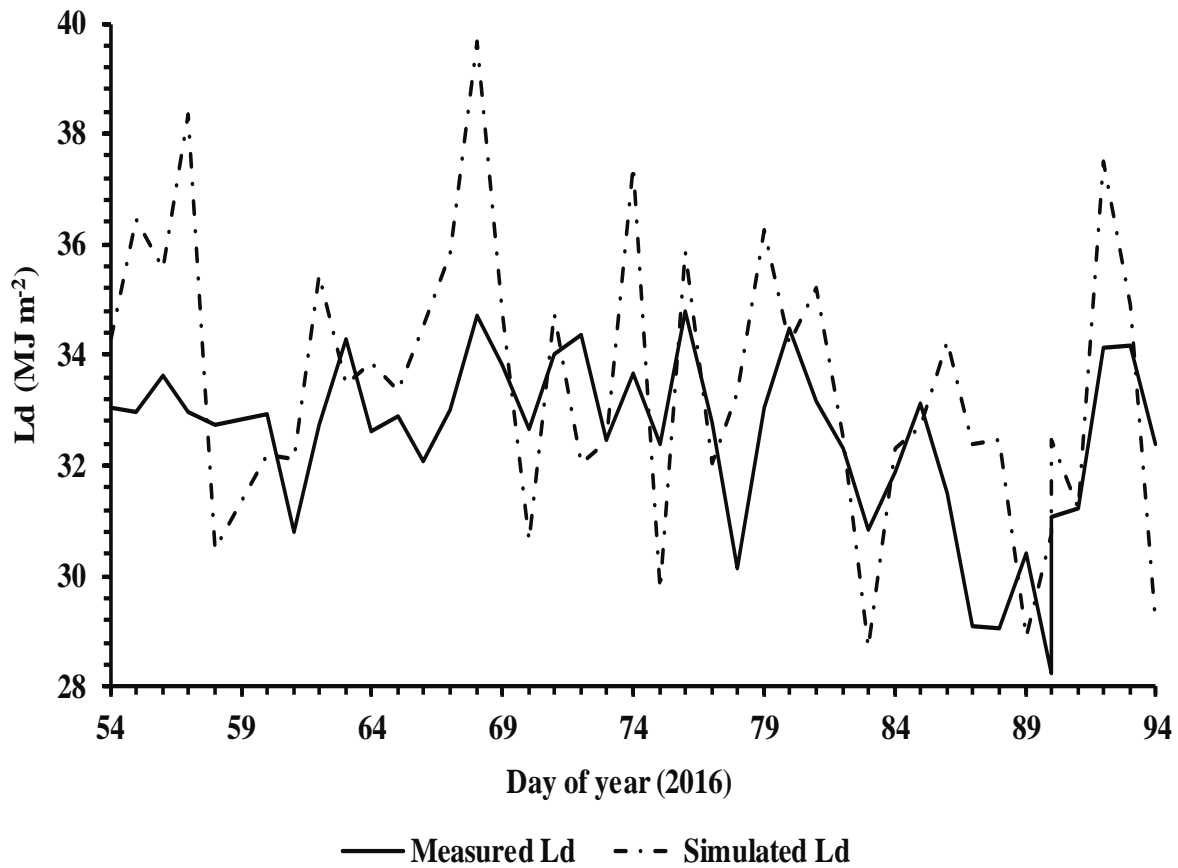


Figure 4.30: The comparison between the daily measured and the simulated L_d above open water at Midmar Dam from 24th February to 4th April 2016.

4.6.2.3 Outgoing infrared irradiance

The comparisons between the daily estimates of L_u predicted from the DPMETHS model and the daily L_u measured above water indicated reasonable agreement with both following the same variation (Figure 4.31). The RMSE of 1.30 MJ m^{-2} indicated the model simulates L_u very well. However, the MBE of 0.58 MJ m^{-2} indicated that the model often over-simulated L_u although such a small value of MBE indicated a better model performance. The calculated t-statistic value of 3.1 which was greater than the critical t-value of 2.66 obtained from the statistical tables indicated that the estimated L_d and measured L_d fluxes were statistically different at the 99.5 % level of confidence.

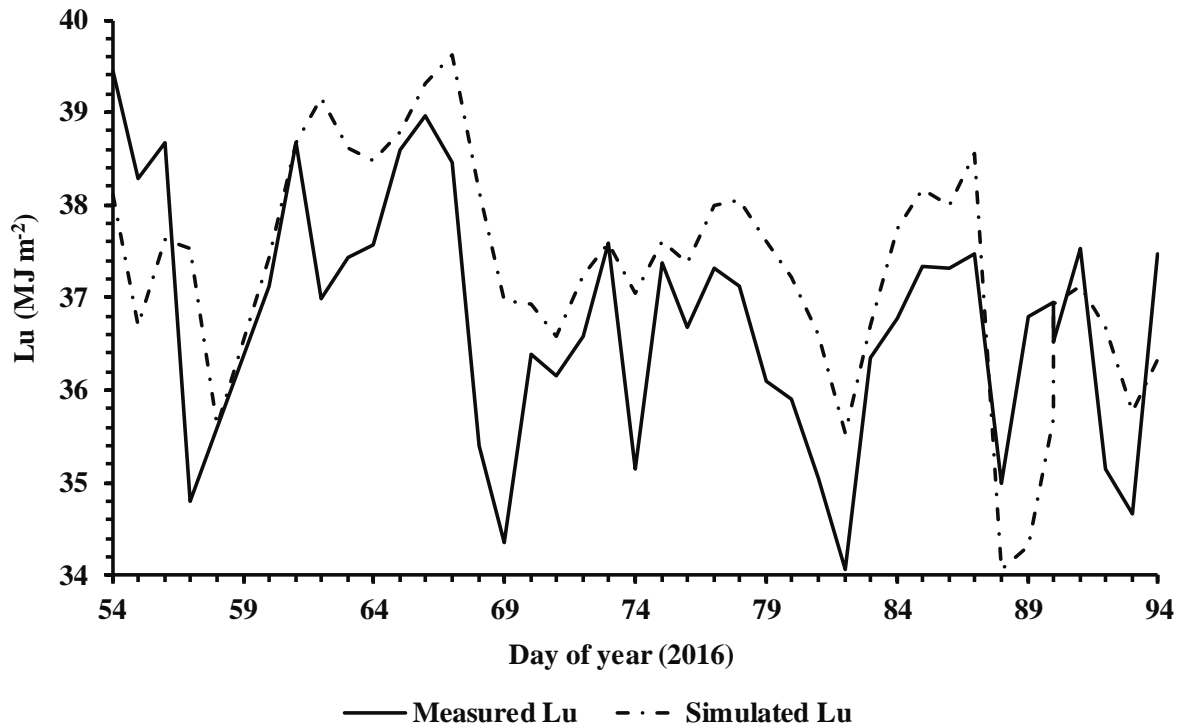


Figure 4.31: The comparison between the daily measured and the simulated L_u above open water at Midmar Dam from 24th February to 4th April 2016.

4.6.2.4 Net irradiance

The relationship between the daily estimates of the net irradiance (R_{ne}) predicted from the DPMETHS model using standard weather data and the daily net irradiance measured above water (R_n) was good (Figure 4.32). The regression graph between R_n and R_{ne} indicated the statistically significant relationship between R_n and R_{ne} , with m of 0.76 and r^2 of 0.70 and intercept of 3.60 MJ m^{-2} (Figure 4.33). The r^2 indicated that about 70 % variation in the R_n can be explained by the R_{ne} . The smaller RMSE of 3.04 MJ m^{-2} indicated the model simulates R_n very well. However, the MBE of 0.70 MJ m^{-2} indicated that the model over-simulated R_n during other days although such a small value of MBE indicated a better model performance. The calculated t-statistic value of 1.5 which was less than the critical t-value of 2.66 obtained from the statistical tables indicated that R_n and R_{ne} fluxes were not statistically different at the 99.5 % level of confidence.

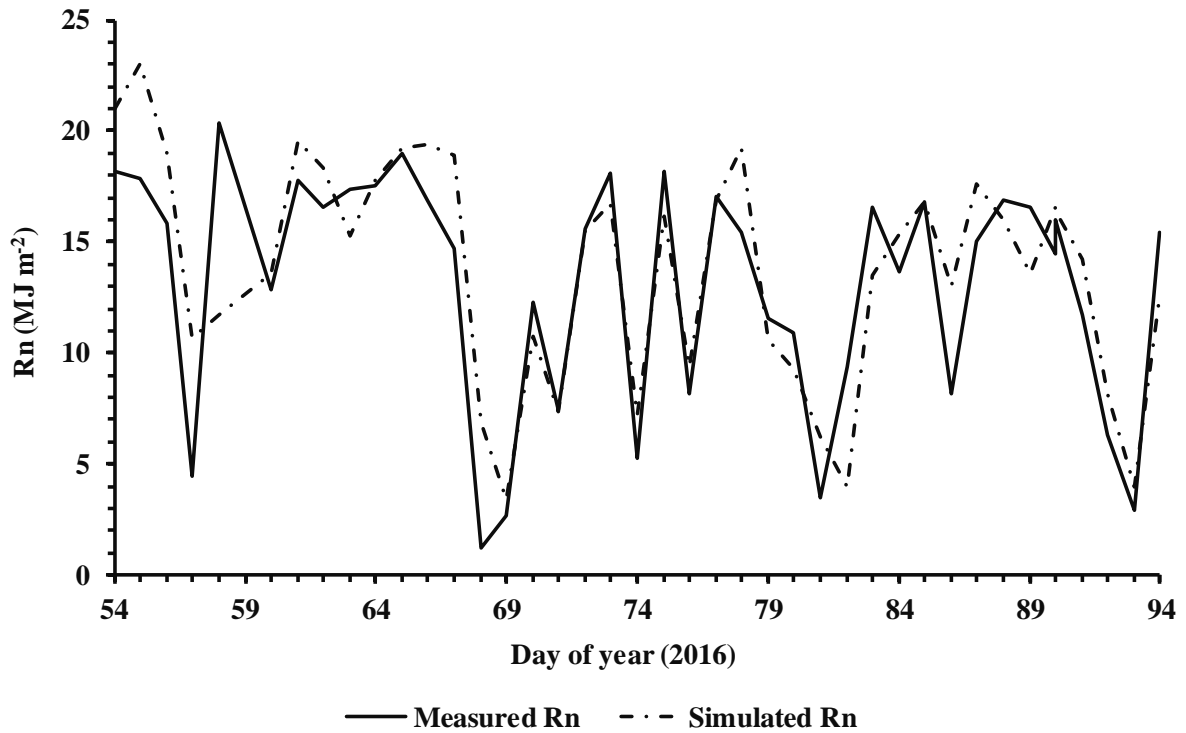


Figure 4.32: The comparison between the daily measured and the simulated R_n above open water at Midmar Dam from 24th February to 4th April 2016.

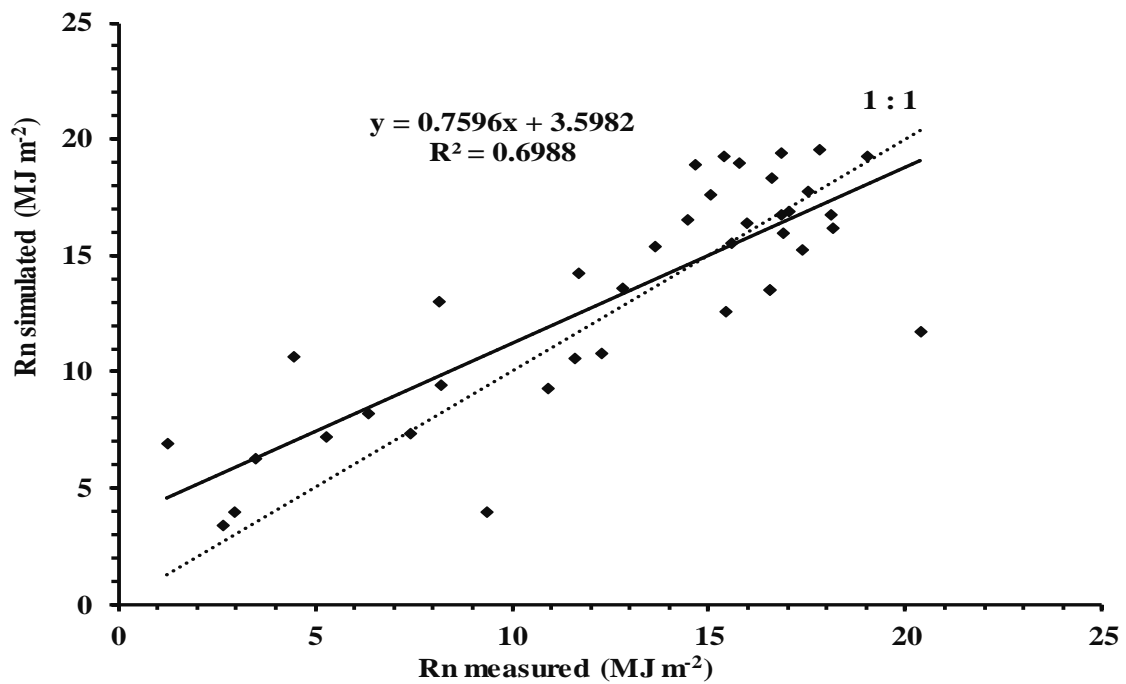


Figure 4.33: The regression graph of the measured and the simulated R_n above open water at Midmar Dam from 24th February to 4th April 2016.

4.6.2.5 Overall discussion on modelling of the radiative fluxes at Midmar Dam

Major under-simulations of R_n were observed during overcast days. For example, R_{ne} was 11.75 MJ m^{-2} compared to R_n of 20.38 MJ m^{-2} during the DOY 58 with 100 % relative humidity and minimal air temperature of $16.36 \text{ }^\circ\text{C}$, occurred just after DOY 57 with 6.35 mm of the daily total rainfall and daily total solar irradiance of 6.69 MJ m^{-2} . Furthermore, during the DOY 58, the estimated L_d was 30.49 MJ m^{-2} compared to the measured L_d of 32.73 MJ m^{-2} . The under-simulation of R_n during the overcast days is attributed to the under-simulation of L_d due to poor estimation of cloud fraction within the DPMETHS model. The Brunt's formula used in the model to estimate L_d was established only for clear-skies and may be not valid during the overcast days since clouds increase the atmospheric emissivity as also noted by Ortega-Farias (2000). Allan (2011) argue that although cloud fraction can be fairly estimated throughout the day in the model but lacks consistency (visual observations) since whether a given cloud will heat or cool the surface depends on the size of the cloud, the composition of the cloud and the cloud's altitude. Santos *et al.* (2011) also noted that L_d was one of the most difficult components of the radiation balance to estimate. Furthermore, assuming a constant r of 0.08 in the DPMETHS model during computation of rR_s could have resulted in slight under-simulation of R_n fluxes due to over-estimation of rR_s which reduces R_s , as illustrated in Section 4.4.1.2 (b).

Major over-simulations of R_n were observed during the days where there was greater contrast between the SWT and T_{air} . For example, R_{ne} was 18.92 MJ m^{-2} compared to R_n of 14.67 MJ m^{-2} during the DOY 67 with daily-average SWT of $23.9 \text{ }^\circ\text{C}$ compared to T_{air} of $18.8 \text{ }^\circ\text{C}$, the estimated L_u was 39.62 MJ m^{-2} compared to R_n of 38.45 MJ m^{-2} . The DPMETHS model predicts L_u based on the assumption that the SWT is equal to the T_{air} . However, daily-average T_{air} was observed to be less than SWT (Figure 4.14). Alcântara *et al.* (2010) noted that the greater the contrast between the SWT and T_{air} , the greater the L_u . The model over-simulated R_n in days where the contrast between the SWT and T_{air} was larger due to under-simulated L_u within the model. The DPMETHS model also uses U_{land} as input, however, U_{water} was observed to always be greater than U_{land} (Figure 4.25). The DPMETHS model, a daily model, is dependent on the daily-averaged wind speed and therefore does not explicitly account for night-time R_n which is dominated by L_u that is directly governed by SWT . Higher wind speed at night-time than expected, could have resulted in surface cooling and decreased SWT .

Consequently, the model slight over-simulated R_n due to under-simulations of L_u during clear, windy days. For example, R_{ne} was 10.67 MJ m^{-2} compared to R_n of 4.48 MJ m^{-2} during the DOY 57 with daily-average U_{water} of $23.9 \text{ }^\circ\text{C}$.

4.7 Modelling study at Stratus station, East Pacific Ocean

The DPMETHS model to estimate the available energy flux for open water evaporation is in its developmental stage and has not been used in any known study. Therefore, the estimates of the radiative flux from the DPMETHS model were tested for goodness of fit against measurements of the radiative flux from the ocean, under different climatic conditions. The ocean data used in this study were acquired at the Stratus station, located off the coast of Peru in South America in the Pacific Ocean. The constant reflection coefficient (r) of 0.08 was used to estimates of rR_s from measurements of R_s above the ocean surface. The estimates of L_u from the ocean surface were computed from sea surface temperatures using Eq. 2.1. The daily estimates of the radiative fluxes for R_s , L_d , and L_u were obtained by summing the hourly data for each day (01h00 to 24h00). Then, the daily R_n of the ocean were computed using Eq. 2.3.

4.7.1 Modelling radiative fluxes at Stratus station, East Pacific Ocean

The DPMETHS model was run for the eastern Pacific Ocean using meteorological daily data of solar irradiance, air temperature, relative humidity, wind speed, wind direction and rainfall measured over water at the ocean as well as the surface area and water depth of the ocean. To evaluate the performance of the DPMETHS model to simulate R_n above the ocean, the comparisons were made between the daily estimates of the radiative fluxes predicted from the DPMETHS model and the daily radiative fluxes measured above water at the ocean.

4.7.1.1 Incoming infrared irradiance

The comparisons between the daily estimates of L_d predicted from the DPMETHS model and the daily L_d measured above the ocean indicated reasonable agreement with both following the same variation (Figure 4.34). The smaller RMSE of 1.72 MJ m^{-2} indicated the model simulates L_d very well. However, the MBE of -1.40 MJ m^{-2} indicated that the model often under-simulated L_d although such a small value of MBE indicated a better model performance. The calculated t-statistic value of 9.3 which was greater than the critical t-value of 2.66 obtained

from the statistical tables indicated that the estimated L_d and measured L_d fluxes were statistically different at the 99.5 % level of confidence.

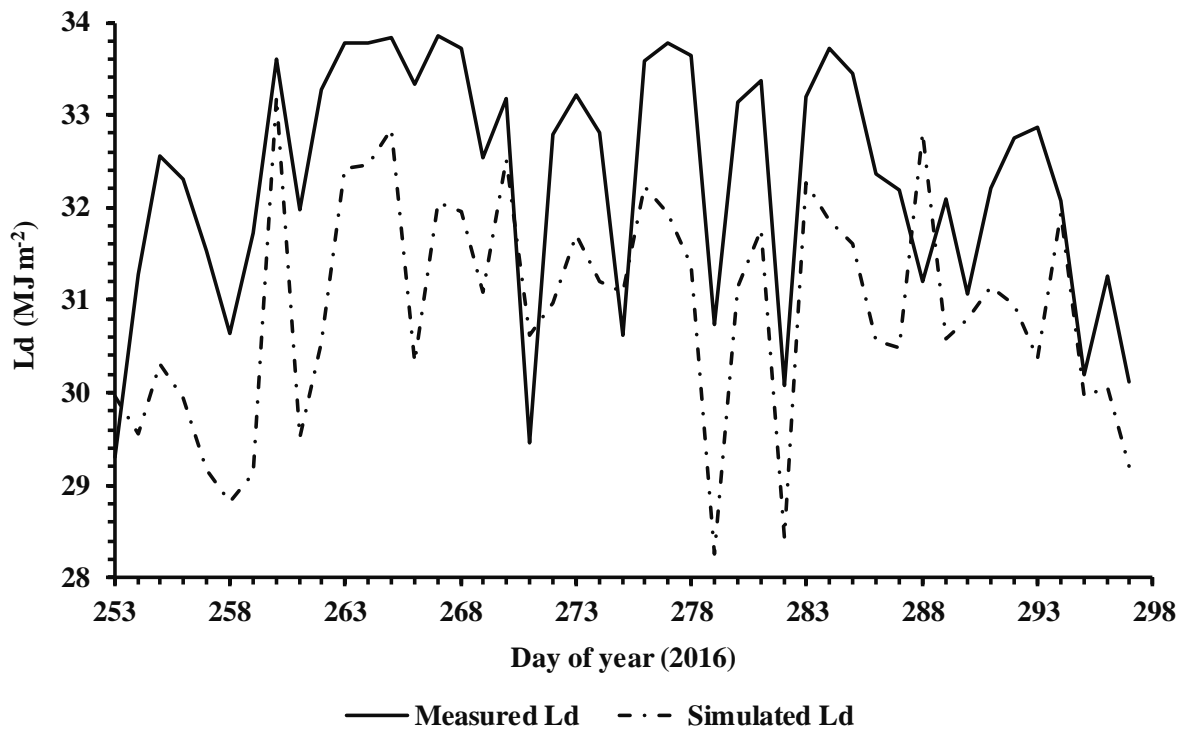


Figure 4.34: The comparison between the daily measured and the simulated L_d for the Stratus station of the East Pacific Ocean from 10th September to 24th October 2016.

4.7.1.2 Net irradiance

The relationship between the daily estimates of the net irradiance (R_{ne}) predicted from the DPMETHS model and the daily net irradiance measured above water at the ocean (R_n) was good (Figure 4.35). The regression graph between R_n and R_{ne} indicated the statistically significant relationship between R_n and R_{ne} , with m approaching 0.62 and r^2 of 0.76 and intercept of 11.14 MJ m⁻² (Figure 4.36). The r^2 indicated that about 76 % variation in the R_n can be explained by the R_{ne} . The RMSE of 5.67 MJ m⁻² indicated the model simulates R_n very well. However, the MBE of 5.45 MJ m⁻² indicated that the model often over-simulated R_n although such a small value of MBE indicated a better model performance. The calculated t-

statistic value indicated that R_n and R_{ne} fluxes were not statistically different at the 99.5 % level of confidence.

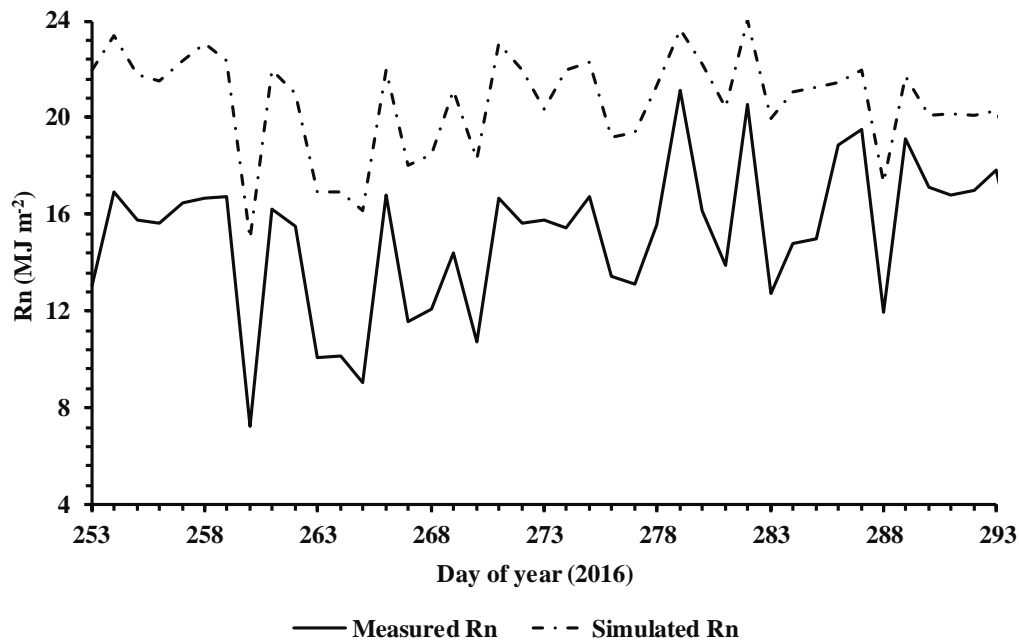


Figure 4.35: The comparison between the daily measured and the simulated R_n for the Stratus station of the East Pacific Ocean from 10th September to 24th October 2016.

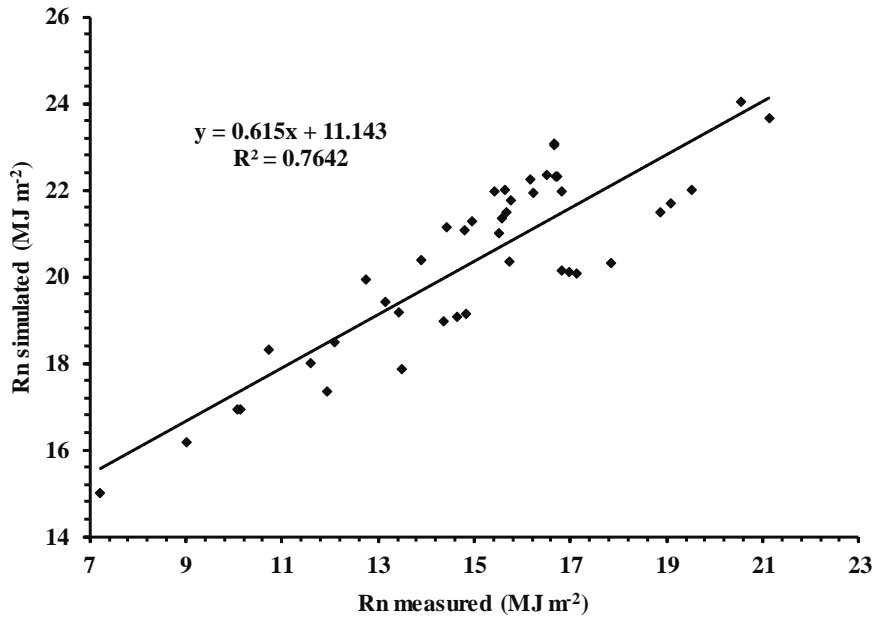


Figure 4.36: The regression graph of the measured and the simulated R_n for the Stratus station of the East Pacific Ocean from 10th September to 24th October 2016.

4.7.2 Overall discussion on modelling of the radiative fluxes at Stratus ocean station

Based on the results of the performance evaluation of the DPMETHS model presented above, it is suggested that the application of the DPMETHS model to estimate R_n for open water evaporation is viable. The presence of the low, thick stratus clouds above the ocean, as noted by Nowak *et al.* (2008), emitted greater L_d than expected. The observed poor estimation of L_d within the DPMETHS model is attributed to the failure of the model to simulate the impacts of the low, thick stratus clouds above the ocean. The DPMETHS model only estimated the cloud fraction with no optical properties. However, whether the presence of clouds will have a net cooling or warming effect at the water surface depends on the cloud optical properties such as the cloud's altitude, its size, and the make-up of the particles that form the cloud (Key *et al.*, 1996). The DPMETHS model over-simulated R_n during the entire study period at the ocean where daily data of the water depth and surface area were missing. Despite these problems associated with poor model input data, results produced are generally acceptable and it is believed that the DPMETHS model can be used to estimate R_n for the ocean surface.

4.8 Potential impacts of climate change on the radiation balance of Midmar Dam

Climate change has already altered, and will continue to alter the different components of the hydrological cycle such as evaporation (IPCC, 2014). However, the impacts of climate change on evaporation are not yet fully understood given that different components of evaporation will be affected differently (CSIR, 2010). Furthermore, the lack of a long-term record of R_n data over water surfaces hinders the evaluation of the potential impacts of climate change on the radiation balance which is one of the main drivers of evaporation. The availability of long-term meteorological dataset at Cedara station near Midmar Dam enables the unique opportunity to investigate the potential impacts of climate change on the radiation balance of Midmar Dam.

4.8.1 Long-term radiation balance of Midmar Dam

To investigate the potential impacts of climate change on the radiation balance of Midmar Dam, the variation of long-term daily estimates of the radiative fluxes predicted from the DPMETHS model were evaluated. The variation in annual average daily R_n ranged between 6.62 to 9.65 MJ m⁻² (Figure 4.37). Of particular note is the large increase in annual average daily R_n by an average of 1.23 MJ m⁻² from year 2005 to 2015.

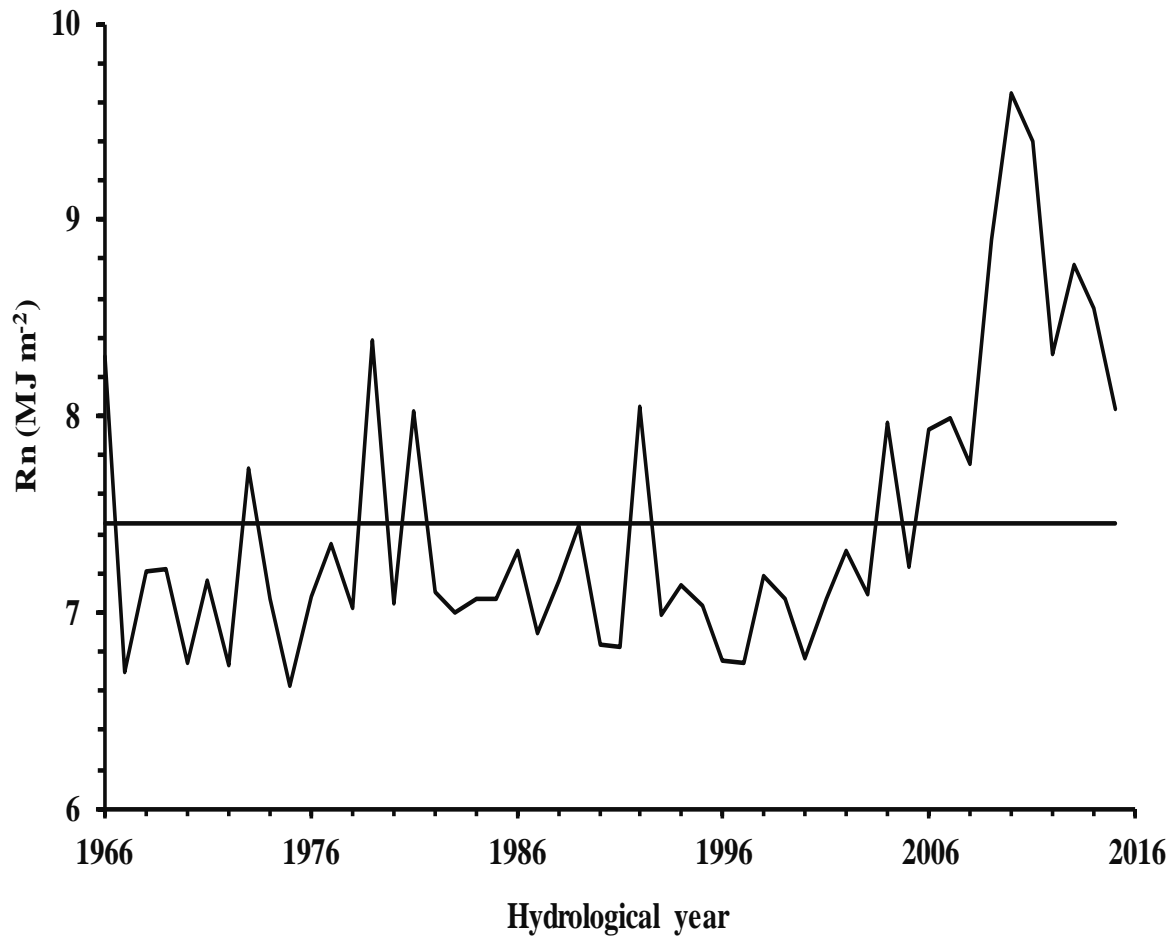


Figure 4.37: Temporal variation in annual average daily R_n for the period between year 1966 and 2015 (inclusively) at Midmar Dam.

To investigate the possible cause of the increase in R_n for this period, variation of annual average estimates of R_s , L_u , and L_d were evaluated. The variation in the annual average daily R_s indicated that R_s decreased by an average of 1.14 MJ m^{-2} from year 2005 to 2015 (Figure 4.38). Therefore, the variation in annual average daily R_s trend yielded no clue of the possible cause of the increase in R_n between year 2005 and 2015. The variation in the annual average daily L_u trend also yielded no clue of the possible cause of the increase in R_n between year 2005 and 2015 (Figure 4.39). The variation in annual average daily L_d indicated the large increase in L_d by 0.49 MJ m^{-2} per annum from year 2005 to 2015 (Figure 4.40). The large increases in L_d is consistent with the increases in R_n for the period between year 2005 and 2015.

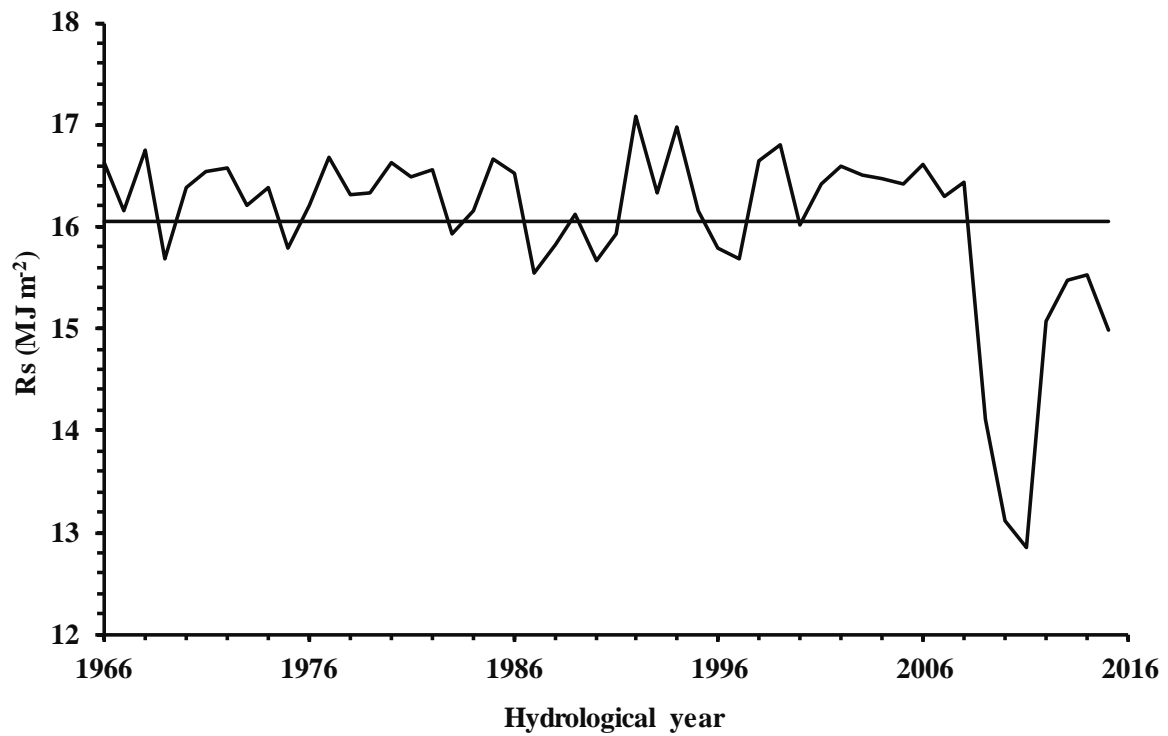


Figure 4.38: Temporal variation in annual average daily R_s for the period between year 1966 and 2015 (inclusively) at Midmar Dam.



Figure 4.39: Temporal variation in annual average daily L_u for the period between year 1966 and 2015 (inclusively) at Midmar Dam.

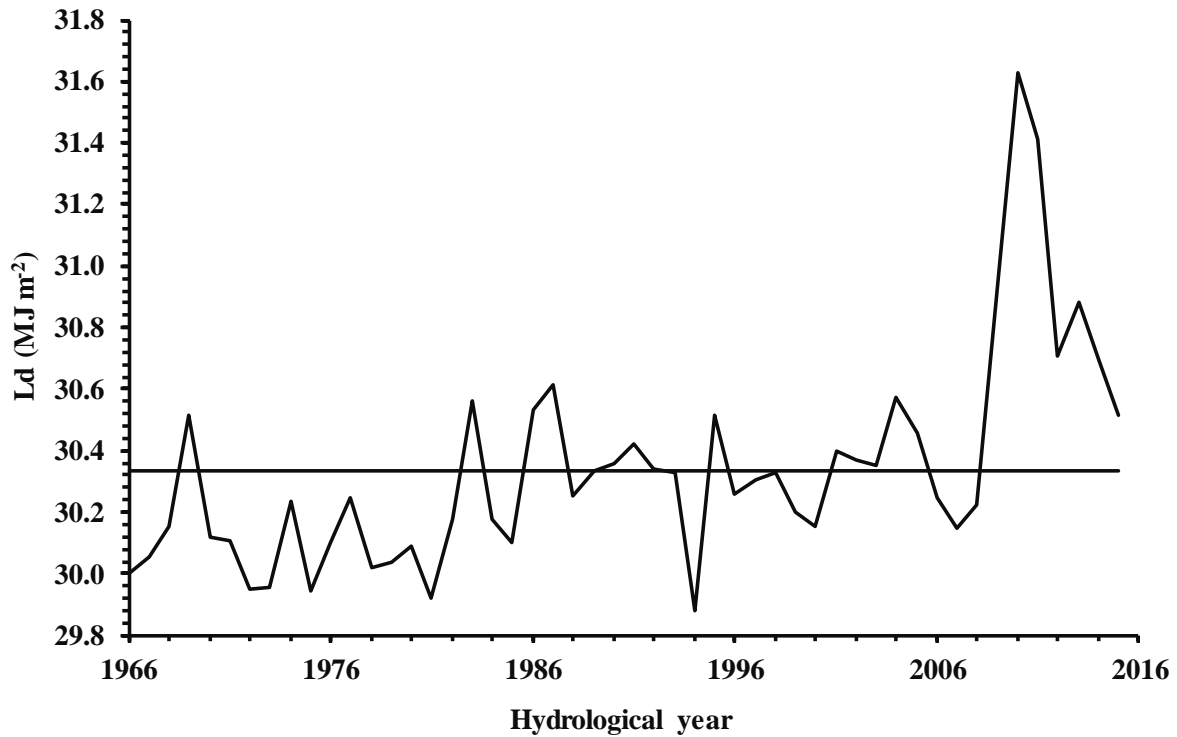


Figure 4.40: Temporal variation in annual average daily L_d for the period between year 1966 and 2015 (inclusively) at Midmar Dam.

4.8.2 Overall discussion on the potential impacts of climate change on the radiation balance of Midmar Dam

The large increase in R_n from year 2005 to 2015 is attributed to the increase in L_d for the same period. IPCC (2014) reported that the total carbon dioxide (CO_2) emissions have continued to increase over 1970 to 2010 with larger absolute increases between 2000 and 2010, despite a growing number of climate change mitigation policies. The increase in L_d is consistent with the increase in total CO_2 emissions reported globally since CO_2 is a very strong absorber and emitter of infrared radiation. The presence of high concentrations of CO_2 in the atmosphere prevented most of L_u from escaping into the space through the atmospheric window. The absorbed L_u was then reradiated back to water surface as L_d and resulted in an increase in L_d which caused a change of the radiation balance. Consequently, the average air temperatures increased by an average of $0.36\text{ }^\circ\text{C}$ per annum from year 2005 to 2015 (Figure 4.41). These findings are consistent with the observed increase in global average temperatures over the past 50 years due to the observed increase in anthropogenic greenhouse gas concentrations reported by IPCC (2014). However, the change in the radiation balance did not change the global average air

temperature instantaneously. Instead, the impacts of the changes in the radiation balance were felt more five years later where 2010 was the hottest year. The lag between when radiation imbalance occurs and when the impact on air temperature becomes fully apparent is mostly because of the large heat capacity of the global ocean. Consequently, the large amount of energy absorbed by the ocean for evaporation, partially buffers the global warming as a results of climate change as also noted by Ramanathan and Feng (2009).

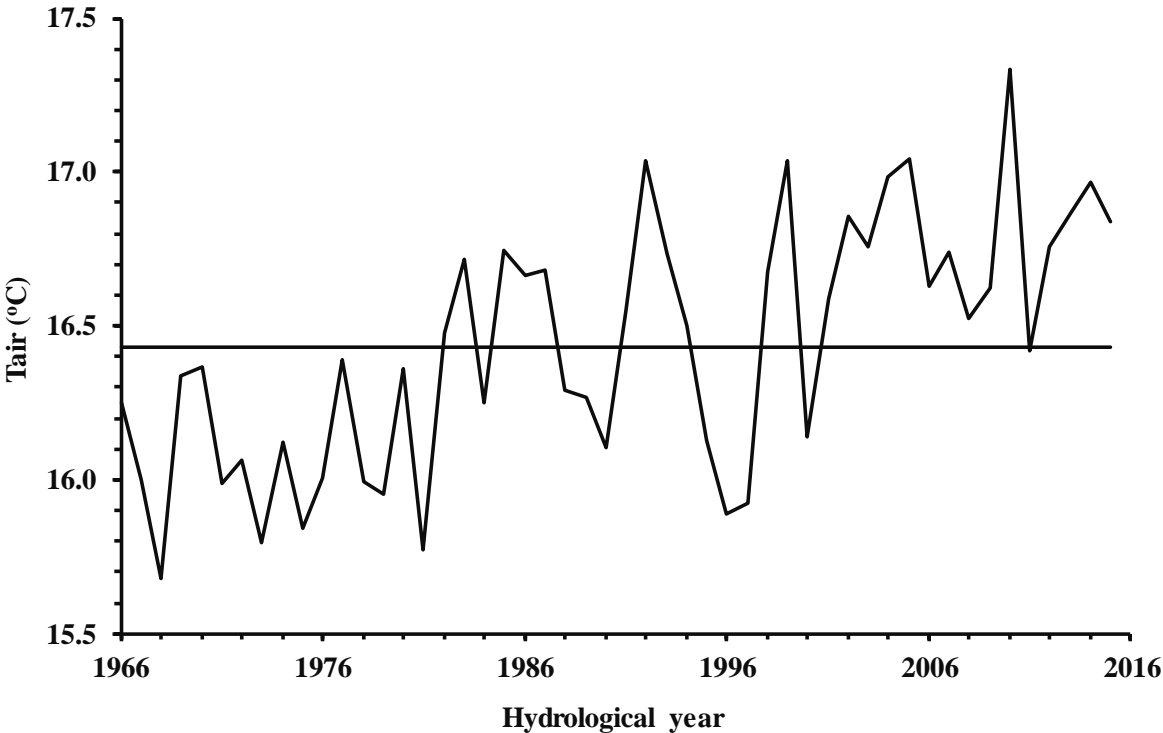


Figure 4.41: Temporal variation in annual average daily air temperature for the period between year 1966 and 2015 (inclusively) at Midmar Dam.

4.8.3 General comments

This study showed evidence of the impacts of climate change on the radiation balance of Midmar Dam. Climate changes attributed to the increasing concentrations of CO₂ threaten to increase the long-term air temperatures of the earth with consequent increase in R_n due to increases in L_d .

CHAPTER 5 : CONCLUSIONS AND RECOMMENDATIONS FOR FURTHER RESEARCH

5.1 Introduction

The main aim of this study was to understand the factors enhancing temporal and spatial variability of the radiation balance at water storage and to evaluate the performance of the DPMETHS model to simulate available energy flux above open water at Midmar Dam and for an eastern Pacific Ocean site. The objectives of the research were:

- To improve an understanding of the variability of the radiation balance and available energy above open water storage and assessing the factors that affect the radiation balance above open water;
- To evaluate the performance of the DPMETHS model to simulate the daily available energy flux at Midmar Dam and at the ocean Pacific Ocean;
- To investigate the potential impacts of climate change on the radiation balance of Midmar Dam.

5.2 Findings

The cloud cover, reflection coefficient of water (r), air temperature (T_{air}) and surface water temperature (SWT) were the main factors that control the temporal and spatial variability of radiation balance above open water surface. The net irradiance (R_n) fluxes were minimal during an overcast day compared to a clear-sky day and this indicated that clouds had an average cooling effect on the water surface of Midmar Dam. The r directly determined the amount of the incoming solar irradiance (R_s) absorbed by the water surface and a turbid water body reflected more R_s . The observed r values showed the strong diurnal variation and there was high water reflectivity at lower sun's angles. For the entire study period, daily r ranged between 0.05 and 0.14 and the daily-average r of 0.08 was observed. The SWT controls the outgoing infrared irradiance (L_u) while T_{air} affects water vapour pressure which controls the incoming infrared irradiance (L_d). Minimum T_{air} and SWT values were observed just before the sunrise while maximum temperatures were observed during the late afternoon. However, during the daytime, T_{air} was greater than SWT while during the night-time the observations were inverted.

The range in diurnal SWT measurements was less than that for T_{air} due to greater specific heat capacity of water compared to air. The spatial variation of R_n above open water is mainly due to the spatial variability in SWT since with constant emissivity, L_u depends on SWT alone. The *in-situ* measurement of SWT compared well to the Landsat-8 estimate of SWT . Water near the shore responded to the atmospheric conditions very quickly compared to the offshore water. Consequently, water near the shore was observed to always be warmer than offshore water by an average of 1.5 °C. Furthermore, shallow parts of the dam were 2 °C warmer than the deeper part of Midmar Dam. The observed average of 1.5 to 2 °C variability of SWT across Midmar Dam implies the very low spatial variability of L_u which is temperature dependent. Therefore, the low spatial variability of SWT is associated with low spatial variation of R_n across the dam. The spatial variability of SWT across the dam indicated that point measurements of SWT are reasonable indicators of the reservoir SWT which is used to compute the water-stored heat flux (G) and L_u from the water surface at Midmar Dam.

The R_n was the dominant component of the available energy flux over water surface at Midmar Dam. During daytime, R_n fluxes were positive, corresponding to a source of energy while during night-time, R_n fluxes were negative, corresponding to a loss of energy from the water surface. The variability of the available energy flux at water storage indicated that G showed a similar diurnal variation to R_n with comparable magnitudes and peaked at the same time as the peak in R_n . For the entire study period, the temporal variability of G showed that during some days, heat was stored in water storage ($G > 0 \text{ W m}^{-2}$) while during other days, heat was released from water storage ($G < 0 \text{ W m}^{-2}$). Therefore, G plays a significant role in the daily energy balance and cannot be neglected for accurate estimation of the daily open water evaporation. Even with using a running mean, estimates of G often showed very wide variation due to turbulent water waves of varying temperature travelling past the thermocouples. Consequently, estimates of G fluxes of Midmar Dam showed a very wide variation that was not attributed to variation in R_n and were unreliable.

This study showed that daily R_n can be simulated well from standard weather station data using the DPMETHS model at Midmar Dam. The under-simulation of R_n during overcast days were attributed to under-simulation of L_d due to poor estimation of cloud fraction using the Brunt's

formula that was established only for clear-skies. Furthermore, assuming a constant r of 0.08 in the DPMETHS model during computation of rR_s resulted in slight under-simulation of R_n fluxes due to over-estimation of rR_s which reduces R_n . The relative lack of validity of the assumption that the SWT is equal to the T_{air} together with the use of wind speed measured at the land-based station which was less than the wind speed at water surface as a model inputs resulted in the model under-simulating L_u which resulted on the over-simulation of R_n on some of the days. The presence of the low, thick stratus clouds above the ocean emitted greater L_d than expected and resulted on the poor simulations of L_d for Stratus station at eastern Pacific Ocean. Despite the problems associated with poor model input data, results produced are generally acceptable and it is believed that the DPMETHS model can be used to estimate R_n for the ocean surface.

This study showed evidence of the impacts of climate change on the radiation balance of Midmar Dam. Climate changes attributed to the global increase in the concentrations of total carbon dioxide threaten to increase the long-term air temperatures of the earth with consequent increase in R_n due to increases in L_d .

5.3 Challenges and recommendations for future research

Despite the free availability of the Landsat-8 data which provide synoptic and frequent acquisition of data over large areas, remote sensing is at its developmental stage and satellite-derived SWT need to be calibrated with ground truth SWT data which is not readily available at Midmar Dam. The main limitation of Landsat-8 is that satellites acquire data once in every 16 days at any given location and does not record data at night. Furthermore, satellites acquire data at local time 09h50, where the main factors driving SWT are minimal and images collected with cloud fraction of more than 60 % are discarded. Consequently, Landsat-8 data are not reliable representations of the temporal variability of daily SWT . The thermal infrared data from Landsat-8 is corrected for the solar elevation and atmospheric emissivity for quantitative assessment of SWT using empirical equations which introduce uncertainties in derived estimates of SWT . Only one Landsat-8 image was used in this study to assess spatial variability of SWT . It is recommended that in future studies on such large dams, more cloudless Landsat-

8 images should be collected and compared with *in-situ* measurements of *SWT* from stations installed permanently across the dam to represent the variability in *SWT* observed in this study.

This study showed that R_n can be simulated well from standard weather station data using the DPMETHS model. The DPMETHS model performed successfully on the Midmar Dam study and to a lesser extent at the ocean with stratus clouds and missing daily data of the water depth. The estimation of the cloud fraction within the DPMETHS model needs to be modified to account for optical cloud properties. This is because whether the presence of clouds will have a net cooling or warming effect at the water surface depends on the cloud optical properties such as cloud's altitude, its size, and the make-up of the particles. The limitations of the DPMETHS model is that it is complex and requires dam characteristics such as water depth and surface area which may be not readily available at the dam of interest. Furthermore, the lack of a long-term record of R_n data over water surface hindered the evaluation of the DPMETHS model to simulate seasonal variability of R_n . In future studies, the DPMETHS model should be validated in different water storages of different sizes representing the wide range of climatic conditions across all regions. Furthermore, a better and reliable method of measuring or estimating G is required since G fluxes were measured with great difficulty using thermocouples. Consequently, model estimates of G were not compared to unreliable measurements of G in this study. The lack of reliable measurements of G limited the evaluation of the DPMETHS model to compute G from land-based meteorological data. One of the limitations of the DPMETHS model is that the model utilizes the daily meteorological data which might not be a true representation of climatic conditions for the entire day, since most of the model inputs demonstrated a wide range of diurnal variability. For future research, it is recommended that a sub-daily model that also estimates available energy flux for open water evaporation based on land-based meteorological data is used for similar studies for improved estimates of available energy flux.

5.4 Final comments and summary

The DPMETHS model is a new and promising method for estimating the daily available energy flux for daily open water evaporation using readily available meteorological data. Consequently, the DPMETHS model can reduce the costs of estimating open water evaporation using the energy balance techniques by eliminating the need for measuring the net irradiance

with greater difficulty using the expensive net radiometers mounted above water. The lack of the long-term records of available energy flux data collected over water will still limit the evaluation and verification of the DPMETHS model in different water storages of different sizes across different climatic conditions. Therefore, more data need to be collected above water using permanent stations for extended periods.

CHAPTER 6 : REFERENCES

- Alcântara EHD, Stech JL, Lorenzetti JA, Bonnet MP, Casamitjana X, Assireu AT, de Moraes Novo EML. 2010. Remote sensing of water surface temperature and heat flux over a tropical hydroelectric reservoir. *Remote Sensing of Environment* 114(11): 2651-2665.
- Alcântara EHD, Stech JL, Lorenzetti JA, Novo EML. 2011. Time series analysis of water surface temperature and heat flux components in the Itumbiara Reservoir (GO), Brazil. *Acta Limnologica Brasiliensia* 23(3): 245-259.
- Allan RP. 2011. Combining satellite data and models to estimate cloud radiative effect at the surface and in the atmosphere. *Meteorological Applications* 18(3): 324-333.
- Allen RG, Pereira LS, Raes D, Smith M. 1998. Crop Evapotranspiration-Guidelines for computing crop water requirements-FAO Irrigation and drainage paper 56. FAO, Rome 300(9): D05109. Available at:
http://s3.amazonaws.com/academia.edu.documents/40878584/Allen_FAO1998.pdf?AWSAccessKeyId=AKIAJ56TQJRTWSMTNPEA&Expires=1477267084&Signature=hZg2Jt%2FggQSPf7i5GDYFBCM8DyU%3D&response-content-disposition=inline%3B%20filename%3DAllen_FAO1998.pdf [Accessed 3 March 2015].
- Arya PS. 2001. Introduction to micrometeorology (Vol. 79). Academic Press. New York, USA.
- Blonquist JM, Allen RG, Bugbee B. 2010. An evaluation of the net radiation sub-model in the ASCE standardized reference evapotranspiration equation: implications for evapotranspiration prediction. *Agricultural Water Management* 97: 1026–1038.
- Brotzge JA, Duchon CE. 2000. A field comparison among a domeless net radiometer, two four-component net radiometers, and a domed net radiometer. *Journal of Atmospheric and Oceanic Technology* 17(12): 1569-1582.
- Brunt D. 1934. *Physical and Dynamical Meteorology*. Cambridge University Press. UK
- Brutsaert W. 1982. *Evaporation into the Atmosphere*, Reidel Publishing Company, Dordrecht, Holland.
- Brutsaert W. 2013. *Evaporation into the atmosphere: theory, history and applications* (Vol. 1). Springer Science & Business Media. New York, USA.

- CSIR. 2010. A CSIR perspective on water in South Africa-2010. CSIR Report No. CSIR/NRE/PW/IR/2011/0012/A. Available at:
http://www.csir.co.za/nre/docs/CSIR%20Perspective%20on%20Water_2010.PDF
[Accessed 25 February 2015].
- de Bruin HAR. 1982. Temperature and energy balance of a water reservoir determined from standard weather data of a land station. *Journal of Hydrology* 593: 261–274.
- Department of Water Affairs and Forestry. 2007. Information on South African dams. Hydrological Services, Department of Water Affairs and Forestry. South Africa. Available on http://www.dwaf.gov.za/hydrology/dwafapp2_wma/ [Accessed 6 March 2015].
- Dong A, Grattan SR, Carroll JJ, Prashar CRK. 1992. Estimation of daytime net radiation over well-watered grass. *Journal of Irrigation and Drainage Engineering* 118(3): 466-479.
- Dozier J. 1980. A clear-sky spectral solar radiation model for snow-covered mountainous terrain. *Water Resources Research* 16 (4): 709-718.
- Duan Z. 2014. Estimating water balance components of lakes and reservoirs using various open access satellite databases. PhD thesis, Delft University of Technology, The Netherlands.
- DWAF. 2013. National Water Resource Strategy: Water for an Equitable and Sustainable Future. Department of Water Affairs Pretoria, South Africa. Available at: <https://www.dwa.gov.za/nwrs/LinkClick.aspx?fileticket=CIwWyptzLRk%3D&tabid=91&mid=496> [Accessed 14 March 2016].
- Edinger JE, Duttweiler DW, Geyer JC. 1968. The response of water temperatures to meteorological conditions. *Water Resources Research* 45: 1137–1143.
- Everson CS. 1999. Evaporation from the Orange River: quantifying open water resources. Water Research Commission. Report No.683/1/99. Available at:
<http://www.wrc.org.za/Knowledge%20Hub%20Documents/Research%20Reports/683-1-99.pdf> [Accessed 23 February 2015].
- Federer CA. 1968. Spatial variation of net radiation, albedo and surface temperature of forests. *Journal of Applied Meteorology* 7(5): 789-795.
- Finch J, Hall R. 2001. Estimation of open water evaporation. A review of methods. Environment Agency. Bristol, UK.
- Finch JW, Calver A. 2008. Methods for the quantification of evaporation from lakes. Available at: http://nora.nerc.ac.uk/14359/1/wmoevap_271008.pdf [Accessed 4 March 2015].

- Finch JW, Gash JHC. 2002. Application of a simple finite temperature difference model for estimating evaporation from open water. *Journal of Hydrology* 255: 252–259.
- Finch JW. 2001. A comparison between measured and modelled open water evaporation from a reservoir in south-east England. *Hydrological Processes* 15(14): 2771–2778.
- Fraederich K, Erath BG, Weber G. 1977. A simple model for estimating the evaporation from a shallow water reservoir. *Tellus* 29: 424-434.
- Gates DM. 1980. Longwave and total radiation. In *Biophysical Ecology* (pp. 148-180). Springer New York, USA.
- Geraldo-Ferreira E, Soria-Olivas J, Gómez-Sanchis AJ, Serrano-López A, Velázquez-Blázquez A, López-Baeza E. 2011. Modelling net radiation at surface using “*in-situ*” netpyrradiometer measurements with artificial neural networks. *Expert Systems with Applications* 38(11): 14190-14195.
- Granger RJ, Hedstrom N. 2011. Modelling hourly rates of evaporation from small lakes. *Hydrology and Earth System Sciences* 15(1): 267-277.
- Hargreaves GH, Samani ZA. 1982. Estimation of potential evapotranspiration. *Journal of Irrigation and Drainage Division, Proceedings of the American Society of Civil Engineers* 108: 223-230.
- Hatzianastassiou N, Vardavas I. 2001. Shortwave radiation Budget of the Southern Hemisphere using ISCCP C2 and NCEP-NCAR climatological data. *Journal of climate*.14(22): 4319-29.
- Henderson-Sellers B. 1986. Calculating the surface energy balance for lake and reservoir modeling: A review. *Reviews of Geophysics* 24(3): 625-649.
- Howell JR, Menguc MP, Siegel R. 2010. *Thermal radiation heat transfer*. CRC Press. USA.
- Huntington JL, McEvoy D. 2011. Climatological estimates of open water evaporation from selected Truckee and Carson River basin water bodies, California and Nevada. Desert Research Institute. Available at: http://www.dri.edu/images/stories/divisions/dhs/dhsfaculty/JustinHuntington/Huntington_an_McEvoy_2011.pdf [Accessed 25 May 2015].
- IPCC. 2014: *Climate Change 2014: Synthesis Report*. Contribution of Working Groups I, II and III to the Fifth Assessment Report of the Intergovernmental Panel on Climate Change [Core Writing Team, R.K. Pachauri and L.A. Meyer (eds.)]. IPCC, Geneva,

- Switzerland, 151 pp. Available at: https://www.ipcc.ch/pdf/assessment-report/ar5/syr/SYR_AR5_FINAL_full.pdf [Accessed 28 April 2015].
- Iziomon MG, Mayer H, Matzarakis A. 2000. Empirical models for estimating net radiative flux: A case study for three mid-latitude sites with orographic variability. *Astrophysics and Space Science* 273(4): 313-330.
- Jacobs AF, Heusinkveld BG, Kraai A, Paaijmans KP. 2008. Diurnal temperature fluctuations in an artificial small shallow water body. *International Journal of Biometeorology* 52(4): 271-280.
- Jensen ME. 2010. Estimating evaporation from water surfaces. In: *Proceedings of the CSU/ARS Evapotranspiration Workshop (Vol. 15)*. Available at: http://ccc.atmos.colostate.edu/ET_Workshop/ET_Jensen/ET_water_surf.pdf [Accessed 2 March 2015].
- Keijman J, Koopmans R. 1973. A comparison of several methods of estimating the evaporation of Lake Flevo, Proc. IAHS (Helsinki) Symposium on Hydrology of Lakes pp. 225–232.
- Key JR, Silcox RA, Stone RS. 1996. Evaluation of surface radiative flux parameterizations for use in sea ice models. *Journal of Geophysical Research: Oceans* 101(2): 3839-3849.
- Kipp & Zonen, Delft, Netherlands, 2014. Instruction manual: CNR4 net radiometer. Kipp & Zonen, Delft, Netherlands.
- Koberg GE. 1964. Methods to compute long-wave radiation from the atmosphere and reflected solar radiation from a water surface. US Government Printing Office pp. 107-136. Available at: <http://pubs.usgs.gov/pp/0272f/report.pdf> [Accessed 12 March 2015].
- Kristovich DA, Laird NF. 1998. Observations of widespread lake-effect cloudiness: Influences of lake surface temperature and upwind conditions. *Weather and Forecasting* 13(3): 811-21.
- Lamaro AA, Mariñelarena A, Torrusio SE, Sala SE. 2013. Water surface temperature estimation from Landsat 7 ETM+ thermal infrared data using the generalized single-channel method: Case study of Embalse del Río Tercero (Córdoba, Argentina). *Advances in Space Research* 51(3): 492-500.
- Li ZL, Tang BH, Wu H, Ren H, Yan G, Wan Z, Sobrino JA. 2013. Satellite-derived land surface temperature: Current status and perspectives. *Remote Sensing of Environment* 131: 14-37.
- Liou KN. 2002. An introduction to atmospheric radiation (Vol. 84). Academic Press. Canada.

- Liu WT. 1993. *Evaporation from the ocean* (Vol. 265). Cambridge University Press. UK.
- Lorenzetti JA, Araújo CAS, Curtarelli MP. 2015. Mean diel variability of surface energy fluxes over Manso Reservoir. *Inland Waters* (2): 155-172.
- Mahmud AA, Baten MA, Khan MB, Miyata A. 2015. Diurnal pattern of energy fluxes over rice field. *Journal of Environmental Science and Natural Resources* 6(1): 1-6.
- McCuen RH, Asmussen LE. 1973. Estimating the effect of heat storage on evaporation rates. *Hydrological Sciences Journal* 18(2): 191-196.
- McJannet DL, Cook FJ, Burn S. 2013. Comparison of techniques for estimating evaporation from an irrigation water storage. *Water Resources Research* 49(3): 1415-1428.
- McJannet DL, Webster I, Stenson M, Sherman B. 2008. Estimating open water evaporation for the Murray-Darling Basin: A report to the Australian Government from the CSIRO Murray-Darling Basin Sustainable Yields Project. CSIRO, Australia. Available at: <https://publications.csiro.au/rpr/download?pid=procite:0921ff52-a841-4574-b599-5f28a8716783&dsid=DS1> [Accessed 13 February 2015].
- McKenzie RS, Craig AR. 2001. Evaluation of river losses from the Orange River using hydraulic modelling. *Journal of Hydrology* 241: 62-69.
- McMahon TA, Peel MC, Lowe L, Srikanthan R, McVicar TR. 2013. Estimating actual, potential, reference crop and pan evaporation using standard meteorological data: a pragmatic synthesis. *Hydrology and Earth System Sciences* 17(4): 1331-1363.
- Mengistu MG, Savage MJ. 2010. Open water evaporation estimation for a small shallow reservoir in winter using surface renewal. *Journal of Hydrology* 380(1): 27-35.
- Monteith JL. 1965. Evaporation and the environment. In *Symposia of the society for experimental biology* 19: 205-234.
- Mukheibir P, Sparks D. 2003. Water resource management and climate change in South Africa: visions, driving factors and sustainable development indicators. Report for Phase I of the Sustainable Development and Climate Change project. Energy and Development Research Centre (EDRC), University of Cape Town. Available at: http://idprc.org/wp-content/uploads/2015/08/Water_resource_management-in-Southern-Africa.pdf [Accessed 23 February 2015].
- Mukheibir P. 2007. The impact of climate change on small municipal water resource management: The case of Bredasdorp, South Africa. Available at: <https://open.uct.ac.za/handle/11427/17197> [Accessed 20 February 2015].

- Nowak D, Vuilleumier L, Ohmura A. 2008. Radiation transfer in stratus clouds at the BSRN Payerne site. *Atmospheric Chemistry and Physics Discussions* 8(3): 11453-11485.
- Ohring G, Clapp P. 1980. The effect of changes in cloud amount on the net radiation at the top of the atmosphere. *Journal of the Atmospheric Sciences* 37(2): 447-454.
- Page JK, Rodgers GG, Souster CG, Le Sage SA. 1979. Predetermination of irradiation on inclined surfaces for different European centres. Final Report, Vol. 2, EEC Solar Energy Programme, Project F, Sheffield. Sheffield. Available at: <http://www.osti.gov/scitech/biblio/7035353> [Accessed 17 March 2015].
- Ramanathan V, Barkstrom BR, Harrison EF. 1989. Climate and the Earth's radiation budget. *International Agrophysics* 5(3-4): 171-181.
- Ramanathan V, Feng Y. 2009. Air pollution, greenhouse gases and climate change: Global and regional perspectives. *Atmospheric Environment* 43:37-50.
- Rozenstein O, Qin Z, Derimian Y, Karnieli A. 2014. Derivation of land surface temperature for Landsat-8 TIRS using a split window algorithm. *Sensors* 14(4): 5768-5780.
- Santos CACD, Silva BBD, Rao TVR, Satyamurty P, Manzi AO. 2011. Downward longwave radiation estimates for clear-sky conditions over northeast Brazil. *Revista Brasileira de Meteorologia* 26(3): 443-450.
- Savage MJ, Abraha MG, Moyo NC, Babikir ESN. 2014. Web-based teaching, learning and research using accessible real-time data obtained from field-based agrometeorological measurement systems. *South African Journal of Plant and Soil* 33(1): 13-23.
- Savage MJ, Everson CS, Odhiambo GO, Mengistu MG, Jarman C. 2004. Theory and practice of evaporation measurement, with special focus on surface layer scintillometry as an operational tool for the estimation of spatially averaged evaporation. Water Research Commission Report No. 1335/1/04, p204, ISBN 1-77005-247-X. Available at: <http://www.wrc.org.za/Knowledge%20Hub%20Documents/Research%20Reports/1335-1-04.pdf> [Accessed 23 March 2015].
- Savage MJ, Heilman JL. 2009. Infrared calibration of net radiometers and infrared thermometers. *Agricultural and Forest Meteorology* 149: 1279-1293.
- Savage MJ, Pasi JM, Myeni L, Clulow AD. 2016. Open water evaporation measurement using micrometeorological methods. Unpublished Water Research Commission Report No. K5/2335.

- Savage MJ. 2010. Sensible heat flux for estimating evaporation. D.Sc.Agric. thesis, University of KwaZulu Natal, Pietermaritzburg, South Africa.
- Savage MJ. 2012. Agrometeorology and environmental biophysics. Unpublished lecture notes, AMET210P1, University of KwaZulu-Natal, Pietermaritzburg, South Africa.
- Schott JR., Barsi JA, Nordgren BL, Raqueno NG, de Alwis D. 2001. Calibration of Landsat thermal data and application to water resource studies. *Remote Sensing of Environment* 78(1): 108-117.
- Schulze RE. 2011. Approaches towards practical adaptive management options for selected water-related sectors in South Africa in a context of climate change. *Water SA* 37(5): 621-646.
- Sima S, Ahmadalipour A, Tajrishy M. 2013. Mapping surface temperature in a hyper-saline lake and investigating the effect of temperature distribution on the lake evaporation. *Remote Sensing of Environment* 136: 374-385.
- Simpson D, Dickens C. 2006. Potential water quality impacts on Midmar Dam from the proposed Khayelisha social housing project. Institute of Natural Resources, Gauteng, South Africa. Available at: http://rava.qsens.net/themes/water_template/mgeni-catchment/Proposed%20Khayelisha%20housing%20project.pdf/at_download/file [Accessed 16 March 2015].
- Sinclair TR, Shiraiwa T, Hammer GL. 1992. Variation in crop radiation-use efficiency with increased diffuse radiation. *Crop Science* 32(5): 1281-1284.
- Steissberg TE, Hook SJ, Schladow SG. 2005. Characterizing partial upwellings and surface circulation at Lake Tahoe, California–Nevada, USA with thermal infrared images. *Remote Sensing of Environment* 99(1): 2-15.
- Swancar A. 2015. Comparison of evaporation at two central Florida lakes, April 2005–November 2007 (No. 2015-1075). US Geological Survey. Available at: <https://pubs.usgs.gov/of/2015/1075/ofr20151075.pdf> [Accessed 8 June 2016].
- Tanny J, Cohen S, Assouline S, Lange F, Grava A, Berger D, Teltch B, and Parlange MB. 2008. Evaporation from a small water reservoir: Direct measurements and estimates. *Journal of Hydrology* 351(1-2): 218-229.
- Timofeyev YM, Vasil'ev AV. 2008. *Theoretical Fundamentals of Atmospheric Optics*. Cambridge Int Science Publishing. UK.

- United States Geological Survey. 2013. Using the USGS Landsat 8 Product. Available at: http://landsat.usgs.gov/Landsat8_Using_Product.php [Accessed 3 May 2016].
- Valiantzas JD. 2006. Simplified versions for the Penman evaporation equation using routine weather data. *Journal of Hydrology* 331(3): 690-702.
- van Dijk M, van Vuuren SJ. 2009. Destratification induced by bubble plumes as a means to reduce evaporation from open impoundments. *Water SA* 35:158–167.
- Walpole RE, Myers RH. 1989. *Probability and Statistics for Engineers and Scientists*. 4th Edn., Macmillan. UK.
- Wang K, Liang S. 2009. Estimation of daytime net radiation from shortwave radiation measurements and meteorological observations. *Journal of Applied Meteorology and Climatology* 48(3): 634-643.
- Wang W, Xiao W, Cao C, Gao Z, Hu Z, Liu S, Shen S, Wang L, Xiao Q, Xu J, Yang D, Lee X. 2014. Temporal and spatial variations in radiation and energy balance across a large freshwater lake in China. *Journal of Hydrology* 511: 811-824.
- Winter TC, Buso DC, Rosenberry DO, Likens GE, Sturrock JrA, Mau DP. 2003. Evaporation determined by the energy-budget method for Mirror Lake, New Hampshire. *Limnology and Oceanography* 48(3): 995-1009.